On the structure of the internal wave field: the impact of the distribution of shear and strain variance in wavenumber-frequency space on mixing estimates

Brian Chinn

A dissertation submitted in partial fulfillment of the
requirements for the degree of

Doctor of Philosophy

University of Washington

2015

Reading Committee:

James B. Girton, Chair

Matthew H. Alford

Ren-Chieh Lien

Program Authorized to Offer Degree:
UW Oceanography

University of Washington

Abstract

On the structure of the internal wave field: the impact of the distribution of shear and strain variance in wavenumber-frequency space on mixing estimates

Brian Chinn

Chair of the Supervisory Committee:
Dr. James B. Girton
UW Oceanography

Data from an archive of McLane Moored Profiler (MP) deployments are used to investigate the role of internal waves, and in general physical processes occupying this frequency range, on the dissipation of kinetic energy and to study how these processes work to shape the spectral characteristics of the wavefield. The data used come from 5 separate field programs, and by analyzing them as a set, provides the opportunity to not only compare and contrast an unprecedented range of different forcing regimes, but also supports the discovery of unique observations of physical processes at individual sites. This dissertation is composed of four separate chapters that address different aspects of this idea.

First, two records, one to the North (MP1) and one to the South (MP2), of Mindoro strait, which lies between the South China Sea and the Sulu Sea, were used to study the processes driving mixing in the Strait. The records are dominated by near inertial variability and internal tides at both the diurnal and semidiurnal frequencies. Analysis of the velocity records from MP1 reveals suggestive evidence for the presence of parametric subharmonic instability of the diurnal tide as well as curious rectilinear bottom trapped near inertial waves. Diffusivities estimated via Thorpe scale analysis at MP1 reveal weak mixing over much of the water column that increases nearly an order of magnitude near the bottom and is strongly tied to the tides. Average mixing rates are found to be insufficient to produce

observed changes in water mass properties suggesting additional processes are at play.

Second, variability in the shear to strain ratio (R_ω) is investigated with the goal of understanding the factors that influence R_ω variability, quantifying its time and space scales, and determining how variability impacts estimates of parameterized diffusivity. Time mean R_ω from each of the sites spans a range from 1 to 10 and within each record, temporal variability around the mean is sufficient to produce a factor of 2-3 change in parameterized diffusivity. Vertical structure of R_ω appears strongly tied to topographic properties and wind forcing. In general, sites can be categorized as having R_ω controlled by shear or by strain. Finally, we find that with sufficient characterization of a site, a predictive model of R_ω can be made that reduces error in R_ω values relative to assuming $R_\omega = 3$ by over 30%.

Third, aspects of the the wavenumber frequency spectrum are explored. We find that while a separable representation of the spectrum can be made that has the same level of variance, the observed structure cannot be modeled with a single form in vertical wavenumber. Narrow band peaks attenuate to match the background continuum by wavenumbers of approximately $k = 10^{-2}$ cpm. At frequencies $\omega < 5$ cpd and wavenumbers $k > 10^{-2}$ cpm, we find that the spectrum is nearly white in frequency and that nearly all frequency bands have collapsed to this same structure. Background continuum spectral levels of velocity vary as a linear function of N. The background continuum spectrum, with peaks removed, displays significant deviations from GM at low wavenumbers. Addition of the narrow band peaks improves the consistency of the total spectrum with GM at low wavenumbers implying that the often observed GM spectral shape is dependent on the presence of internal tides.

Fourth, the impact of the inherent sawtooth sampling pattern in time and depth space of profiling instruments on resolved variance is examined through the use of virtual instruments profiling through an idealized wavefield. By creating a wavefield that has an exactly GM velocity spectrum, the variance resolved by various profiling schemes can be determined. We find that variance resolved, as computed from a spectrum from gridded profile data, can be

represented as a linear function of mean time between profile and latitude. A functional dependence is defined such that one can estimate a priori the impact of their sampling patterns. Additionally, the spectral response and bandwidth of the half inertial differencing operation is examined. It is found that the while half inertial differencing does eliminate even multiples of the inertial frequency and alias in odd multiples, the pass band of the filter is quite broad meaning there is potential for significant aliasing of non inertial signals into the inertial band estimates from the half inertial difference filter.

TABLE OF CONTENTS

LIST OF FIGURES

LIST OF TABLES

ACKNOWLEDGMENTS

I would like to thank my advisors James Girton and Matthew Alford as well as my committee members Steve Riser, Mark Warner, Ren-Chieh Lien, and Nathan Kutz. Their advice and guidance has been pivotal in making it through this process. I would also like to acknowledge my cohort of peers and fellow graduate students who provided valuable feedback, comments, and support.

Finally, I want to thank my wife Jennie for all of her support and encouragement.

DEDICATION

To Jennie, Tali, and Milo

Chapter 1
INTRODUCTION

1.1 Motivation

The thermohaline circulation of the ocean is controlled by processes that bring deep, cold, dense water formed at high latitudes back to the surface [Ganachaud and Wunsch, 2000, Lumpkin and Speer, 2007]. Repeat occupations of sites in the Pacific ocean 21 years apart revealed that ventilation rates of deep ocean tracers (temperature, salinity, ^{14}C, ^{226}Ra) had not changed [Munk, 1966]. Using a simple advection diffusion model with a vertical velocity estimated via mass flux arguments based on ocean basin size and production rates of deep water, Munk [1966] estimated that in order to maintain the observed tracer profiles an average or basin wide diffusivity of $\kappa = 10^{-4}\mathrm{m}^2\mathrm{s}^{-1}$ was required.

Recent studies, however, have highlighted that vertical diffusivity is not a spatially or temporally uniform process [Polzin et al., 1997, Levine et al., 1985, Ferron et al., 1998, Kunze and Sanford, 1996] and that the distribution of diffusivity is an important influence on numerical climate models [Melet et al., 2013, Jayne, 2009]. In actuality the ocean contains large swaths of area with low diffusivities [Kunze et al., 2006] and small regional hotspots with highly elevated diffusivity. The resultant local water mass changes at these hot spots are then carried along isopycnals into the oceanic interior or distributed locally. It is only on average that these different regimes provide sufficient mixing to maintain the abyssal stratification.

Numerous possible sources of this vertical mixing have been considered and it has been concluded that internal waves are likely the most significant contributor [Munk and Wunsch, 1998]. Internal waves are the continuously stratified analogue of surface gravity waves whose

motions are supported by the density stratification of the ocean. The band of frequencies (the internal wave band) within which internal waves can exist lies between the local inertial frequency (f) and the buoyancy frequency (N).

The dominant generation mechanisms of internal waves are atmospheric forcing, which drives inertial motions [Pollard and Millard, 1970, D'Asaro, 1985], and the interaction of the barotropic tide with topography [Baines, 1982, 1974, Garrett and Kunze, 2006] that produces internal tides (internal waves at tidal frequencies). Energy from these two sources is typically observed as spectral peaks that are narrow in frequency yet occupying a broad range in vertical wavenumber. Energy input via these mechanisms flows to smaller scales through nonlinear interactions and wave breaking until ultimately acted upon by molecular processes. Wave–wave non linear interactions allow energy to flow from its input at large scales to dissipation and influence the spectral shape of the internal wave band. Weakly resonant theory has found that these non linear interactions drive the shape of the internal wave spectral continuum by both moving energy between different scales and frequencies and tending to drive it toward a uniform structure in space and time [McComas, 1977, Müller et al., 1986].

An empirical model of the internal wave spectrum was developed by Garrett and Munk [1972] (GM72). This model was an effort to merge the typical observations of this era, that could only resolve in frequency or vertical wavenumber, into a single model that described variability in both of these dimensions. GM72 prescribes a functional form to the shape of the two dimensional spectrum that depends on local stratification and latitude and requires a separable form or that the wavenumber structure be independent of frequency. As understanding increased, incremental but significant improvements were made to this model. Here we consider the permutation of the GM model as modified by Cairns and Williams [1976] (GM76). Numerous observations have highlighted remarkable agreement with GM76 with the notable exception that GM76 does not include the commonly observed narrow band frequency peaks corresponding to the diurnal and semi diurnal internal tides. A thorough reanalysis of many previous studies by Polzin and Lvov [2011] highlights the agreement with,

and variations about, the spectral levels predicted by GM76.

The end product of this downscale transfer of energy from forcing through the continuum is to produce increased mixing. Because direct measurements of mixing via microstructure profilers are difficult to make and sparsely available, and because the dynamics of internal waves and their interactions with one another strongly influence the shape of the spectrum, parameterizations have been developed that use more easily observable internal wave properties, at more measurable scales, as proxies for turbulent dissipation of kinetic energy. These are known as finescale parameterizations [Gregg et al., 2003, Polzin et al., 1995]. Derivations of the fine scale parameterization use the idea that for a steady spectrum, the downscale rate of energy transfer due to non-linear interactions is proportional to the rate of turbulent dissipation. Finescale parameterizations are designed to capture the energy flux through the internal wave spectrum relative to GM76 and have several correction factors. This dissertation concerns itself most greatly with the correction that is made because of the typical lack of information about the frequency content of the measured wave field [Polzin et al., 2013].

Because records of oceanic properties are often simply vertical profiles, it is not possible to integrate over the internal wave band as is required to estimate dissipation. From vertical profiles of velocity and density, and leveraging what is known about the dynamics of single internal waves, the only information that can be deduced about frequency content comes from the ratio of kinetic to potential energy or the shear to strain ratio (R_ω). In GM76 the shear to strain ratio is uniformly $R_\omega = 3$. Reports of measured values of R_ω are sparse but those that do exist report significant deviations from the GM76 value [MacKinnon et al., 2013]. Despite the dependence of the parameterizations on R_ω, recent studies have applied the finescale parameterization with only density information and assumed that the wavefield has a GM shear to strain ratio of $R_\omega = 3$ [Whalen et al., 2012]. While these studies report agreement with microstructure data to within a factor of 2-3 the impact of non GM shear to strain ratios is unquantified.

This dissertation attempts to address several of the issues that have been presented above. The results presented span a wide range of sites and a breadth of mechanisms. The

underlying theme concerns the way in which processes at small scales can influence large scale phenomenon or how processes can communicate down or upscale. This is approached from several angles ranging from site specific process studies to examinations of aggregations of data.

All of the data used in this analysis comes from McLane Moored Profilers (MP). The MP provides sufficient vertical and temporal resolution such that we can isolate the frequency content at a wavenumber k and, for example, focus on the wavenumber structure of the internal tides separately from the continuum. Pinkel [1984, 1985] has made repeat attempts at characterizing the 2 dimensional (vertical wavenumber and frequency) structure of the internal wave field based on Doppler acoustic measurements of velocity from the research platform R/V FLIP. Results from these experiments, however, were limited by instrument noise floors, platform motion, vertical resolution, length of record, and variety of domains sampled. The MMP, however, has its own set of limitations that differ from that of the acoustic measurements from FLIP. Notably, the temporal resolution of the MMP is much less. By looking at our new results in conjunction with those of Pinkel and additional recent acoustic measurements, we hope to improve the state of knowledge about the nature of the wavenumber frequency spectrum.

Chapter 2 explores the processes contributing to the overall mixing state on both sides of the Mindoro Strait. The Mindoro Strait is the deepest connection between the South China Sea and the Sulu sea and is potentially a large contributor to the Indonesian through flow. Previous studies have highlighted the importance of understanding the processes at work in this region by estimating that a 10 sv Indonesian through flow could export as much as 0.5 PW from the Pacific Ocean and that the through flow may have strong feedbacks to the global climate [Godfrey, 1996]. Our analysis focuses on two moorings, one to the north, MP1, and one to the south, MP2, of Mindoro Strait. We report on several mechanisms that are at play in the strait. Specifically, we highlight the suggestive evidence for PSI of the diurnal tide forcing near inertial motions at the northern most mooring. Additionally, we find a curious rectilinear canyon trapped bottom intensified near–inertial wave. Further

analysis reveals that breaking of the internal tide is responsible for a large portion of the deep mixing at the northward side of the sill, however, observed diffusivities are not sufficient to explain the changes in water mass properties between the Sulu sea and the South China Sea.

Chapter 3 focuses on the mechanisms that influence the shear to strain ratio (R_ω) and the impact of variability in R_ω on parameterized diffusivity. We find that time mean R_ω varies from 1–10 on daily, weekly, and monthly scales and that variations are generally tied to local topographic roughness or wind variability. Observed variations in R_ω are sufficient to produce errors of a factor of 2–3 in time averaged parameterized diffusivity. This means that variability in R_ω is more than sufficient to explain the scatter that exists in comparisons between parameterized diffusivity and microstructure in studies that compute parameterized diffusivity and assume R_ω is a constant. In general sites can be categorized as having R_ω controlled by shear or by strain. We also report that with sufficient data, a linear model can be made at each site such that R_ω can be estimated based on shear or strain alone that has on average 30% less error than assuming $R_\omega = 3$. Lastly, we report that at $E_{shear} > 5$, shear and strain vary at nearly the same rate while at $E_{shear} < 5$, strain variations are 3 times weaker than shear. The findings from this work are an important contribution to understanding the limitations of and sources of error in our parameterized estimates of diffusivity.

Chapter 4 examines the structure of the wavenumber and frequency spectrum of shear and strain. In particular addressing the separability of the spectrum and how different frequencies of the spectrum have distinctly different structures in wavenumber. We use the singular value decomposition to produce an optimal separable representation of the wavenumber frequency spectrum of the internal wave band. While separable spectral representations of the wavefield capture close to the same level of variance as the input field, the distribution of this variance differs from the observations. By requiring separability, the background frequencies, and the narrow band strongly forced frequencies (f,1,2 cpd) are forced to have the same decay rate in vertical wavenumber. Our observations agree with previous results which show that this is not the case. At wavenumbers less than $\approx 10^{-2}$ cpm, variance in the narrow band peaks

decays more rapidly than the background which we define as frequencies that are not within 0.2 cpd of f,1,2 cpd.

Background spectra of strain show a shape very similar to the GM76 model while background spectra of velocity differ from GM76 at low wavenumbers. Instead of having a uniform slope, at low wavenumbers the velocity spectrum of the background begins to whiten. This is in contrast to the total frequency spectrum from these sites which typically have a very GM shape. This implies that the GM shape is maintained by the combination of variance from the narrow band peaks and the background "continuum". We find that background spectral levels of velocity vary in concert with N as expected from the GM spectrum, using arguments from internal wave propagation through varying stratification. Strain peak levels, though not varying linearly with it, appear to have some functional constraint related to meters above bottom, or the deepest depth sampled relative to the overall water depth with high strain scale factors only being observed at sites where the profiler reaches within 500m of the sea floor.

Chapter 5 quantifies the the response of various processing operations used with profiling instruments. Specifically, we focus on profiles from McLane Moored Profilers and half inertial differences from EM–APEX floats and use a synthetic Garrett and Munk 1976 velocity field. We find that the speed of the profiler strongly influences resolved spectral variance and that there is a significant change in resolved variance produced by gridding the profiles back to a uniform time depth map. Spectra from the non gridded vertical profiles show minimal loss in variance captured irrespective of profiling speed. Spectra from gridded data, however, show a strong dependence on profiler speed. At profiling speeds less than 15 cm/s for a 1000 m vertical window , resolved variance decreases rapidly, while at speeds above 15 cm/s improvements to resolved variance increase slowly. Gridded data appears to asymptote to a value of 95% of the input variance. The decrease in spectral levels from the gridding operation is uniform in wavenumber. This does not, however, agree with observations which show larger attenuation in spectral level at high wavenumber than at low wavenumber. The loss of variance from gridding is similar when computing variance from a frequency spectrum.

Over the range of profiling speeds tested, frequency spectra from the gridded data, capture up to 95% of the input variance with most of the loss of variance happening at high frequencies near the Nyquist. These results can in general be reduced to a single expression in terms of mean time between profiles which equates to the time between samples at the mid depth point of the sampling range. We find that half inertial differences effectively block out variance at all even multiples of the inertial frequency, but the filter has a large pass band over the odd multiples of the inertial frequency. This leads to potentially significant aliasing where variance at the tidal frequencies will be returned as near inertial variance.

1.2 Bibliography

P. G. Baines. On internal tide generation models. *Deep-Sea Res.*, 29(3a):307–338, 1982.

PG Baines. The generation of internal tides over steep continental slopes. *Philosophical Transactions of the Royal Society of London,Series A, Mathematical and Physical Sciences*, 277 (1263):27–58, July 1974.

J. L. Cairns and G. O. Williams. Internal wave observations from a midwater float, 2. *J. Geophys. Res.*, 81:1943–1950, 1976.

Eric A. D'Asaro. The energy flux from the wind to near-inertial motions in the surface mixed layer. *J. Phys. Oceanogr.*, 15(8), 1985.

Bruno Ferron, Herle Mercier, Kevin Speer, Ann Gargett, and Kurt Polzin. Mixing in the romanche fracture zone. *J. Phys. Oceanogr.*, 28:1929–1945, 1998.

A Ganachaud and C Wunsch. Improved estimates of global ocean circulation, heat transport and mixing from hydrographic data. *Nature*, 408:453–456, november 2000.

C. Garrett and Eric Kunze. Internal tide generation in the deep ocean. *Ann. Rev. Fluid Mech.*, 1:1056–8700/97/0610–00, 2006.

C. Garrett and W. Munk. Space-time scales of internal waves. *Geophys. Fluid Dyn.*, 3: 225–264, 1972.

J. S. Godfrey. The effect of the Indonesian throughflow on ocean circulation and heat exchange with the atmosphere: A review. *J. Geophys. Res.*, 101:12,217–12,238, 1996.

Michael C. Gregg, Thomas B. Sanford, and David P. Winkel. Reduced mixing from the breaking of internal waves in equatorial waters. *Nature*, 422:513–515, April 2003.

S R Jayne. The impact of abyssal mixing parameterizations in an ocean general circulation model. *J. Phys. Oceanogr.*, 39:1756—1775, 2009.

E Kunze and T B Sanford. Abyssal Mixing: Where It Is Not. *J. Phys. Oceanogr.*, 26(10): 2286–2287, October 1996.

Eric Kunze, Eric Firing, Jules Hummon, Teresa K Chereskin, and Andreas Thurnherr. Global abyssal mixing inferred from lowered ADCP shear and CTD strain profiles. *Journal of Physical Oceanography*, 36(8):1553–1576, 2006.

Murray D. Levine, Clayton A. Paulson, and James H. Morrison. Internal waves in the arctic ocean: Comparison with lower-latitude observations. *J. Phys. Oceanogr.*, 15(6):800–809, 1985.

Rick Lumpkin and Kevin Speer. Global ocean meridional overturning. *J. Phys. Oceanogr.*, 37:2550–2562, 2007.

Jennifer A. MacKinnon, Matthew H. Alford, Rob Pinkel, Jody Klymak, and Zhongxiang Zhao. The latitudinal dependence of shear and mixing in the Pacific transiting the critical latitude for PSI. *J. Phys. Oceanogr.*, 43(1):3–16, 2013.

C. Henry McComas. Resonant interaction of oceanic internal waves. *J. Geophys. Res.*, 82 (9):1397–1412, 1977.

Angelique Melet, Robert Hallberg, Sonya Legg, and Kurt L Polzin. Sensitivity of the ocean state to the vertical distribution of internal-tide-driven mixing. *J. Phys. Oceanogr.*, 43(3): 602–615, 2013. doi: http://dx.doi.org/10.1175/JPO-D-12-055.1.

Peter Müller, Greg Holloway, Frank Henyey, and Neil Pomphrey. Nonlinear interactions among internal gravity waves. *Rev. Geophys*, 24(3):493–536, 1986.

W. Munk and C. Wunsch. Abyssal recipes II: energetics of tidal and wind mixing. *Deep-Sea Res. Part I*, 45:1977–2010, 1998.

Walter H. Munk. Abyssal recipes. *Deep-Sea Res.*, 13:707–730, 1966.

Robert Pinkel. Doppler sonar observations of internal waves: The wavenumber-frequency spectrum. *J. Phys. Oceanogr.*, 14:1249–1270, 1984.

Robert Pinkel. A wavenumber-frequency spectrum of upper ocean shear. *Journal of Physical Oceanography*, 15:1453–1469, 1985.

R T Pollard and R C Millard. Comparison between observed and simulated wind-generated inertial oscillations. *Deep-Sea Res.*, 17:153–175, 1970.

K. L. Polzin, J. M. Toole, J. R. Ledwell, and R. W. Schmitt. Spatial variability of turbulent mixing in the abyssal ocean. *Science*, 276:93–96, 1997.

Kurt L. Polzin and Yuri V Lvov. Toward regional characterizations of the oceanic internal wavefield. *Rev. Geophys.*, 49(RG4003):1–61, 2011.

Kurt L. Polzin, John M. Toole, and Raymond W. Schmitt. Finescale parameterizations of turbulent dissipation. *J. Phys. Oceanogr.*, 25:306–328, 1995.

Kurt L. Polzin, Alberto C. Naveira Garabato, Tycho N. Huussen, Bernadette M. Sloyan, and Stephanie N. Waterman. Finescale parameterizations of turbulent dissipation. *Rev. Geophys.*, submitted, 2013.

Caitlin B Whalen, Lynne D Talley, and Jennifer A MacKinnon. Spatial and temporal variability of global ocean mixing inferred from argo profiles. *Geophys. Res. Lett.*, 39(L18612): doi:10.1029/2012GL053196, 2012.

Chapter 2

OBSERVATIONS OF INTERNAL WAVES AND PARAMETRIC SUBHARMONIC INSTABILITY IN THE PHILIPPINES ARCHIPELAGO

2.1 Abstract

Internal waves contain a significant fraction of the kinetic energy in the ocean and are important intermediaries between the forcing (by wind and tide) and interior diapycnal mixing. We report here on measurements from Mindoro Strait in the Philippines (connecting the South China Sea to the Sulu Sea) of an internal wave field with a number of surprising properties that point to previously-unrecognized processes at work in the region. Continuum spectral levels are very close to typical "background" values found in the open ocean, but internal tide energy (in both the diurnal and semidiurnal frequency bands) is significantly elevated—and higher at the northern mooring (MP1) than the southern (MP2). Two particularly energetic depth ranges stand out at MP1: an upper layer centered near 300 m, and one at the bottom of the water column, near 1800 m. The upper layer contains both internal tides and a near-inertial band with upward and downward propagating waves and an apparent spring-neap cycle. The combination is suggestive of Parametric Subharmonic Instability as the forcing for the near-inertial band—a conclusion supported by bicoherence estimates. Mixing (estimated from density overturns) is weak over much of the water column but enhanced by about an order of magnitude in the deep layer and closely tied to the internal tide (both diurnal and semidiurnal). Near-inertial currents in this deep layer are dominantly rectilinear and not well-correlated with the mixing. Bulk mixing rates at the two sites are less than required to produce property changes seen in hydrography, suggesting additional enhancement elsewhere in the archipelago.

2.2 Introduction

The Philippines Archipelago borders on the Pacific Ocean, South China Sea (SCS), and Sulu Sea (SS) and contains a complex network of islands, straits, and interior seas. Within the Archipelago, the Mindoro Strait is the deepest connection between the SCS and SS and, hence, may have a significant impact on both the SCS circulation and the Pacific-to-Indian Ocean throughflow (via Luzon and Makassar Straits). Because of these connections and the relatively unquantified flow field, an intensive field and modeling study was conducted in Mindoro Strait as part of an Office of Naval Research Department Research Initiative (DRI) called the Philippines Experiment (PhilEx). We report here on two moorings making high-resolution measurements in both time and depth at either end of Mindoro Strait. The chosen site presents a unique opportunity to study the interaction of internal waves in a large scale throughflow with narrow topography, very low latitude, and a highly energetic internal tide.

Internal waves are ubiquitous phenomena in the ocean, with frequencies, ω, lying between the Coriolis (or inertial) frequency f and the buoyancy frequency N. The internal wave field around complex archipelago topography is not as simple as the open ocean but many similarities exist between the two. Generally, the dominant forcing mechanisms for internal waves are thought to be wind forcing and interactions between topography and the barotropic tide. However, many of our ideas about the behaviour of internal waves in the ocean assume a minimal contribution from the bottom (other than during generation) and lateral boundaries. As we venture into shallow water or constraining bathymetry, the shape of the topography can play a major role in setting the amplitude and structure of the wavefield through reflection, focusing, or steering [*Hotchkiss and Wunsch*, 1982, *Eriksen*, 1982, *Kunze et al.*, 2002].

In addition to wind and topography, internal waves can be generated and modified through non-linear interactions within the wavefield itself. A particular interaction of interest is Parametric Subharmonic Instability (PSI), in which an initial internal wave of frequency ω breaks down into two daughter waves of frequency $\omega/2$. The intention of this paper is to

present a first look at the details of the internal wave field of two Philippine seas, including candidate generation mechanisms and implications for mixing of throughflow waters. Specifically, data from two moored profilers are used to establish a baseline picture of the internal wave climate in the Philippines and to highlight an observed relationship between localized energetic near-inertial waves and the internal tide. We also present preliminary observations showing a curious form of near-inertial wave that appears trapped at depth and has a very rectilinear current ellipse. Additionally, the locations of the moorings, one in the SCS and one in the SS, allow us to compare and contrast two regions with different magnitudes of internal tides (*i.e.*, significantly larger in the SCS).

2.3 Measurements

PhilEx was designed not only to provide exploratory measurements of the Philippines circulation, but also to test the ability of regional numerical models to simulate small-scale processes and their impact on mixing and biological productivity. In order to characterize the candidate processes, two profiling moorings (MP1 and MP2) were deployed from late December 2007 through early March 2008 [*Girton et al.*, 2011] at the Northern (MP1: 12°50.260′ N, 120°36.404′ E) and Southern (MP2: 10°21.318′ N, 121°44.094′ E) ends of Mindoro Strait (Fig. 3.1a). The combination of long duration and high resolution in depth and time from multiple instruments was chosen to give maximum flexibility in the analysis of an unknown set of intermittent processes including mesoscale flow variations, tides and internal waves, and turbulence.

2.3.1 Instrumentation

MP1 was configured with two Mclane Moored Profilers (MMP) stacked on a single wire with each sampling about 900 m of the water column while MP2 employed a single MMP over the entire 1500 m deep water column. Each of the three MMPs was equipped with an acoustic velocimeter and a CTD, providing full depth records of u and v velocity, salinity, temperature, and depth for the entire 3 months of the deployment at intervals of approximately 1.5 hours

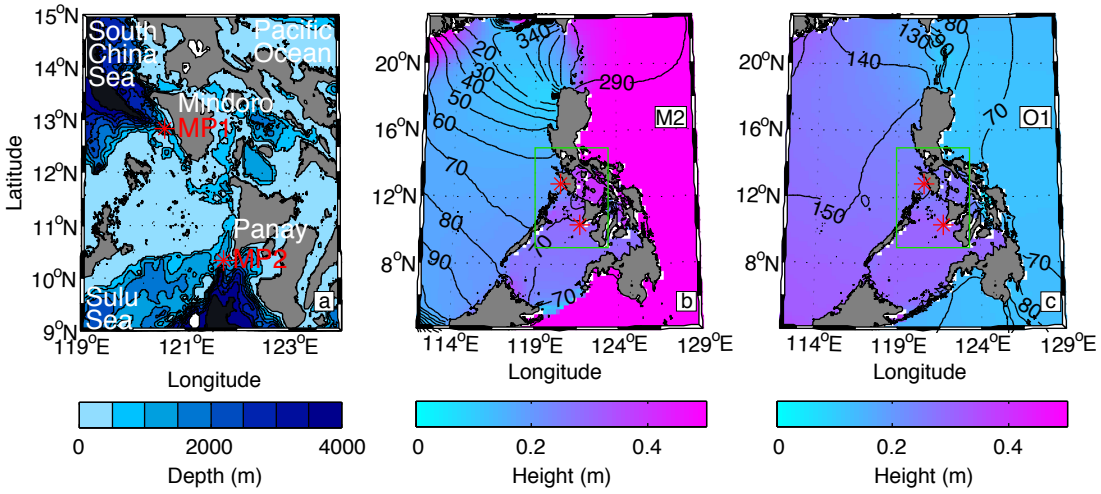

Figure 2.1: Overview maps showing (a) the bathymetry of the Mindoro Strait, including the mooring sites MP1 and MP2 and the narrow channel connecting the two, and the regional surface height amplitude and phase distribution of the (b) M2 semidiurnal tide and (c) O1 diurnal tide from TPXO. The smaller region shown in (a) is indicated in (b,c). Although the tidal maps are for specific constituents, they are nearly indistinguishable from those for the other constituents in the diurnal and semidiurnal bands (*e. g.*, S2 and K1).

and a vertical resolution of 2 m. Both moorings were equipped with a downward-looking 75 kHz ADCP and an upward-looking 300 kHz ADCP in the near-surface buoy (30m at MP1 and 50m at MP2). MP1 had an additional 300 kHz ADCP at the bottom, however it only survived for the first ten days of the deployment. All instruments used 8 m bin sizes, made pings every minute, and saved 10 minute ensembles.

2.3.2 Time and Depth Structure

Figure 2.2 presents unfiltered time–depth maps of eastward (u) velocity from MP1 and MP2 along with a subset of isopycnals. Despite lying in similar environments ($\sim$50 km wide, $<$2000 m deep channels adjoining deep basins) and being separated by only 300 km, the two records are strikingly different in both their temporal and vertical structure. Both records have an energetic water column (especially above 500 m; Fig. 2.3b) with clearly identifiable

high-frequency fluctuations, including periodic motions near 0.5, 1, and 2 cycles per day (cpd), as well as a low-frequency modulation, evident even in the raw velocity record.

Time mean profiles of both buoyancy frequency squared (N^2) and shear squared, ($S^2 = u_z^2 + v_z^2$), are larger at MP1 than at MP2 for nearly the entire depth range as seen in Figure 2.3a. Similarly, total horizontal kinetic energy (HKE= $\frac{1}{2}\rho(u^2 + v^2)$), is greater at MP1 than at MP2 over the entire depth range (see Fig. 2.3b). Note that at MP1 we see a signal of elevated energy at depth whereas energy generally decreases with depth at MP2.

Tidal (1 and 2 cpd) variability is stronger at MP1 at all depths, with both barotropic and low-mode baroclinic components. In order to separate barotropic and baroclinic signals, we define barotropic quantities as depth-averages ($\overline{X} = \frac{1}{H}\int_{-H}^{0} X\ dz$) and baroclinic as the remainder ($X' = X - \overline{X}$). The near complete water depth coverage, H = water depth, makes it possible for us to do this separation unambiguously.

The upper energetic region at MP1, located between 300 and 500 m depth, also contains significant near-inertial motions (Fig. 2.2a). MP2 contains more energy at lower (sub-inertial) frequencies, as well as larger isopycnal displacements at depth (Fig. 2.2d), including high-frequency intermittent events and low-frequency excursions.

2.3.3 Frequency Spectra

To look at energy content as a function of frequency, rotary spectral estimation is done such that a complex velocity, $u + iv$, is decomposed into clockwise (CW) and counterclockwise (CCW) rotating components as described by Gonella [1972]. Spectral estimates at each depth are averaged and logarithmically smoothed in frequency. Confidence intervals are derived using the number of degrees of freedom in the frequency smoothing (equal width in log space) and a vertical decorrelation scale of 30 m, as calculated from our inertial band-passed velocity records. The choice of decorrelation scale was driven by our focus on the inertial motions in the record. However, we recognize that there is indeed a frequency dependence in vertical decorrelation scale that we have chosen to omit here.

The resulting mid-depth frequency spectra averaged over 250–500 m (Fig. 2.4a and b)

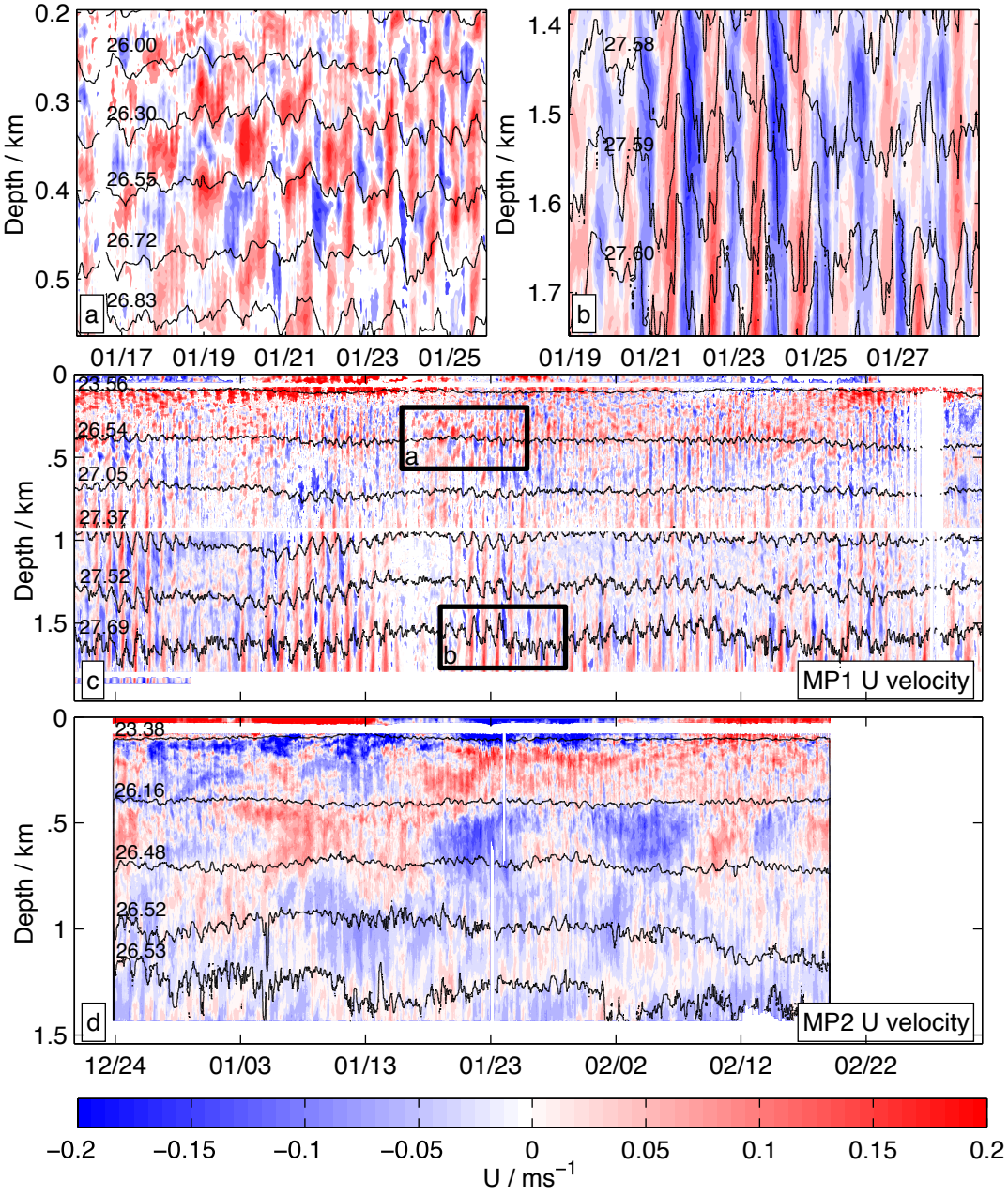

Figure 2.2: Unfiltered eastward (u) velocity component from MP1 (panel c) and MP2 (panel d), with depths of isopycnal surfaces shown in black. Panels a and b show expanded versions of two periods in the MP1 record (black boxes in panel c) illustrating the signature of the near-inertial mid-depth motions and the relationship between isopycnal heaving and velocity at depth.

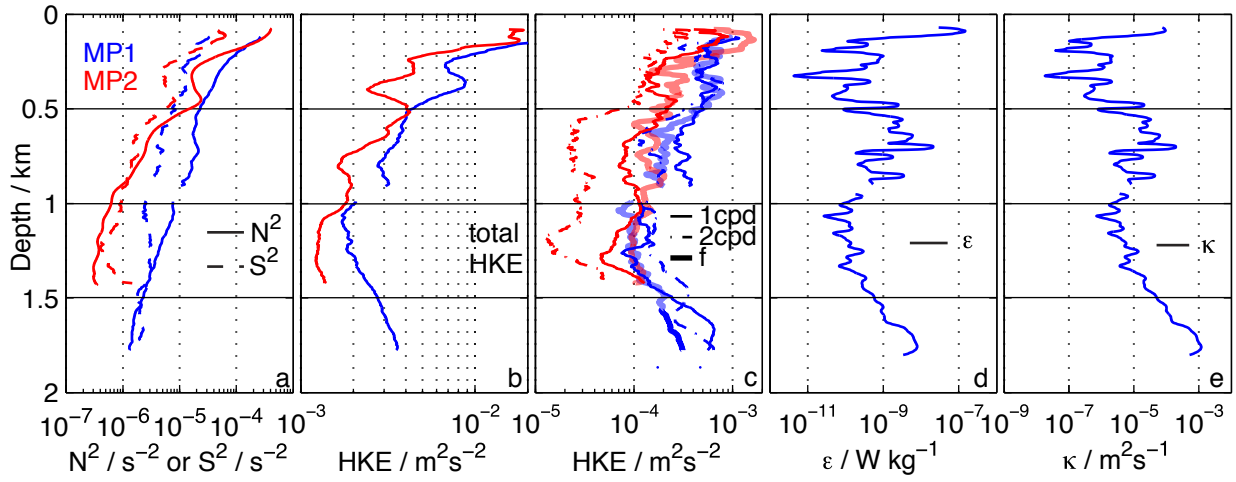

Figure 2.3: Time-mean vertical profiles at MP1 and MP2. In all panels blue corresponds to MP1 and red corresponds to MP2. Panels a-d show: (a) squared buoyancy frequency ($N^2 = -\frac{g}{\rho}\frac{\partial \rho}{\partial z}$) and shear ($S^2 = u_z^2 + v_z^2$), (b) unfiltered total horizontal kinetic energy (HKE), (c) local near-inertial, diurnal, and semi-diurnal baroclinic HKE (BHKE), (d) dissipation of turbulent kinetic energy (ϵ), and (e) diffusivity (κ) at MP1 determined from density overturns (ϵ and κ from MP2 not shown).

show significant peaks in variance density in the inertial (2.8 day period at MP2 and 2.2 days at MP1), diurnal (1 cpd), and semi-diurnal (2 cpd) frequency bands, with an equipartition of energy between the CW and CCW rotating tidal components. Inertial peaks at both sites are broad and have more energy in the CW rotating band as we would expect of inertial oscillations in the northern hemisphere.

Continuum levels at both sites agree very well with the Garrett and Munk (GM76) spectrum [*Garrett and Munk*, 1975, *Cairns and Williams*, 1976]. Due to noise floor saturation caused by the FlowQuest instrument at MP2, a constant noise level of $1.5 \times 10^{-5}\mathrm{m^2 s^{-2} cpd^{-1}}$ corresponding to a 1.2 cm $\mathrm{s^{-1}}$ rms, has been removed from that spectrum (uncorrected spectra are shown in dotted lines).

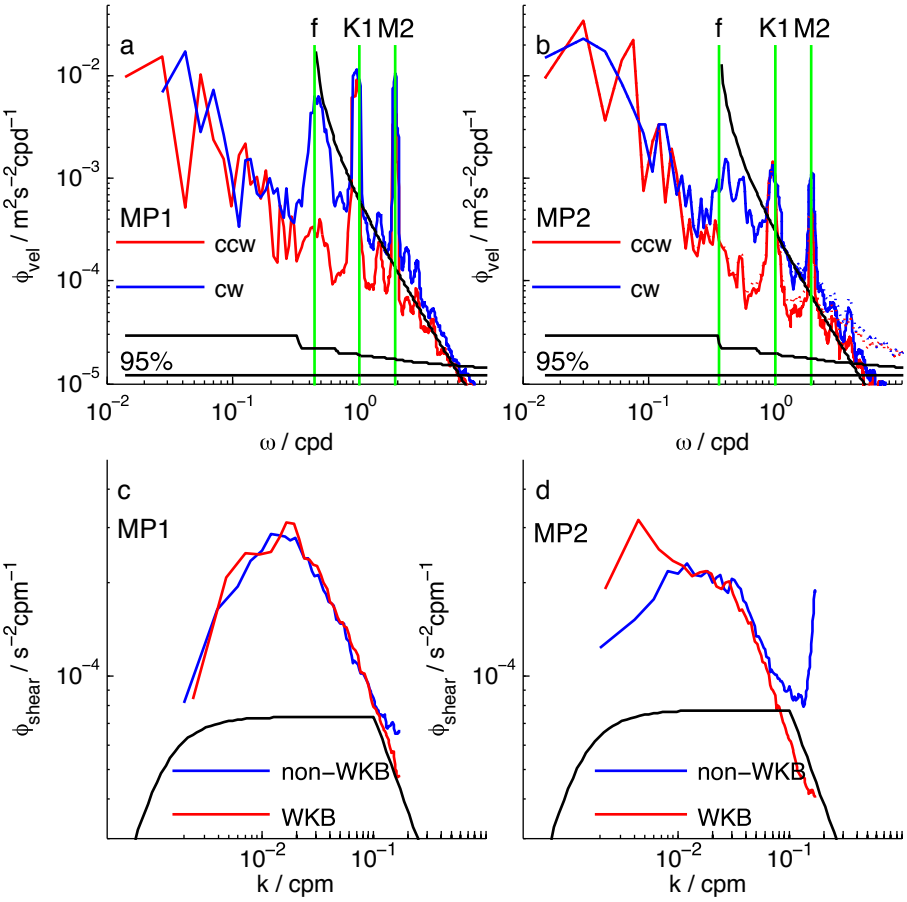

Figure 2.4: Frequency rotary velocity spectra for MP1 (a) and MP2 (b). Velocity spectra are averaged over $z \in [250 : 500]$m and are shown with green lines indicating the local inertial, M2, and K1 frequencies and black curves representing the spectral shape as predicted by the Garrett and Munk 1976 model [*Garrett and Munk,* 1975; *Cairns and Williams,* 1976]. The dotted lines in panel b show the spectrum before removal of the $1.5 \times 10^{-5}\,\mathrm{m^2\,s^{-2}\,cpd^{-1}}$ noise level of the FlowQuest ADCP (corresponding to a $1.2\,\mathrm{cm\,s^{-1}}$ single-ping RMS error). Black lines in the bottom of panels a and b indicate 95% confidence intervals. Vertical wavenumber spectra of shear for MP1 (c) and MP2 (d). Blue curves in panel c and d correspond to shear spectra calculated over the full depth range while red curves are the same spectra calculated on a WKB stretched and scaled velocity record. In both the unstretched and the WKB stretched record, shear spectra are calculate for each profile and the resulting spectra from the first 500 profiles (31 days) are averaged together and shown here.

2.3.4 Frequency Bands

The presence of narrow and well-separated peaks in frequency spectra suggests that bandpass filtering may be a useful way to describe the observed phenomena. In this way, the amplitude modulation of the bands can be described and compared without explicit separation of the tidal constituents within each band (*i. e.*, M2 and S2 in the 2 cpd band). We use fourth order Butterworth filters with a passband of ±20% for the diurnal and semi-diurnal frequencies, and a slightly wider ±22.5% for the inertial (to accommodate the broader inertial peak as seen in Fig. 2.4). The low latitude results in an inertial frequency that is clearly separated from the tidal frequencies, and thus minimal leakage between filtered frequency bands is expected.

The vertical structure of horizontal kinetic energy from the bandpassed baroclinic velocities is shown in Figure 2.3c. At MP1, BHKE (baroclinic HKE) in both the diurnal and semi-diurnal tidal bands are of comparable magnitude over the entire depth range and are greater than both tidal components of BHKE at MP2. BHKE in the 1 cpd band is much larger than the 2 cpd band at MP2 by roughly a factor of five.

Near-inertial BHKE indicates similar background levels at MP1 and MP2 however, there are large excursions from this background level at MP1 both at the bottom and at approximately 400 m depth. The band of increased amplitude in the upper water column corresponds with lines of coherent phase propagation visible in time depth maps of u velocity (Figs. 2.5b and d). Coherent propagating near-inertial waves are largely absent from MP2.

Further separating the inertial-bandpassed motions into clockwise and counterclockwise rotation with depth (together with the dominance of clockwise rotation in time) allows diagnosis of the vertical phase propagation. Due to the propagation characteristics of linear internal waves, upward phase propagation (phase velocity) implies downward energy propagation (group velocity). The upper energetic depth range includes both CCW and CW rotation with depth (upward and downward energy propagation, respectively).

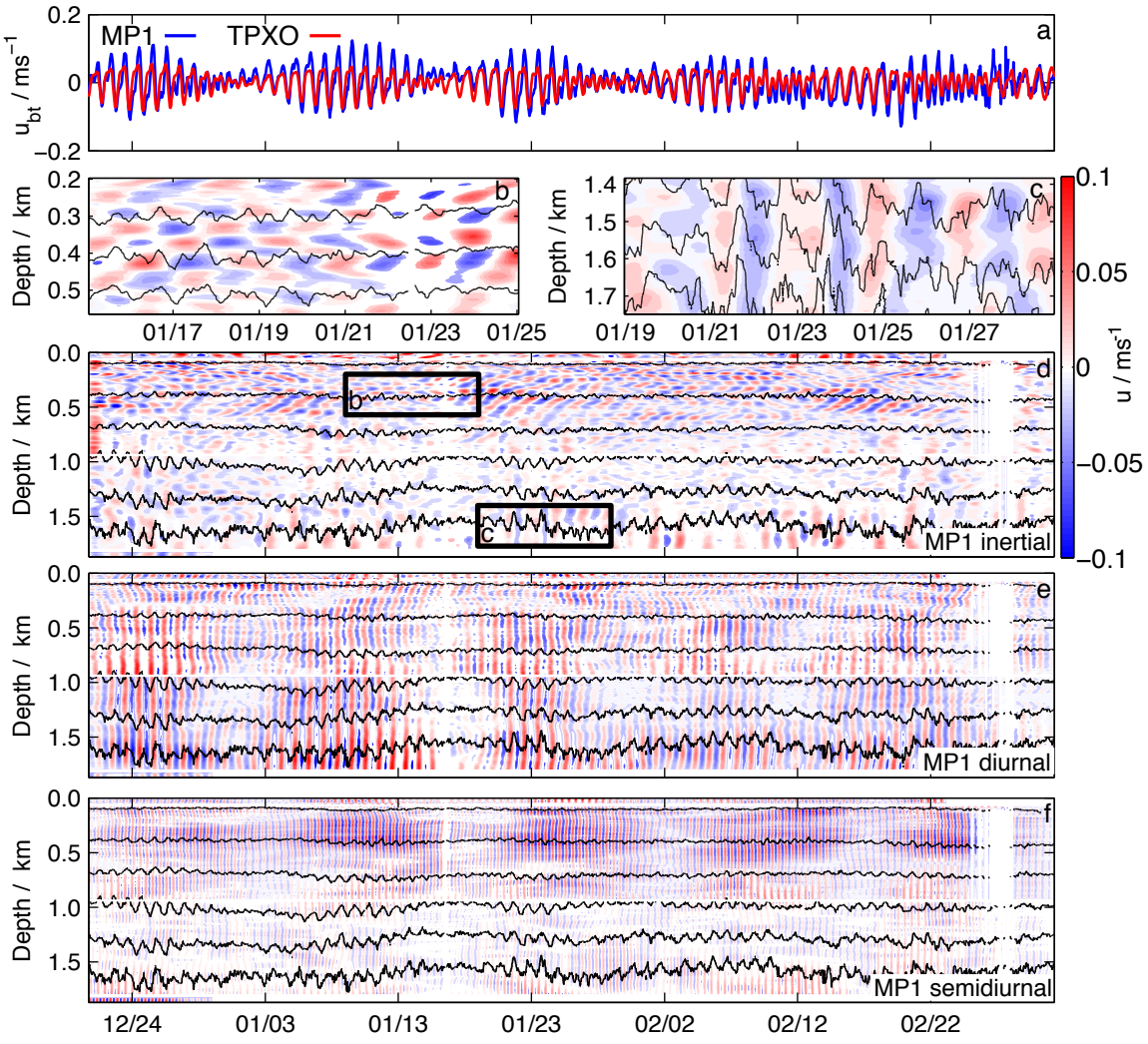

Figure 2.5: Time series plots from the mooring MP1 showing (a) u_{bt}, the barotropic along channel tidal velocity as determined from MP1 vs prediction from TPXO 7.1, (b), zoom in of u velocity at MP1 showing strong lines of phase propagation in the mid depth energetic layer, as well as "checkerboarding" indicating the presence of both upward and downward propagating waves, (c), zoom in of deep inertial motions at MP1, (d), full u velocity record from MP1 bandpass filtered around the local inertial frequency, (e) full u velocity record from MP1 bandpass filtered around 1 cycle per day, (f) full u velocity record from MP1 bandpass filtered around 2 cycles per day.

2.3.5 Wavenumber Spectra

Despite the observed differences between frequency spectra at MP1 and MP2, the two sites look far more similar when we look at mean vertical wavenumber spectra of shear. In order to facilitate the comparison of internal wave properties at different depths and locations we make use of the WKB transformation to account for the effects of vertical variations in stratification. Following *Leaman and Sanford* [1975] we scale the velocity record and vertical structure such that $u_{wkb}(z) = u'(z)/(N(z)/N_o)^{1/2}$ and $dz_{wkb} = [N(z)/N_o]dz$ and calculate the shear spectrum as the product of the wkb stretched velocity spectrum with the squared wavenumber.

Shear spectra averaged over the first 500 profiles (∼31 days) and across most of the water column (see figure 2.4 panels c and d) reveal similar peak energy levels and show that both sites have about 2 times the level of shear in the GM76 model spectrum. Despite the elevated peak levels, the high wave number roll-off in the "saturated" range of each spectrum matches that found by previous investigators [*Gargett et al.*, 1981].

2.4 Tides

Not surprisingly, given the mooring locations in relatively narrow straits, tidal variability makes up a large part of the velocity signal at both locations. The levels at the two sites are quite different, however, both in the depth-uniform (barotropic) and depth-varying (baroclinic) components. We interpret these differences in terms of the nearby structure of the open-ocean barotropic tides (Fig. 3.1b,c) and the generation of internal (baroclinic) tides by topography.

2.4.1 Barotropic Tides

The barotropic component makes up a significant portion of the tidal variability (both diurnal and semi-diurnal) at each mooring site, as evidenced by the vertical striations in the raw velocity records (Fig. 2.2) and the tidally bandpassed records (Fig. 2.5e,f). Because of

the large wave speeds and length scales of the barotropic mode, we expect the barotropic tide at each MP location to be closely connected to that in the adjacent open basins of the South China and Sulu Seas. As summarized by *Wyrtki* [1961] and confirmed in the latest version (7.1) of the 9-constituent TPXO global inverse solution [*Egbert and Erofeeva*, 2002], diurnal and semidiurnal tides in the region have strikingly different and geographical structures, with semi-diurnal tides strongest in the Pacific Ocean and diurnal tides dominating the SCS (Fig. 3.1b,c). Although the accuracy of the large-scale fields is partially dependent on the coarse-resolution barotropic model used in the TPXO inversion, these fields do contain clues about the smaller-scale response of barotropic and baroclinic tides to unresolved bathymetry. For example, large phase gradients across the various straits and island chains around the Philippines indicate strong reversing tidal pressure gradients and likely locations for accelerated currents and internal tide generation. Two of the most obvious of these are Luzon Strait at the north end of the SCS and Sibutu Passage and the Sulu Archipelago at the south end of the SS. Strong internal tides and tidally-generated non-linear internal waves have been observed in both locations. In contrast, the barotropic phase gradient across Mindoro Strait is relatively weak in both constituents and suggests a more limited role in internal tide generation.

We have extracted the TPXO velocity predictions at MP1 and MP2 for comparison with the measured depth-averaged velocity at each site. In addition, we have conducted a harmonic analysis of each mooring's timeseries using the T-Tide software package [*Pawlowicz et al.*, 2002]. In an attempt to correct for differences between the TPXO model bathymetry and the real water depth at our mooring locations, we have scaled the TPXO velocity amplitudes by the model-to-measured depth ratios 0.6 and 0.86 at MP1 and MP2, respectively. Results are shown in Table 2.1 and Figure 2.5a.

In the timeseries comparison, the observed spring and neap tides lag TPXO by about a day, while individual ebb and flood events are nearly in phase with each other. In general we find that, for all frequency constituents and both velocity components, the amplitudes are greater at MP1 than at MP2 in both our observations and TPXO. In fact, the time mean of

Vel	σ	MP1	TPXO@1	MP2	TPXO@2
u	m2	**.017 [339°]**	.0094 [10°]	.0003 [257°]	.0009 [144°]
	s2	**.0110 [37°]**	.0054 [46°]	.0002 [80°]	.0006 [210°]
	k1	**.0164 [161°]**	.0157 [120°]	**.0022 [309°]**	.0007 [215°]
	o1	**.0161 [100°]**	.0141 [90°]	**.0016 [158°]**	.001 [153°]
v	m2	**.0222 [170°]**	.0124 [188°]	**.0088 [348°]**	.0127 [22°]
	s2	**.0140 [232°]**	.0071 [226°]	**.0036 [66°]**	.0072 [103°]
	k1	**.0226 [343°]**	.0212 [299°]	**.0054 [21°]**	.0176 [253°]
	o1	**.0231 [281°]**	.0186 [269°]	**.0087 [293°]**	.0166 [233°]

Table 2.1: Amplitude (in meters) and [Greenwich phase] (in degrees) of barotropic tidal harmonics as observed at MP1 and MP2 and predicted by the TPXO 7.1 model at both locations. TPXO velocities at MP1 and MP2 have been scaled by 0.6 and 0.86 to account for the model's coarsely-resolved bathymetry. Statistically significant observed values are shown in **bold.**

barotropic kinetic energy at MP1 is nearly 3 times that of MP2 (roughly the same scaling as the squared ratio of the TPXO amplitude predictions at the two locations). In addition, we find better agreement between measured and predicted phase at MP1 than MP2—likely the result of the stronger signal at the former. This overall agreement suggests that the basic properties of the barotropic tides are relatively well characterized by the TPXO model.

2.4.2 Internal Tides

Much as was seen in the barotropic tide, the baroclinic internal tide is much stronger at MP1 than at MP2. We look in more detail at this difference in strength, by calculating the energy flux associated with the internal tide at both sites. We focus on the diurnal fluxes, since semidiurnal fluxes at both sites were much weaker.

Having both density and velocity information over the entire water column, we can estimate the energy flux in the internal tide as $F_u =< u'p' >$ where u' and p' are the baroclinic

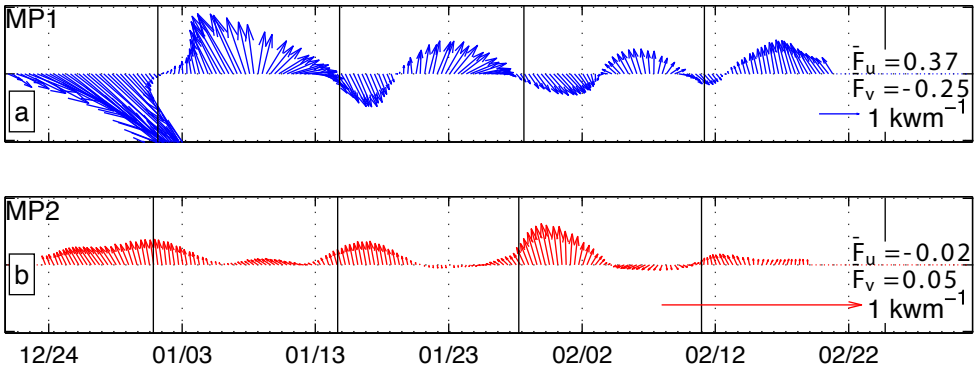

Figure 2.6: Timeseries of depth-integrated diurnal internal tide energy flux ($F_u =< u'p' >$ and $F_v =< v'p' >$) at MP1 (a) and MP2 (b) and time mean flux components. Vertical black bars indicate diurnal neap tides (k1+o1) as predicted by TPXO.

velocity and pressure respectively, and we define the $< X >$ operator as a time-average over a tidal cycle. We calculate $\overline{F}$ following the procedures outlined by *Nash et al.* [2005] with the diurnal internal tide energy fluxes from both moorings shown in Figure 2.6. At MP1, the flux is oriented along the axis of the canyon but the direction varies between NW and SE. The largest period of observed flux at MP1, near the end of December, has a magnitude of slightly greater than 2 kW m^{-1} while the other peaks are less than 1kW m^{-1}.

The flux is predominantly contained within the first two baroclinic modes, with the mode 1 energy flux always directed to the east, but pulsing in phase with the barotropic tide, and the mode 2 energy flux oscillating between NW and SE. The peaks of diurnal energy flux for both modes tend to coincide with diurnal spring tides to within 2–3 days. This observed phase correlation between baroclinic and barotropic tides implies a "relatively" local generation. Using the method described by *Rainville and Pinkel* [2006a], we can make estimates of the group velocities for the mode 1 internal tide of 200 km/day and for mode 2 of 100 km/day. The group speeds, and our estimates of phase offset, put potential generation sites for the observed internal tide within roughly 500 km.

Given the large amplitude of the energy fluxes, the observed internal tides must be coming from a site with intense barotropic to baroclinic conversion. *Alford et al.* [2011] have shown

that Luzon Strait ($\approx$ 300km to the north) is a site with extremely high levels of internal tide energy by both open ocean standards and when compared to other strong generation sites like the Hawaiian Ridge. Numerical modeling studies carried out by *Simmons et al.* [2011] agree that Luzon Strait is one of the strongest generators of the diurnal internal tide and reveal that there is a beam of K1 energy that leaves Luzon Strait and moves southward through the SCS towards MP1. Though not conclusive, this beam of diurnal energy from Luzon Strait is a potential source for the observed internal tide at MP1. The variability of the flux direction suggests that this distant source may interfere with waves from a local source to the southeast, likely Mindoro Strait itself.

Diurnal energy flux at the southern mooring, while still contained predominantly in the first two modes, is much weaker with the largest peaks up to .2kW m^{-1} with average peaks on the order of .1kW m^{-1}. Despite being weaker, the energy flux is significantly more consistent in terms of direction with energy predominantly moving into the channel from the South. There is much less of a clear relationship between the baroclinic internal energy flux and the barotropic tide at MP2 with little observed correlation between the observed peaks in energy flux, and the spring tides as predicted by TPXO.

2.5 Inertial-band Motions in Northern Mindoro Strait (MP1)

In addition to the overall differences in internal tide energy corresponding to the different tidal forcing environments of the two locations, two other internal wave phenomena stand out in the northern mooring record (MP1). The first is the low-frequency modulation of upward and downward propagating near-inertial motions in the lower thermocline (between 200 and 800 m depth), and the second is a similar modulation of rectilinear near-inertial motions near the bottom of the water column. Examples of these are highlighted in the raw velocity record in Figures 2.2a and b, in the inertial record in Figures 2.5b and c, and are discussed further below.

2.5.1 Thermocline Inertial Motions

The mid-depth peak in inertial BHKE at MP1 is marked by strongly-sloping phase lines (both upward and downward) and a pronounced low-frequency modulation. The bi-directionality of the waves suggests mid-depth generation, but nearby reflection of downward-propagating waves off subcritical topography is also a possibility. Although the ∼14-day period of the modulation is a likely indicator of tidal influence, we first consider the more typical source of near-inertial energy—the wind.

Wind Forcing

The mid-depth near-inertial signals are clearly visible in the time–depth plot of u velocity in Figure 2.5b. The characteristic upward sloping phase lines are indicative of an internal wave packet propagating with a downward group velocity [*Leaman and Sanford*, 1975]. The direction of propagation and water column location indicate that their generation may be related to surface forcing. Using wind data from the COAMPS model [*Pullen et al.*, 2007] we estimate the localized input of energy from the wind into the ocean with a slab model approach [*D'Asaro*, 1985, *Alford*, 2001]. Figure 2.7a shows the resultant integrated flux into the mixed layer and corresponding along-channel wind velocity. Flux estimates are based on a constant mixed layer depth of 50 m and are dominated by a large wind event near January 20, 2008. If the inertial current events we observe in our time–depth record are caused by local atmospheric forcing we would expect the BHKE of these inertial motions to be highly correlated with the wind input.

However, little correlation is seen between the slab model output and either the observed inertial currents in the upper 50 m of the water column or the deeper motions in the thermocline. In fact, there is little or no response in the mixed layer from the predicted large injection of energy near January 20th as a storm swept over the mooring moving from east to west. Clearly, the presence of nearby boundaries makes the slab model less useful than in the open ocean, but the lack of anything like a 14-day cycle in the wind forcing suggests a

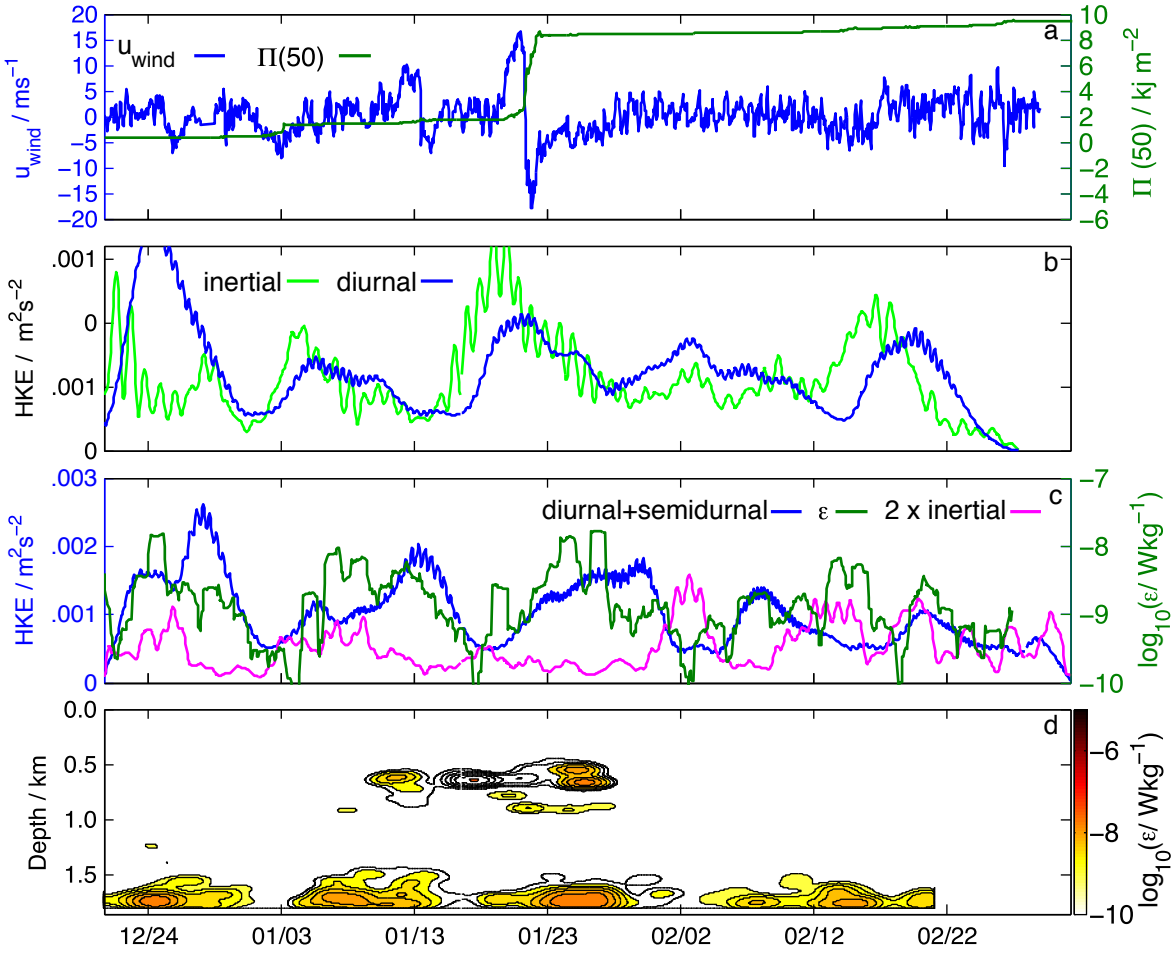

Figure 2.7: Time series plots from mooring MP1 showing (a) u_{wind} along channel wind velocity and $\mathrm{P}(50) = \int_0^t \Pi(50)\mathrm{dt}$, which is the integrated flux of energy into the mixed layer following *D'asaro* [1985], (b), Inertial HKE and 1 cpd BHKE from MP1 showing similar low frequency modulations, (c), total tidal baroclinic (1+2 cpd) HKE, two times the local inertial HKE, and turbulent dissipation of kinetic energy, $log_{10}(\epsilon)$ averaged over the bottom 200m of the water column, (d), $log_{10}(\epsilon)$ as calculated from a Thorpe scale analysis showing low frequency signal at depth.

different source for the near-inertial motions.

As internal waves have been shown to propagate great distances, it is worth considering that the motions we observe were perhaps not forced locally. However, most studies showing long range propagation were concerned with low-mode waves, not the relatively high-mode signals we observe. Via a simple ray tracing calculation following *Alford and Gregg* [2001] we can estimate when and where the internal waves we observe at 400 m might have been generated. Results of this calculation predict that the generation region would be about 100 km and nearly 80 days away. Given the high mode structure of these motions it is unlikely that such waves would survive their transit across a mesoscale field that would tend to shear the motions apart.

Tidal Modulation of the Inertial Band

Re-examining the timeseries of inertial BHKE over the 250–500 m range (Fig. 2.7b) reveals that not only does the inertial level not correlate well with the predicted wind energy input but that it has a low frequency modulation that resembles the local spring–neap cycle of the diurnal tide. The tidal and inertial signals have a statistically significant correlation of 0.56, with peak diurnal BHKE lagging by 34 hours. Varying the averaging depth range, bandpass filter width, and center frequency reveals that values of correlation coefficient and corresponding lag are robust to changes in these parameters. This correlation between the two timeseries is a characteristic we would expect from the breakdown of the diurnal internal tide via a wave-wave interaction process. However, the time lag, though small compared to the 14-day period of the modulation, is opposite what we might expect from such an interaction. This phasing is a puzzle to which we will return later.

Parametric Subharmonic Instability

With no evidence to support wind forcing of the upper water column near inertial motions and a strongly suggestive correlation with the internal tide, we look for a specific coupling mechanism. A particular form of wave–wave interaction that has recently been implicated

in open ocean situations [*Rainville and Pinkel*, 2006b, *Carter and Gregg*, 2006, *Alford*, 2008] is parametric subharmonic instability (PSI), which involves the non-linear breakdown of an internal wave into two waves with half the frequency of the original [*Muller et al.*, 1986]. Hence, PSI of the internal tide can only occur equatorward of the critical latitude where half the tidal frequency is greater than the local inertial frequency (*e. g.*, 14.52°N for K_1 and 13.44°N for O_1). Long believed to be too slow of a process to compete with other mechanisms of tidal dissipation, PSI was largely dismissed [*Olbers and Pomphrey*, 1981]. However, recent numerical, theoretical, and observational work has shown convincing evidence that near the critical latitudes the rates of PSI are vastly enhanced and may be a dominant part of the redistribution of energy throughout the internal wave spectrum [*Mackinnon and Winters*, 2005, *Young et al.*, 2008, *Alford*, 2008].

Although the main evidence for PSI in our dataset is the fortnightly modulation of the near-inertial band, a further clue comes from the "checkerboard" pattern that is visible in several locations in Figure 2.5d, indicating that the signal is often comprised of both upward and downward propagating waves. This bi-directional energy propagation is confirmed by a rotary spectral decomposition in depth [*Leaman and Sanford*, 1975]. See Figure 4 of *Girton et al.* [2011] for an illustration.

PSI is a "non-local" triad interaction that, in addition to the frequency criteria mentioned above, satisfies the wavenumber constraints: $k_1 + k_2 = k_i$ and $m_1 + m_2 = m_i$, where k and m are horizontal and vertical wavenumber, respectively, and subscripts i, 1, and 2 label the initial wave and first and second daughter waves, and the non-locality implies a scale separation between the daughter waves and the parent. Because of the near-inertial frequency and, hence, small aspect ratio (k/m) of the daughter waves, the implications of the wavenumber constraint are that the initial, low wavenumber wave would break down into an upward and a downward propagating wave with high vertical wavenumber, similar to what we observe here.

It is important to note that we only see evidence of this mechanism near 400 m. The localization is curious, and we are unsure of the characteristics in the water column or specifics

of the physical forcing that allow it to occur at this particular depth. One possibility is that perhaps this depth corresponds to the ray path of an internal tidal beam passing the mooring from a nearby generation site.

Evidence for PSI from Bispectra

An additional diagnostic for PSI that has been used previously [*Carter and Gregg*, 2006, *Sun and Pinkel*, 2010] is the bispectrum, or the normalized version—the bicoherence. Bicoherence is a quantity that shows whether or not a statistically dominant phase relationship exists for a wave triad, over the span of the record, that stands out above random phasing. The bicoherence is defined such that its magnitude at the frequency pair $[\omega_1, \omega_2]$ indicates the strength of the triad interaction between frequencies ω_1, ω_2, and $\omega_1 + \omega_2$. Following *Carter and Gregg* [2006] we perform a bicoherence analysis using the normalization of *Kim and Powers* [1979].

Bispectra and bicoherence are computed from each component of the velocity using ∼12 day half overlapping windows. We assume that the four non overlapping windows, and u and v, are independent giving us 16 degrees of freedom and calculate our levels of statistical significance following *Elgar and Guza* [1988]. Although an average over the entire vertical range from 50–800 meters does not show any statistically significant bicoherence, a vertical profile of bicoherence at the frequency pair $[\omega_1, \omega_2] = [f, f]$ (the key indicator for PSI) shows an isolated peak of significant bicoherence centered at 350 m (Fig. 2.8a), and the bicoherence at 350 m shows a narrow region of significant bicoherence near this frequency pair (Fig. 2.8b). 350 m is nearly the center of the band of tidally-modulated near-inertial energy in Figure 2.5d.

A vertical average over the shaded region from 250 to 500 m yields a vertical band averaged bicoherence of 0.281 which based on the increased degrees of freedom from the averaging, taking into account the vertical de-correlation scale, is significant at the 95% level.

Artificially-high bicoherence may be produced by vertical advection of velocity gradients [*McComas and Briscoe*, 1980, *Neshyba and Sobey*, 1975], but comparison of results before

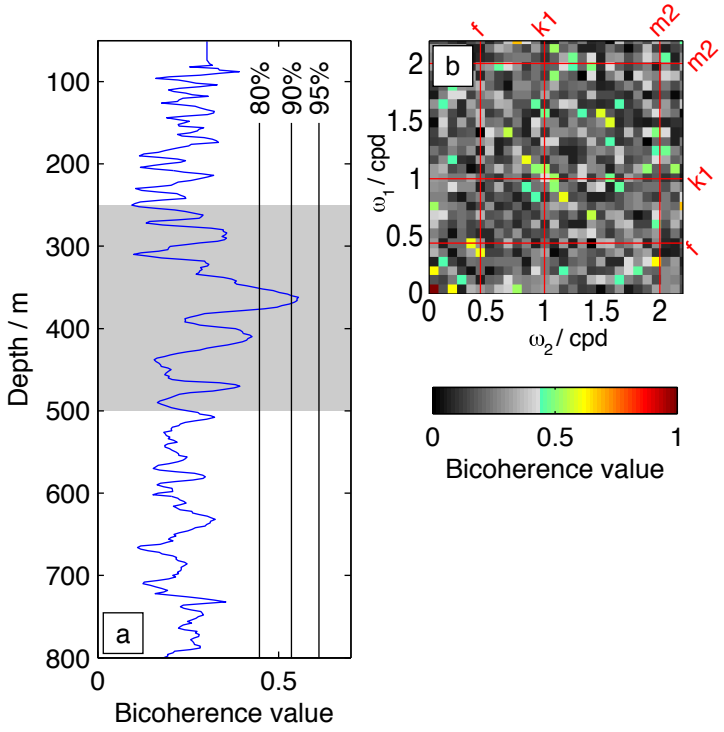

Figure 2.8: Results of bispectral calculations described in Section 4.1.4 following *Carter and Gregg* [2006] (a) Vertical profile of bicoherence at the (f, f) frequency pair (the principal indicator of PSI of the K1 tide). Vertical lines indicate the 80%, 90%, and 95% significance levels. (b) Bicoherence map at 360 m—the depth of the peak in panel a.

and after removing vertical advection (through isopycnal leveling via a semi-Lagrangian transformation [*Alford and Pinkel*, 2000]) shows that this is not likely to be a major effect in our dataset. The net result of the bispectral calculation is to add another piece of evidence (though far from conclusive) that PSI of the diurnal tide may be responsible for the mid-depth near-inertial energy at MP1.

2.5.2 Deep Rectilinear Inertial Motions

Briefly, we now move to the bottom of the water column at MP1 to look in detail at the near inertial motions making up the deep energy peak. The magenta trace in Figure 2.7c is a time series of twice the inertial BHKE averaged over the bottom 50 m of the water column.

This is the same depth range where we observe an intensification in inertial and tidal kinetic energy in our vertical profiles of Figure 2.3. Mean current ellipses (not shown) from inertial band velocities in this same depth range reveal extremely rectilinear motion oriented along the axis of the canyon, as opposed to the typically circular motion we would expect from inertial oscillations. Evidently the inertial band is responding to the presence of the canyon walls and behaving like a Kelvin or channel wave.

2.6 Mixing

While the importance of the Mindoro Strait to the throughflow transport between the South China and Sulu Seas has not yet been firmly established, the watermass differences between the two seas clearly requires some amount of mixing during the transit. The densest layers that flow through the strait are found crossing the Panay Sill as a dense overflow [*Tessler et al.*, 2010] with a substantially reduced salinity minimum (*i. e.*, higher salinity) than seen on the same density surface in the SCS. Applying a 1-D mixing argument as described by *Hautala et al.* [1996], this S change over a 100 m thick layer implies a diffusivity of $10^{-3}\,\mathrm{m}^2/\mathrm{s}$.

The moored profiler provides sufficient vertical resolution such that we can estimate dissipation of turbulent kinetic energy (ϵ) via a Thorpe scale analysis [*Thorpe*, 1977], applied following *Alford et al.* [2006]. Since temperature and salinity were observed to be highly correlated, potential temperature could be used rather than potential density, greatly simplifying the calculation owing to the absence of salinity spiking. Time–depth maps of ϵ smoothed with a Gaussian filter of five days length and 150 meters depth (Fig. 2.7d) reveal a low-frequency modulation at depth with sporadic events in the upper water column. The timeseries of dissipation averaged over the lower 200 m of the water column shows this even more clearly (Fig. 2.7c). The dissipation signal in the upper water column has little correlation with either of the tidal frequencies, whereas the signal at depth is clearly tied to the spring–neap cycle of the internal tide. Our analysis shows that the highest correlation with this dissipation signal is with the sum of the diurnal and semi-diurnal band HKE. Figure 2.7c shows that the large pulses of tidal BHKE are co-located in time with most of the high

values of ϵ, while large values of inertial BHKE only appear during a few epsilon peaks in mid February. In some cases, large peaks in inertial energy have no apparent signal of dissipation (*e. g.*, February 2).

The lack of a dissipation signal in the upper water column suggests that the energy that we believe is transferring from the diurnal internal tide to inertial motions is not breaking down locally and causing mixing but is propagating away, potentially providing energy to drive mixing further along in the channel.

Near the bottom of the water column, the observed correlation between the total internal tide and dissipation implies that the elevated mixing signal we are seeing is likely caused by the internal tide impinging on the sloping base of the canyon where it breaks and releases energy for mixing.

The average mid-water column diffusivity inferred using the *Osborn* [1980] relation ($\kappa_\rho = 0.2\epsilon/\overline{N^2}$) from density overturns (Fig. 2.3e) is approximately $10^{-5}\,\mathrm{m}^2/\mathrm{s}$ in the range of the strongest near-inertial wave energy. This is only moderately higher than typical open ocean background values [*Gregg*, 1989], and clearly not sufficient for dramatic watermass modification. However, it is worth noting that this small enhancement of mid-depth dissipation and diffusivity is consistent with the level of the shear spectrum (2.1×GM) at this latitude (12deg N) following the mixing parameterization of [*Gregg et al.*, 2003], assuming a shear–strain ratio of 7 as suggested by [*Kunze et al.*, 2006]. Some departure would not be surprising, due to the violation of the [*Gregg et al.*, 2003] assumptions by the coherence of the PSI waves, but the fact that the parameterization performs well nonetheless is encouragement to continue its use in other similar environments.

2.7 Conclusions

These two moored profiler records from either end of the Mindoro Strait in the Philippines illustrate some of the similarities and dramatic contrasts possible over fairly short distances within Archipelago topography. These differences manifest themselves not only in the mean vertical structure but also the temporal and spatial characteristics of the wavefield.

In summary,

- The northern site in the South China sea is more energetic than the southern site in the Sulu Sea in both the semidiurnal and diurnal bands.

- We find no evidence to support local or remote atmospheric forcing of intense thermocline (200–500 m deep) near-inertial motions.

- Due to the co-varying amplitude modulation as well as timeseries and bicoherence estimates of non-linear interactions, our results are highly suggestive of PSI of the diurnal internal tide as a generation mechanism for the thermocline near inertial motions.

- Elevated near-bottom dissipation has a clear spring–neap cycle and is tied primarily to the internal tide, suggesting that similar or greater levels of near-bottom mixing may exist between MP1 and Panay Sill, explaining the observed watermass transformation.

- Mid-depth diffusivity is insufficient to produce the watermass transformation seen in the dense overflow between the SCS and SS.

The evidence suggesting a PSI-generated near-inertial wave signal adds strength to the theory that PSI is a valid mechanism for internal wave generation both here and in the open ocean. Additionally, the variations in the internal wave field observed between MP1 and MP2 show that even within small regions of energetic internal wave activity, the wave field itself is highly variable and topographic interactions may play a role in defining the scales of this variability.

The phase lag between the hypothesized PSI-generated near-inertial energy and the internal tide forcing is a puzzle that we have not been able to resolve with our current dataset. Two possibilities include: (a) Saturation of the near-inertial wavefield (due to propagation or further breakdown) early on in the spring tide, results in an energy peak before the maximum in forcing; or (b) the majority of the internal tide signal observed at MP1 has propagated

from a remote generation site further away than the location of PSI. More detailed spatial coverage of measurements or theoretical consideration of the influence of bathymetry on the PSI process are likely needed to make progress on this question.

Our initial investigations have certainly just scratched the surface and more work is needed to fully understand the dynamics at work in this strait. It is our hope that the work presented herein is a starting point for future work in the region and motivation for more studies on the role of internal waves in low latitude archipelagos.

2.8 Acknowledgments

This research was funded as part of the ONR Archipelago Straits DRI, also known as PhilEx, by program managers Steve Murray and Scott Harper (Code 322) under grants N00014-06-1-0685, N00014-06-1-0737, and N00014-07-1-0927. We would like to thank the Captain and Crew of the R/V Melville for their assistance during shipboard operations as well as our colleagues from the Philippines, Laura David, Cesar Villanoy, and other collaborators. Finally, we are indebted to Andrew Cookson, Eric Boget, and John Mickett for logistical support as well as mooring design and construction.

2.9 Bibliography

Alford, M. (2008), Observations of parametric subharmonic instability of the diurnal internal tide in the south china sea, *Geophys. Res. Lett.*, *35*.

Alford, M. H. (2001), Internal swell generation: The spatial distribution of energy flux from the wind to mixed layer near-inertial motions, *J. Phys. Oceanogr.*, *31*(8), 2359–2368.

Alford, M. H., and M. C. Gregg (2001), Near-inertial mixing: Modulation of shear, strain and microstructure at low latitude, *J. Geophys. Res.*, *106*(c8), 16,947–16,968.

Alford, M. H., and R. Pinkel (2000), Observations of overturning in the thermocline: The context of ocean mixing, *J. Phys. Oceanogr.*, *30*, 805–832.

Alford, M. H., M. C. Gregg, and M. A. Merrifield (2006), Structure, propagation, and mixing of energetic baroclinic tides in mamala bay, oahu, hawaii, *J. Phys. Oceanogr.*, *36*, 997–1018.

Alford, M. H., et al. (2011), Energy flux and dissipation in Luzon Strait: two tales of two ridges, *J. Phys. Ocean.*, *41*(11), 2211–2222.

Cairns, J., and G. Williams (1976), Internal wave observations from a midwater float, 2, *J. Geophys. Res.*, *81*(12), 1943–1950.

Carter, G. S., and M. C. Gregg (2006), Persistent near-diurnal internal waves observed above a site of M 2 barotropic-to-baroclinic conversion, *J. Phys. Oceanogr.*, *36*(6), 1136–1147.

D'Asaro, E. A. (1985), The energy flux from the wind to near-inertial motions in the surface mixed layer, *J. Phys. Oceanogr.*, *15*(8).

Egbert, G. D., and S. Y. Erofeeva (2002), Efficient inverse modeling of barotropic ocean tides, *J. Atmos. Ocean. Tech.*, *19*, 183–204.

Elgar, S., and R. Guza (1988), Statistics of the bicoherence, *IEEE Trans. Acoust., Speech, Signal Proc*, *36*.

Eriksen, C. C. (1982), Observations of internal wave reflection off sloping bottoms, *J. Geophys. Res.*, *87*, 525–538.

Gargett, A. E., P. J. Hendricks, T. B. Sanford, T. R. Osborn, and A. J. Williams III (1981), A composite spectrum of vertical shear in the upper ocean, *J. Phys. Oceanogr.*, *11*, 1258–1271.

Garrett, C., and W. Munk (1975), Space-time scales of internal waves: A progress report, *J. Geophys. Res.*, *80*(3).

Girton, J. B., B. S. Chinn, and M. H. Alford (2011), Internal wave climates of the philippine seas, *Oceanography*, *24*(1), 100–111.

Gonella, J. (1972), A rotary-component method for analysing meteorological and oceanographic vector time series, *Deep-Sea Res.*, *19*, 833–846.

Gregg, M. C. (1989), Scaling turbulent dissipation in the thermocline, *J. Geophys. Res.*, *94*, 9686–9698.

Gregg, M. C., T. B. Sanford, and D. P. Winkel (2003), Reduced mixing from the breaking of internal waves in equatorial waters, *Nature*, *422*, 513–515.

Hautala, S. L., J. L. Reid, and N. Bray (1996), The distribution and mixing of Pacific water masses in the Indonesian Seas, *J. Geophys. Res.*, *101*(C5), 12,375–12,389.

Hotchkiss, F. S., and C. Wunsch (1982), Internal waves in Hudson Canyon with possible geological implications, *Deep-Sea Res.*, *29*, 415–442.

Kim, Y., and E. Powers (1979), Digital bispectral analysis and its application to nonlinear wave interactions, *IEEE Trans. Plasma Sci.*, pp. 120–131.

Kunze, E., L. K. Rosenfeld, G. S. Carter, and M. C. Gregg (2002), Internal Waves in Monterey Submarine Canyon, *J. Phys. Oceanogr.*, *32*, 1890–1913.

Kunze, E., E. Firing, J. Hummon, T. K. Chereskin, and A. M. Thurnherr (2006), Global abyssal mixing inferred from lowered ADCP shear and CTD strain profiles, *J. Phys Oceanogr.*, *36*(8), 1553–1576.

Leaman, K., and T. Sanford (1975), Vertical energy propogation of internal waves: a vector spectral analysis of velocity profiles, *J. Geophys. Res.*, *80*, 1975–1978.

Mackinnon, J., and K. Winters (2005), Subtropical catastrophe: Significant loss of low-mode tidal energy at 28.9, *Geophys. Res. Lett.*, *32*.

McComas, C., and M. Briscoe (1980), Bispectra of internal waves, *J. Fluid Mech.*, *97*(1), 205–213.

Muller, P., G. Holloway, F. Henyey, and N. Pomphrey (1986), Nonlinear interactions among internal gravity waves, *Reviews of Geophysics*, *24*(3), 493–536.

Nash, J. A., M. H. Alford, and E. Kunze (2005), Estimating internal wave energy fluxes in the ocean, *J. Atmos. Ocean. Tech.*, *22*, 1551–1569.

Neshyba, S., and E. J. C. Sobey (1975), Vertical cross coherence and cross bispectra between internal waves measured in a multiple-layered ocean, *J. Geophys. Res.*, *80*(9).

Olbers, D., and N. Pomphrey (1981), Disqualifying two candidates for the energy balance of oceanic internal waves, *J. Phys. Oceanogr.*, *11*, 1423–1425.

Osborn, T. R. (1980), Estimates of the local rate of vertical diffusion from dissipation measurements, *J. Phys. Oceanogr.*, *10*, 83–89.

Pawlowicz, R., B. Beardsley, and S. Lentz (2002), *Classical tidal harmonic analysis including error estimates in MATLAB using T TIDE*, vol. 28, 929-937 pp.

Pullen, J., J. D. Doyle, P. May, C. Chavanne, and P. Flament (2007), Monsoon surges trigger oceanic eddy formation and propagation in the lee of the philippine islands, *Geophys. Res. Lett.*, *35*.

Rainville, L., and R. Pinkel (2006a), Propagation of low-mode internal waves through the ocean, *J. Phys. Oceanogr.*, *36*, 1220–1236.

Rainville, L., and R. Pinkel (2006b), Baroclinic energy flux at the Hawaiian Ridge: Observations from the R/P FLIP, *J. Phys. Oceanogr.*, *36*(6), 1104–1122.

Simmons, H., M. H. Alford, C. Jackson, J. A. M. J. D. Nash, , A. Pickering, and L. C. St. Laurent (2011), Dynamic modeling of internal tides in the Luzon Straits, *Ocean Modelling*, *in prep*.

Sun, O., and R. Pinkel (2010), Subharmonic energy transfer from the semidiurnal internal tide at kaena ridge, Ph.D. thesis, UCSD.

Tessler, Z. D., A. L. Gordon, L. J. Pratt, and J. Sprintall (2010), Transport and dynamics of the Panay Sill overflow in the Philippine Seas, *J. Phys. Oceanogr.*, *40*, 2679–2695.

Thorpe, S. A. (1977), Turbulence and mixing in a scottish loch, *Philosophical Transactions of the Royal Society of London*, *286*.

Wyrtki, K. (1961), *Physical oceanography of the southeast Asian waters*, 2, University of California NAGA rept.

Young, W., Y. Tsang, and N. Balmforth (2008), Near-inertial parametric subharmonic instability, *J. Fluid Mech.*, *607*, 25–49.

Chapter 3

THE IMPACT OF OBSERVED VARIATIONS IN THE SHEAR-TO-STRAIN RATIO OF INTERNAL WAVES ON INFERRED TURBULENT DIFFUSIVITIES

3.1 Abstract

The most comprehensive studies of the spatial and temporal scales of diffusivity rely on internal wave parameterizations that require knowledge of fine scale shear and strain. Studies lacking either shear or strain measurements have to assume a constant ratio between shear and strain(R_ω). Data from 14 moorings collected during 5 field programs are examined to determine the spatial and temporal patterns in R_ω and the influence of these patterns on parameterized diffusivity. Time mean R_ω ranges from 1 to 10, with changes of order 10 observed over a broad range of scales. Temporal variability in R_ω is observed at daily, weekly, and monthly scales. Observed changes in R_ω could produce a 2-3 times change in parameterized diffusivity. Vertical profiles of R_ω, E_{shear} and E_{strain} (shear or strain variance relative to Garret Munk) reveal that both local topographic properties and wind variability impact the internal wave field. Time series of R_ω from each mooring have strong correlations to either shear or strain, often only at a specific range of vertical wavenumbers. Sites fall into two categories, in which R_ω variability is dominated by either shear or strain. Linear fits to the dominant property (i.e., shear or strain) can be used to estimate a time series of R_ω that has an RMS error that is 30% less than RMS error from assuming $\mathrm{R}_\omega = 3$. Shear and strain level vary in concert, as predicted by the GM model, at high E_{shear} values. However, at $\mathrm{E}_{shear} < 5$, strain variations are 3 times weaker than shear.

3.2 Introduction

Internal waves are the dominant sources of finescale velocity variance in the frequency range from f (local inertial) to N (Brunt–Väisälä) and are important contributors to mixing the abyssal ocean [Munk and Wunsch, 1998, Egbert and Ray, 2000]. They act as intermediaries between narrowband forcing mechanisms (e.g., tides and storms) and eventual dissipation into heat. By breaking, these waves produce mixing that brings dense cold water formed at high latitudes to the surface at lower latitudes.

Microstructure based studies have shown that vertical diffusivity is highly variable and differs by several orders of magnitude across different topographic domains and forcing regimes. Polzin et al. [1997] report that over a large topographic feature, specifically the Mid Atlantic Ridge, diffusivity was enhanced by more than a factor of 10 ($0.1 \times 10^{-4}\mathrm{m}^2\mathrm{s}^{-1}$ in the basin, $> 10^{-4}\mathrm{m}^2\mathrm{s}^{-1}$ over the ridge). Ferron et al. [1998] report values of $\kappa = 1000 \times 10^{-4}\mathrm{m}^2\mathrm{s}^{-1}$ at the exit of the Romanche fracture zone, while Gregg and Sanford [1980] found values significantly below $\kappa = 1 \times 10^{-4}\mathrm{m}^2\mathrm{s}^{-1}$ in the Sargasso Sea.

The paucity of direct diffusivity measurements limits the predictive capability of ocean models. Numerical studies have shown that the abyssal density structure and circulation are sensitive to the values used for diffusivity as well as its horizontal and vertical structure [Jayne, 2009, Melet et al., 2013, Harrison and Hallberg, 2008]. Samelson [1998] evaluated the response of the overturning circulation and deep stratification to localized regions of intense mixing. He reports that edge-intensified mixing, as opposed to a constant basin wide diffusivity, produced abyssal stratification that better resembled existing observations. Since we cannot sample every region directly, it is necessary to understand how different forcing regimes contribute to mixing so that we can infer the mixing states of unsampled regions.

Direct turbulence measurements are challenging, requiring instruments capable of measuring velocity variance on centimeter scales. Several techniques have been developed to estimate vertical diffusivity based on more easily measured quantities. These include overturning scales of active turbulence [Thorpe, 1977] as well as finescale shear and strain of the

internal wave field[Gregg, 1989, Polzin et al., 1997].

Estimates of vertical diffusivity from measurements of finescale shear and strain via fine scale parameterizations have been calculated for several large data sets to study the spatial variability of mixing. Kunze et al. [2006] use shear and strain from lowered acoustic Doppler current profilers and conductivity temperature depth casts (CTD) taken during the World Ocean Circulation Experiment (WOCE) and subsequent hydrographic cruises.

More recently, groups have applied the parameterization to data from the ARGO network of profiling floats [Whalen et al., 2012, Wu et al., 2011]. However, because ARGO floats do not provide velocity measurements, both of these studies had to assume that the shear to strain ratio is a constant (Whalen et al. [2012] assume $R_\omega = 3$ while Wu et al. [2011] use $R_\omega = 7$); we test this assumption and its consequences here.

Whalen et al. [2015] show agreement between microstructure based diffusivity and parameterized diffusivity to about a factor of 2–3. We hypothesize that much of this scatter is due to the assumption that R_ω is a temporally invariant constant of 3. With a novel data set, we investigate this hypothesis by applying the finescale parameterization to vertical profiles from 16 McLane Moored Profilers (MP) in a variety of locations encompassing a broad range of spatial scales, temporal scales, and local forcing environments. The MP provides sufficient data to compute parameterized diffusivity with actual measurements of both shear and strain and to examine the consistency of the methods that rely on only one or the other, as well as to study the temporal variability of the input fields that drive the finescale parameterization. Our goal is to understand how the local internal wave state influences variability in R_ω, and what limitations assumptions about R_ω impose on the ability to resolve variability in diffusivity and explain the inconsistencies in previous comparisons.

3.3 Data

The data examined here represent many years of work and 5 separate field programs. Numerous articles have been published based on these experiments (See appendix for a brief description of each program and a list of references). This study is the first use of these

data together as a set. The experiments cover both the open ocean and continental shelf and encompass variability in latitude, wind forcing, topography, and barotropic tidal amplitude. Figure 3.1 shows all of the mooring locations on a global map and table 3.1 lists basic deployment parameters for each site.

The data considered are from MP measurements exclusively. The MP is a wire crawling instrument that is equipped with a CTD and a velocimeter that provides records of salinity, temperature, pressure, and east (u) and north (v) velocity. The MP traverses the wire with a mean speed of $25 - 35$ cm s^{-1} and can provide 2-m vertical resolution and on average 1.5-hr spacing between samples, though this varies as a function of depth and profiling ranges. Within the MP archive, range covered by a single MP varies from ≈500 to 2000 m with additional range coming at the cost of nominal time interval. Previous calculations have shown that frequency and wavenumber content can be resolved, without contacting the instrument noise floor, out to a vertical wavenumber of $k_z \approx 0.10$ cycles per meter (cpm) and to a frequency of $\sigma \approx 10$ cycles per day (cpd). Some deployment sites contain multiple stacked MPs for higher temporal resolution over a given depth range; these sites are marked on the map with a green asterisk (Fig. 3.1)

3.4 Methods

3.4.1 Finescale parameterizations

Finescale parameterizations of turbulent dissipation are based on models that predict the rate at which energy flows through the internal wave spectrum towards smaller scales and the idea that this rate is proportional to measurable scales of shear or strain variance [McComas and Müller, 1981, Henyey et al., 1986]. Finescale is regarded as fluctuations that are typically from 1–100 m in the vertical while microscale is where molecular processes such as viscosity and diffusivity begin to have an impact (about 1 m to 1 mm).

Parameterized diffusivities have been compared to observations by many investigators including Gregg [1989], Polzin et al. [1995], Gregg et al. [2003]. They compared estimated

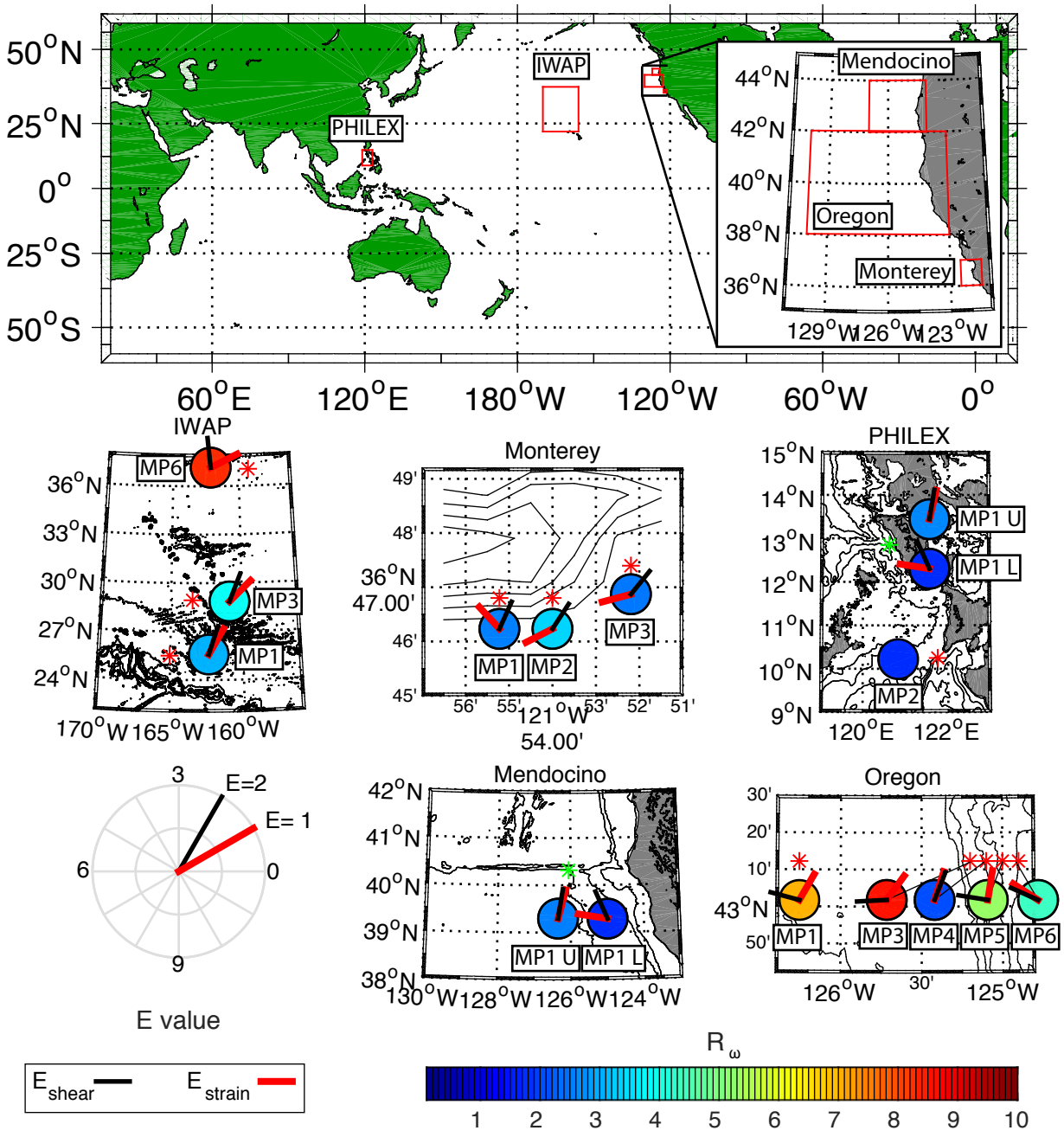

Figure 3.1: Experimental sites including bathymetry. Circle color indicates time mean R_ω and direction lines indicate mean E_{shear} and E_{strain} values. The red lines corresponds to E_{strain} and the black lines corresponds to E_{shear} and the value is indicated by radial position according to the guide in the lower left corner. Moorings with more than one MP on the wire show each MP separately labeled U(upper) and L(lower) with the actual position marked by the red asterisk.

dissipation rates with direct dissipation measurements from microstructure profilers (The Advanced Microstructure Profiler, the Multi-Scale Profiler, and HRP) and report agreement to within a factor of two.

Finescale parameterizations relate vertical diffusivity to shear variance ($< V_z^2 >$) and strain variance ($< \xi_z^2 >$) relative to the Garrett Munk (GM) spectrum through a mixing efficiency γ ($\kappa = \gamma\epsilon/N^2$, Osborn [1980]). Following Kunze et al. [2006], this takes the form of

$$\kappa_{v_z} = \kappa_o \; E_{shear} \; h_1(R_\omega) j \left(\frac{f}{N}\right) \tag{3.1}$$

with

$$E_{shear} = \frac{< V_z^2 >^2}{< V_z^2 >_{GM}^2} \tag{3.2}$$

$$h_1(R_\omega) = \frac{3(R_\omega + 1)}{2\sqrt{2} R_\omega \sqrt{R_\omega - 1}} \tag{3.3}$$

$$R_\omega = \frac{< V_z^2 >}{\bar{N}^2 < \xi_z^2 >} \tag{3.4}$$

$$j(f/N) = \frac{f acosh(N/f)}{f_{30} acosh(N_o/f_{30})} \tag{3.5}$$

and constants

$$\kappa_o = 5 \times 10^{-6} m^2 s^{-1}$$

$$f_{30} = 7.2920 \times 10^{-5} rad \; s^{-1}$$

$$N_0 = 5.2 \times 10^{-3} rad \; s^{-1}$$

R_ω (3.4), the shear to strain ratio, is the ratio of the buoyancy frequency normalized shear variance to strain variance. A single linear internal wave has an R_ω governed by its dispersion relation. It provides a measure of the aspect ratio and frequency content of the wave. For a single wave in the absence of a mean flow it can be expressed as

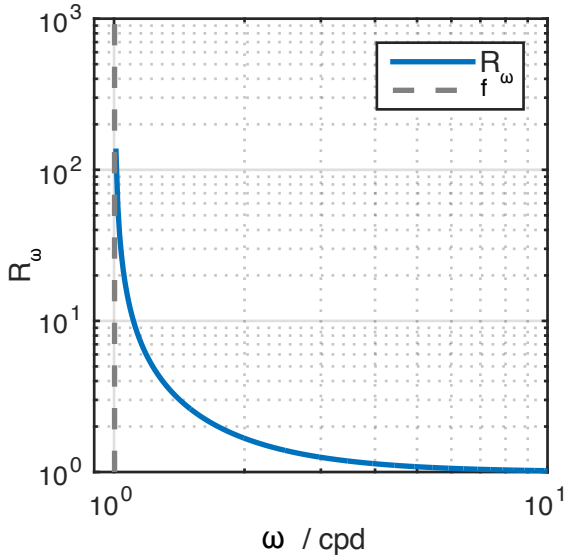

Figure 3.2: R_ω computed at 30 degrees north as a function of frequency to illustrate the different R_ω values that exist in the internal wave band. Vertical dashed line shows the local inertial frequency.

$$R_\omega = \frac{(\omega^2 + f^2)(N^2 - \omega^2)}{N^2(\omega^2 - f^2)}. \tag{3.6}$$

Equation (3.6) (and shown graphically in figure 3.2) conveys that near inertial waves (whose motions are predominantly horizontal) have a high shear to strain ratio (high shear low strain) while for waves near N (whose motions are predominantly vertical) the opposite is true.

The latitudinal dependence of the parameterization is given by $j(f/N)$. This term is a correction for the observed weaker turbulent dissipation rates at the equator [Gregg et al., 2003] as well as the predicted weaker wave–wave interaction rates.

Shear variance is calculated by integrating the vertical wavenumber spectrum of shear ($\Phi_{V_z}(k_z)$) from $k_0 = 1/(\text{record length})$ up to a critical wavenumber, k_c, defined as (3.7)

$$< V_z^2 >= \int_{k_0}^{k_c} \phi_{V_z}(k_z) dk_z = .661 N^2. \tag{3.7}$$

Strain variance is computed as the integral of the strain spectrum over this same wavenumber band.

$$< \xi_z^2 >= \int_{k_0}^{k_c} \phi_{\xi_z}(k_z) dk_z \tag{3.8}$$

In addition to (3.1), the parameterization can also be formulated in terms of strain variance relative to GM instead of shear as

$$\kappa_\xi = \kappa_o \; E_{strain} \; h_2(R_\omega) \left(\frac{f}{N} \right) \tag{3.9}$$

$$E_{strain} = \frac{< \xi_z^2 >^2}{< \xi_z^2 >_{GM}^2} \tag{3.10}$$

$$h_2(R_\omega) = \frac{1}{6\sqrt{2}} \frac{R_\omega (R_\omega + 1)}{\sqrt{R_\omega - 1}} \tag{3.11}$$

This is the formulation used by Whalen et al. [2012] because ARGO floats do not provide velocity measurements.

Because the MP measures both velocity and density, we are able to compute time varying shear variance, strain variance, and therefore time varying shear to strain ratio. With this information we can estimate parameterized diffusivity in a variety of ways. Here we consider four permutations of computed diffusivity,

- $\kappa_{v_z}^{var}$: E_{shear} with a time varying R_ω
- κ_ξ^{var}: E_{strain} with a time varying R_ω
- $\kappa_{v_z}^{const}$: E_{shear} with an assumed constant for R_ω
- κ_ξ^{const}: E_{strain} with an assumed constant for R_ω

$\kappa_{v_z}^{var}$ and κ_ξ^{var} yield the same time series of diffusivity because with the actual time varying R_ω the parameterizations (3.1) and (3.9) are consistent. $\kappa_{v_z}^{const}$ would be computed if we only

had velocity information and assumed that $R_\omega = 3$, while κ_ξ^{const} would be computed if we only had strain information and made a similar assumption about R_ω. This is the approach taken by Whalen et al. [2012] and Wu et al. [2011]. The subscript indicates the equation used ($\kappa_{v_z} \rightarrow$ (3.1) and $\kappa_\xi \rightarrow$ (3.9)) while the superscript indicates if a time varying or a constant R_ω is used.

Figure 3.3a shows an example of these four time series of diffusivity computed for the southern most mooring, MP1, from the IWAP experiment. It highlights the scale of variability in diffusivity that can be introduced via assumptions about R_ω.

Separations between κ_ξ^{var} and $\kappa_{v_z}^{var}$ are manifestations of the shear to strain ratio diverging from 3. If $\kappa_{v_z}^{var}$ is greater than κ_ξ^{var} it implies an $R_\omega > 3$ and if κ_ξ^{var} is greater than $\kappa_{v_z}^{var}$ it implies $R_\omega < 3$. Effectively, the difference between the red and green curve (figure 3.3) shows the resultant discrepancy between computing diffusivity using (3.1) and an assumed constant for R_ω and the actual time varying R_ω. Similarly, the difference between the black and green curve (figure 3.3) shows the resultant discrepancy between computing diffusivity using (3.9) and an assumed constant of R_ω and the actual time varying R_ω. Figure 3.3b shows the time series of R_ω used to compute the four diffusivity traces shown in panel a.

Figure 3.3a,b highlight variability of R_ω on a broad range of time scales. Apparent is a large deviation from $R_\omega = 3$ between year days 120 and 126 and smaller deviations on the order of 1–2 days in the rest of the time series. Additionally, we see a slow steady decrease in R_ω from year day 130 and on. The large deviation in R_ω from year days 120–126 produces a mean deviation in diffusivity of a factor of 2-3 between κ_ξ^{const} and $\kappa_{v_z}^{var}$, with peak deviations of about a factor of 8. This represents significant error when attributing shear or strain variability to mixing variability.

3.4.2 Shear vs strain error

The parameterizations (3.1) and (3.9) are consistent with each other in that with the correct instantaneous (true) R_ω one can produce the same parameterized diffusivity from either shear alone or strain alone. When the actual shear to strain ratio is not known, however,

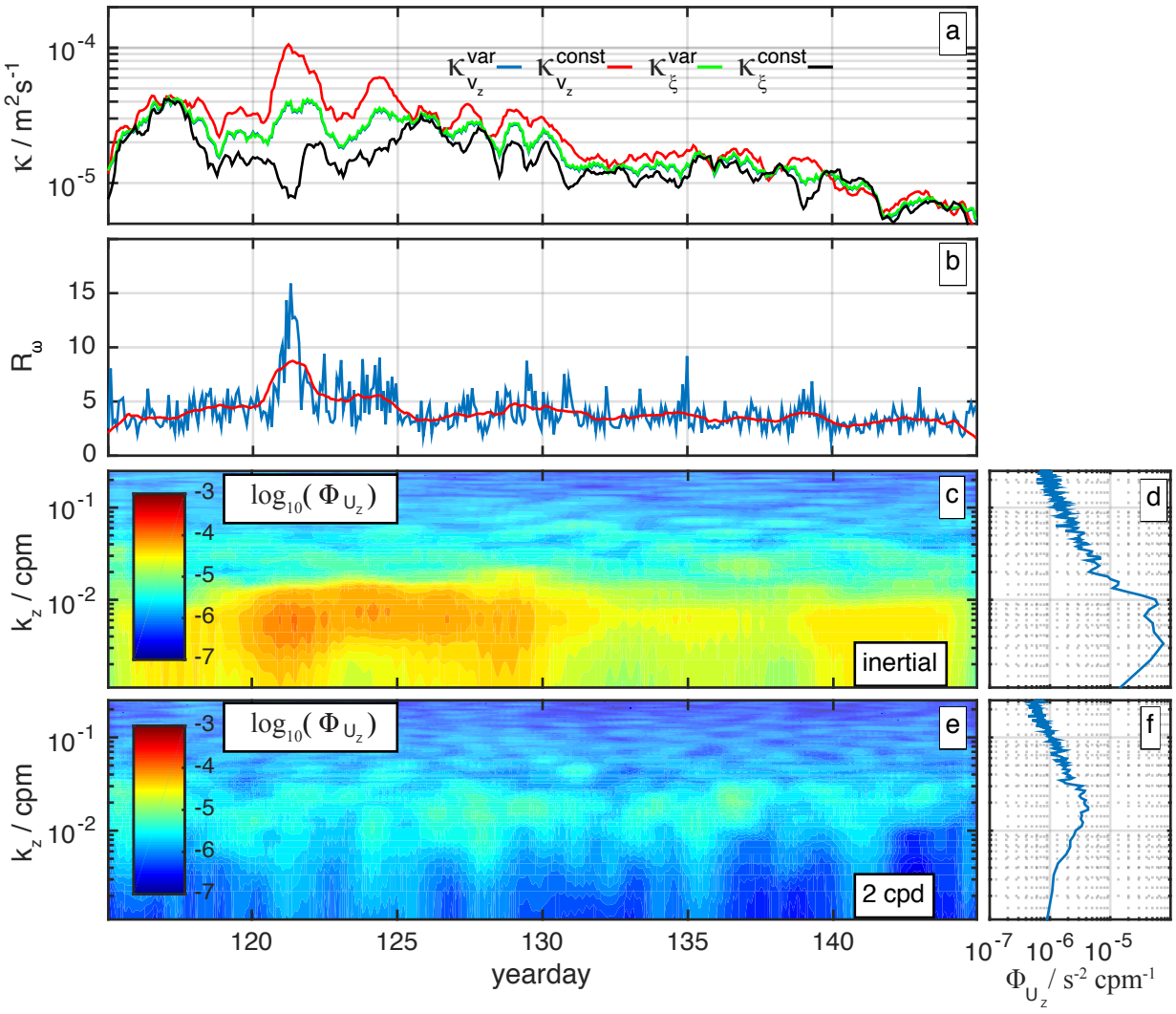

Figure 3.3: Site analysis of the IWAP MP1 mooring showing; a) diffusivity computed using (3.1) and (3.9) and an assumed constant of $R_\omega = 3$ and full time varying R_ω. The blue curve is lying directly beneath the green curve because the strain based parameterization and the shear based parameterization produce the same diffusivity when the true time varying R_ω is used. b) Time series of R_ω and time series of R_ω smoothed by a 1.25 day moving average filter. Time wavenumber frequency band passed spectra of vertical shear(c and e) along with the time mean spectrum (d and f) for the IWAP MP1 mooring (c,d) near inertial, e,f) semidiurnal). Time wavenumber near inertial shear spectral density shows a strong pulse of near inertial variance density from year days 120-125 that has a very limited wavenumber bandwidth and is strongly correlated to $R\omega$.

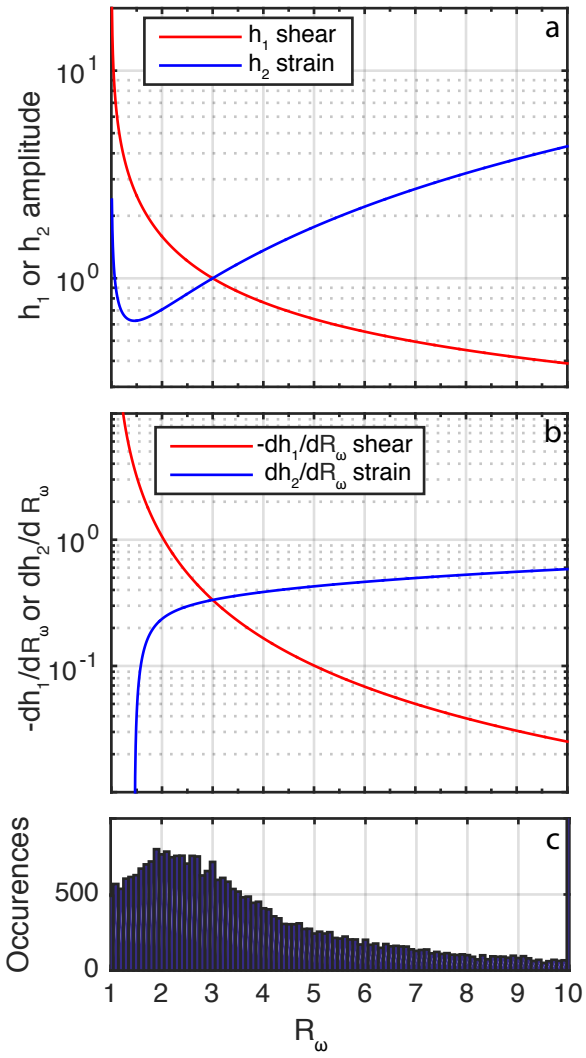

Figure 3.4: a) Curves of h_1 and h_2 as a function of R_ω used in shear and strain parameterizations highlighting the differences in relative error when computing diffusivity using (3.1) or (3.9) when actual R_ω is > 3 or < 3. b) Curves of dh_1/dR_ω and dh_2/dR_ω illustrating how the sensitivity of diffusivity to error in R_ω is a function of mean R_ω. c) Histogram of R_ω from smoothed time series from all of the moorings combined.

the error associated with incorrectly assuming R_ω from (3.1) and (3.9) is not the same (Fig. 3.4a).

Assuming a shear to strain ratio of 3, $h1$ and $h2$ both provide a value of 1. However, if the

actual value is $R_\omega = 10$, h1 and h2 are actually $h1 = .38$ and $h2 = 4.32$. If all other variables remain constant, the strain based parameterization would be underestimating diffusivity by 4.32 times while the shear based parameterization is overestimating by 2.5 times. The relative error in the strain based parameterization caused by incorrect assumptions in R_ω is 200% greater than the error associated with incorrectly assuming R_ω and using a shear based parameterization. Inversely, where actual $R_\omega < 3$, the relative error due to an incorrect assumption of R_ω is less when strain is used.

The histogram of instantaneous values of R_ω from all of the MP data shows a distribution covering both regimes, but with more samples corresponding to $R_\omega < 3$ (figure 3.4c). The histogram was computed from time series of R_ω that were smoothed with a 1/4 day filter. Values span a broad range from 0.8 to greater than 10 with a mean of 3.97. The corresponding h1 and h2 curves show that the observed variability in R_ω, and associated deviations from $R_\omega = 3$, could produce order of magnitude differences in h1 and h2.

This implies that for sites with $R_\omega > 3$ shear only parameterizations are a better choice, while for $R_\omega < 3$ strain only would be the better choice.

3.5 Analysis procedure

We compare and contrast a variety of quantities at each of the sites. To make clear the analysis procedures and to define the quantities used, we present a detailed case study of the southern most mooring from the IWAP experiment, MP1.

The IWAP experiment was designed to study the fate of the M2 internal tide as it propagates away from its generation sites along the Hawaiian ridge. Previous work has shown a complex field where nonlinear interactions such as parametric subharmonic instability are at play transferring energy out of the low mode tide [Alford et al., 2007, MacKinnon et al., 2013b,a]. Pickering et al. [in prep.] shows that there is a complex near inertial wave field with upward and downward propagating wave packets in both the upper and lower portions of the sampling regimes.

The signature of these near inertial waves is apparent in the U velocity field (Figure 3.5a).

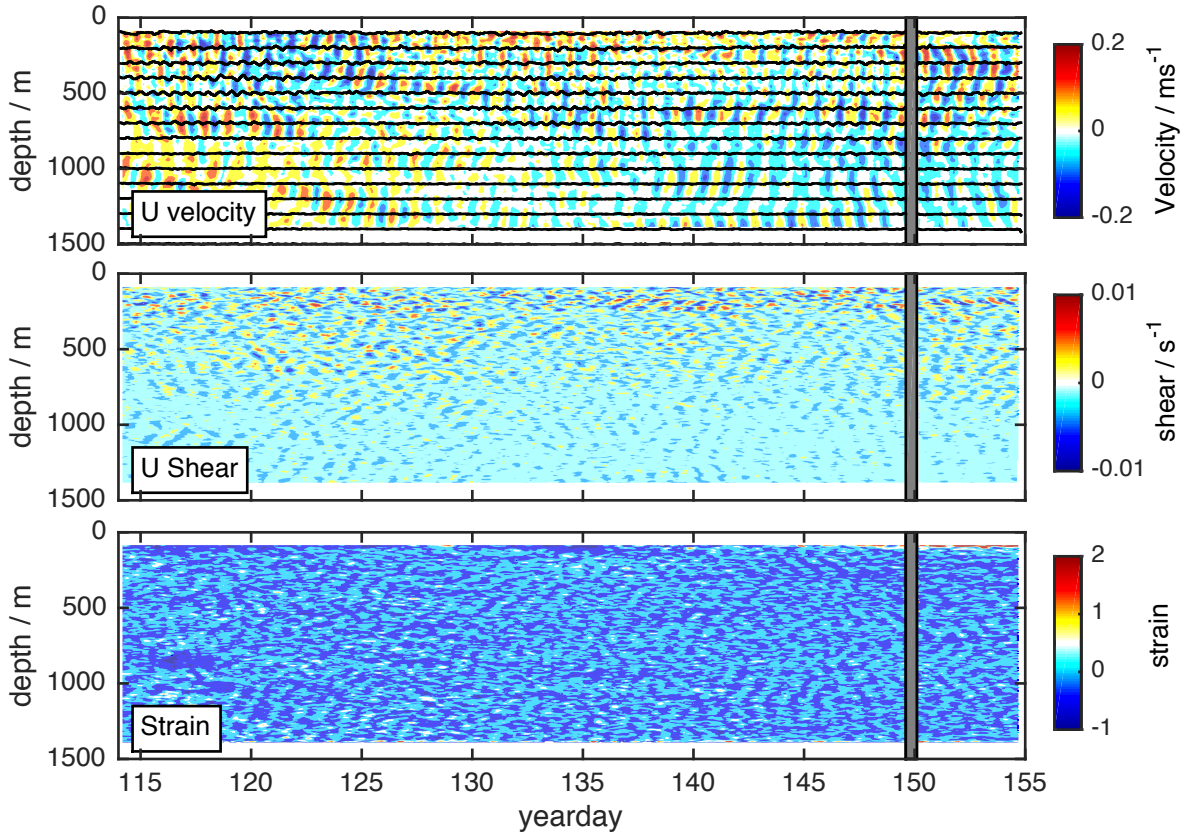

Figure 3.5: IWAP MP1 mooring showing a) U velocity and isopycnals, b) U shear, and c) strain.

The strong sloping lines of phase are the characteristic signal of internal waves viewed in an Eulerian reference frame. Upward phase propagation corresponds to downward energy propagation while downward phase propagation corresponds to the opposite. A checkerboard pattern is indicative of the coexistence of both upward and downward propagating waves. Previous work has used this pattern as a potential indicator of parametric subharmonic instability [Alford et al., 2007, Chinn et al., 2012].

The following analysis explores how this variability influences the shear to strain ratio.

3.5.1 Mean R_ω

Following the methods described in section 3.4.1, we computed time mean shear and strain spectra. Spectra were computed for each profile by computing the mean spectra from half overlapping 300 m windows with the time mean spectra being the average of all of the profile spectra. At IWAP MP1, both shear and strain exceed the levels predicted by the GM model (Fig. 3.6a).

The ratios of shear and strain variance to GM, E_{shear} and E_{strain}, reveal that MP1 has 2.4 times as much shear variance as GM and 2 times as much strain variance as GM. The resulting time mean R_ω for this site is 3.6 ± 0.9. Despite significantly more shear and strain variance than GM, R_ω is very close to the GM value. The error bounds for R_ω are computed as the maximum error possible assuming that the spectral error for shear and strain are perfectly oppositely correlated. It represents a worst case scenario for error. The upper R_ω confidence limit is computed as the variance in the upper 95% confidence limit of the shear spectrum divided by the lower 95% confidence limit of the strain spectrum with the lower confidence limit on R_ω computed as the opposite. Degrees of freedom for error analysis are computed by estimating a decorrelation time scale for shear variance and strain variance and assuming values separated by this scale are independent. The shear spectrum shows a high wavenumber increase with a slope of k^{+2} that is consistent with white noise in velocity with an RMS velocity variance of $V_{rms} = 1$ cm/s. This noise floor is above k_c and therefore does not contaminate the calculation of $< V_z^2 >$.

The impact of uncertainty in R_ω on diffusivity can be approximated from the gradient of h_1 and h_2 (Fig. 3.4b) as

$$\epsilon_{h_x} \approx \epsilon_{R_\omega} \frac{dh_x(R_\omega)}{dR_\omega}. \tag{3.12}$$

At IWAP MP1, this results in a value for h1, and error in h1 from error in R_ω, of $h_1 = 0.783 \pm 0.159$. This represents a factor of 1.5 in diffusivity.

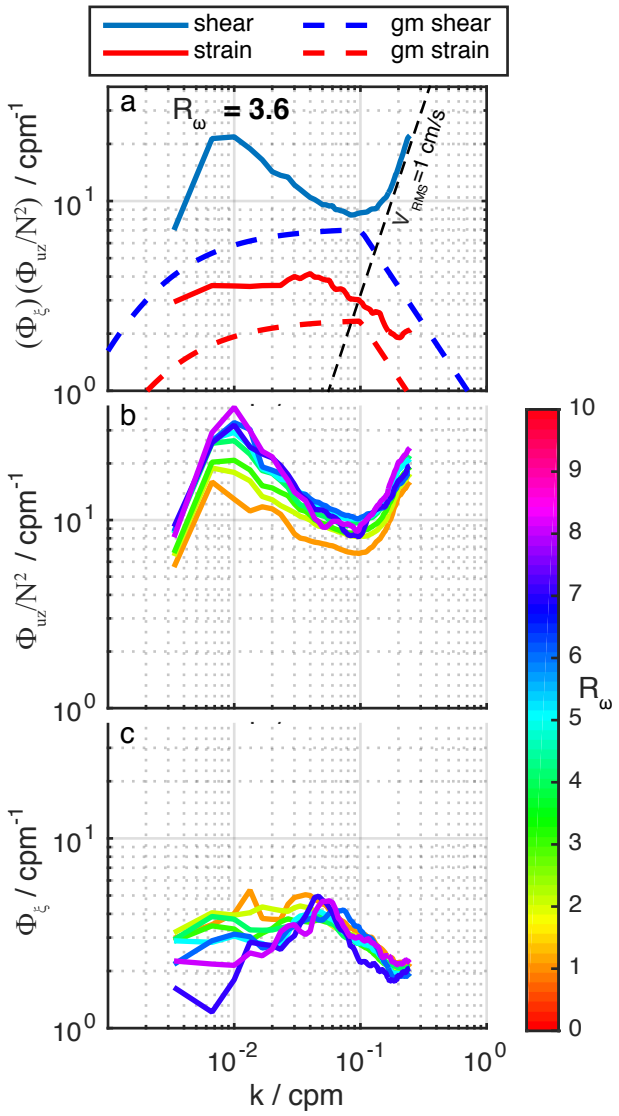

Figure 3.6: a) Time mean spectra of stratification normalized shear and strain and GM spectra showing elevated shear and strain spectra but with a near GM R_ω of R_ω = 3.6. Dashed line shows b) Stratification normalized wavenumber spectrum of shear as a function of R_ω. c) Wavenumber spectrum of strain as a function of R_ω.

3.5.2 Time varying R_ω

Mean values of R_ω can obscure the existence of significant features and variability. Instead of computing R_ω from time mean spectra, we now compute R_ω for each profile and examine

the time series of R_ω. The time series of R_ω from IWAP MP1 shows a uniform slow decrease from year day 125 onward with a large period of elevated R_ω between year days 120 and 125 (Fig. 3.3b). According to the full finestructure parameterization this elevated period of R_ω would produce large diffusivities that would be missed if only considering mean R_ω and only measuring strain.

The effect of R_ω deviations from an assumed value of 3 results in a discrepancy between diffusivity predicted with shear only or strain only and the diffusivity computed with full time varying R_ω (Fig. 3.3a). As a first step in establishing the root cause of variations in R_ω we examine how spectral levels vary with R_ω.

From mean spectra of shear and strain associated with different values of R_ω we observe variability in both the shear spectra and the strain spectra. However, variations in shear spectral level show a more ordered correlation with respect to R_ω (Fig. 3.6b,c). This consistent relationship between shear level and R_ω, and the lack of one between strain level and R_ω, is an indicator that at this site, shear based processes are in control of R_ω. We use this result as evidence to drive further analysis and to substantiate our later claims about the causes of variability in R_ω at this site.

3.5.3 Frequency distribution of R_ω variability

In our observations, near inertial waves and internal tides are generally the strongest frequencies of internal waves. Because each wave has a different signature in terms of R_ω (near inertial waves have high shear and low strain while internal tides have lower shear and higher strain) we hypothesize that the overall structure in R_ω may be tied strongly to the presence or absence of energy in these bands.

To determine how the frequency distribution of shear influences R_ω we band pass filter the velocity data into inertial (f), diurnal (1 cpd), and semidiurnal (2 cpd) bands. We then Fourier transform in depth to get time-varying shear spectral density or $\Phi_{u_z}(k, t, \omega_i)$. Figure 3.3b,e show the inertial and semidiurnal $\Phi_{u_z}(k, t, \omega_i)$ fields for IWAP MP1 as well as the time mean wavenumber spectrum (panels d and f) for each frequency band. It should be noted

that at the latitude of this mooring the inertial frequency is too close to 1 cpd to effectively separate inertial motions from the diurnal tide. Because of this, we omit the diurnal plot and show only the near inertial, noting that it may contain diurnal tidal signals. Figure 3.6e shows that in time there is a relatively uniform level of 2 cpd shear spectral density with a peak value at a wavelength of 90 m. Time varying near inertial shear spectral density (figure 3.6c), however, has a large increase between year days 120 and 130 at wavelengths of 100–300 m. This corresponds to the time period of observed increased R_ω indicating that in this case R_ω rises because of near–inertial shear.

3.5.4 Wavenumber distribution of correlation

To quantify this observed correlation between near inertial shear and R_ω, we compute the correlation coefficient (r) between the previously computed time series of R_ω and each wavenumbers' time series of variance density for each of the 3 frequency bands.

$$r(k, \omega_i) = corr(\Phi_{uz}(k, t, \omega_i), R_\omega(t)) \tag{3.13}$$

This produces a wavenumber profile of band passed correlation coefficients (Fig. 3.7).

The strongest correlation exists between near inertial/1cpd motions and R_ω, with little observed correlation between semidiurnal shear and R_ω. Peak correlation is at a wavelength of 100m and has a correlation coefficient of $r = 0.52$. Wavenumbers that have a correlation coefficient that fails the student T test for statistical significance are not shown. Curiously, the observed correlation peak does not have the same broad shape as seen in the time mean spectrum of band passed shear (a recurring feature that will be discussed later).

A similar calculation yields a wavenumber profile of correlation coefficients for band passed strain. As opposed to shear, in strain we are looking for strong negative correlations between strain variance and R_ω because increasing strain causes a reduction in R_ω. At this site, no strong correlations between strain variance and R_ω were observed.

3.5.5 Vertical structure in R_ω

Because the wavenumber correlation exists at such a distinct scale, and is a size that does not span the entire water column, we consider the vertical structure of R_ω to deduce the role of vertical fluctuations in shear variance. We compute mean vertical profiles of R_ω by calculating R_ω in 300 m half–overlapping windows and then temporally averaging.

Figure 3.8 shows a time depth map of R_ω, the time mean vertical profile of R_ω, and vertical profiles of E_{shear} and E_{strain}. The vertical profiles show an average decrease in R_ω with depth. However, this trend is dominated by the strong impulse in near inertial shear variance between yeardays 120 and 125.

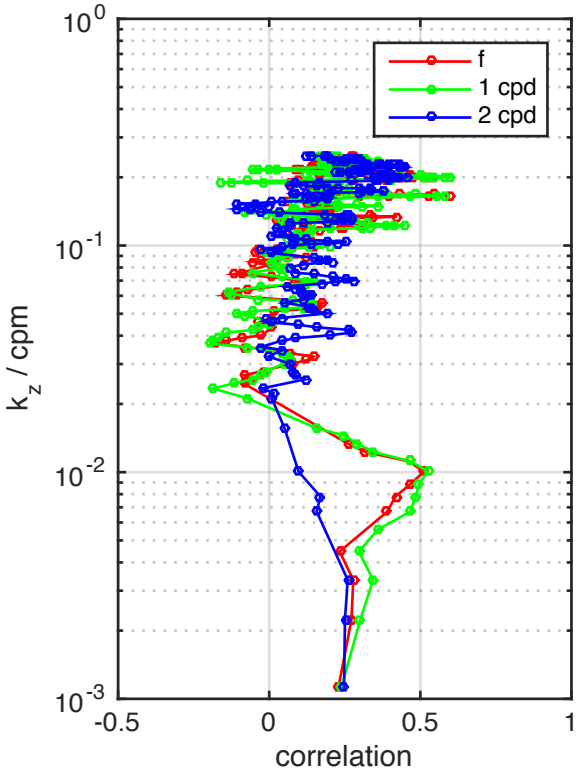

Figure 3.7: Wavenumber profile of band passed correlation coefficient from $\rho(\Phi_{u_z}(k), R_\omega)$ at IWAP MP1. Shows that R_ω is strongly temporally correlated to 100m scale near inertial energy

We observe increasing E_{shear} at the bottom of the profile with a mid depth minimum. E_{strain} is relatively flat above 800m, but then increases consistently towards 1100m. The changes in R_ω as a function of depth are caused by a combination of the vertical variations in shear and the vertical variations in strain.

3.5.6 Modeling R_ω from shear and strain

Ideally, we wish to estimate diffusivity from only partial knowledge of the wave field (shear only or strain only). As noted, the mean value of R_ω, and therefore the structure of the local wavefield, plays a role in determining the optimal parameter (shear or strain) in terms of error caused by an incorrect assumption of constant R_ω. Because the mean value of R_ω is close to 3, there is minimal difference in relative error from the assumption of constant R_ω in h1 vs h2 (shear only parameterizations or strain only parameterizations would produce similar error). However, because our previous analysis at IWAP MP1 showed strong correlations between

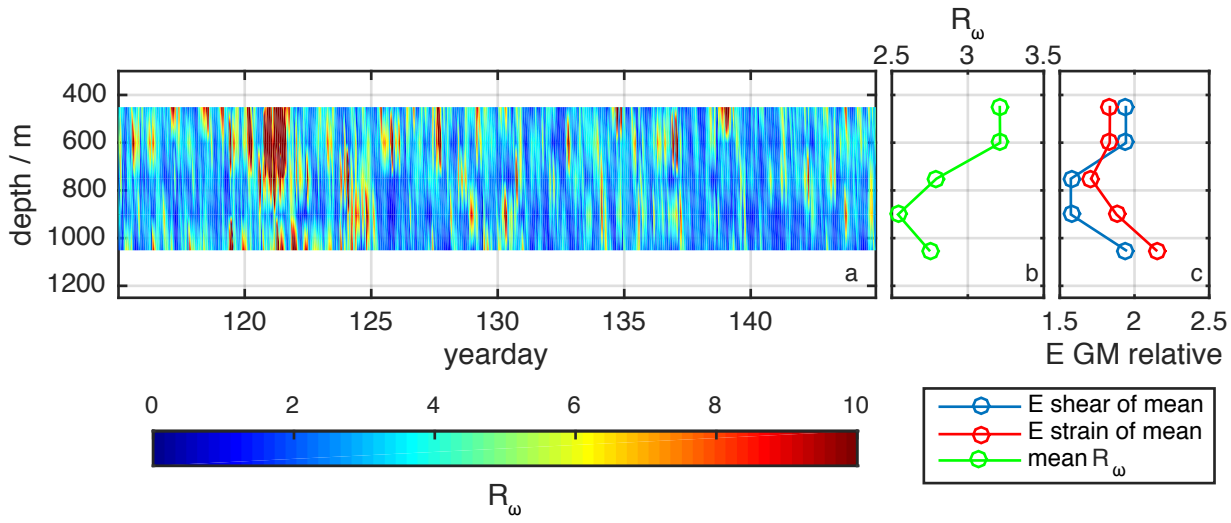

Figure 3.8: Time depth map of R_ω(a) and time mean vertical profiles of R_ω(b), E_{shear} and E_{strain} (c) at IWAP MP1 reveals a variable vertical structure in R_ω with episodic elevated values of R_ω at the surface. Surface intensification of R_ω and strong correlations to near inertial shear spectral density imply that the dominant source of R_ω forcing at this site is surface generated near inertial motions.

near inertial shear and R_ω, we hypothesize that the best estimator of R_ω would be some function of shear variance. To examine this relationship we compute the linear regression between shear variance and R_ω and strain variance and R_ω. In both cases we use normalized shear and strain variance computed as

$$\frac{< V_z^2 > (t)}{< V_z^2 >_{max}} \quad \text{or} \quad \frac{< \xi^2 >^{-1} (t)}{< \xi^2 >_{max}^{-1}} \tag{3.14}$$

such that shear and strain variance $\in [0, 1]$. We compute a line of best fit that minimizes the sum of the squared error for both normalized shear and normalized strain vs R_ω(Fig. 3.9). Shear variance vs R_ω has a strong linear trend that does not occur in strain. The line of best fit for shear vs R_ω has a slope of 8.2 and an $R^2 = 0.315$ while the best fit for strain variance vs R_ω has a slope of 3.0 and an $R^2 = 0.04$. This correlation confirms what we anticipated, there is a stronger relationship between variability in R_ω and shear variance than for strain variance.

Despite this correlation, there is a series of elevated R_ω values that are represented poorly by our fit. This region of elevated R_ω corresponds to the period of year days 120–125, where we determined that elevated levels of near inertial shear variance were increasing local R_ω (Fig. 3.3). Even with full knowledge of the shear and strain fields at the site, it is difficult to make a single regression that represents both the background fluctuations in R_ω as well as strong narrowband events. Despite this fact, we are able to predict R_ω with less error than assuming a constant value of 3. At this site a constant $R_\omega = 3$ produces a root mean square deviation (RMSD) of 2.2 from the observed R_ω, while our linear model using shear alone produces a time series of R_ω that has an RMSD of 1.0.

3.5.7 IWAP MP1 analysis conclusions

In conclusion, we find that while the mean value of R_ω at this site is close to GM, shear and strain levels are both significantly elevated relative to GM (Fig. 3.6). We also find large amplitude short time (O(7 day)) variability in the shear to strain ratio driven by 100

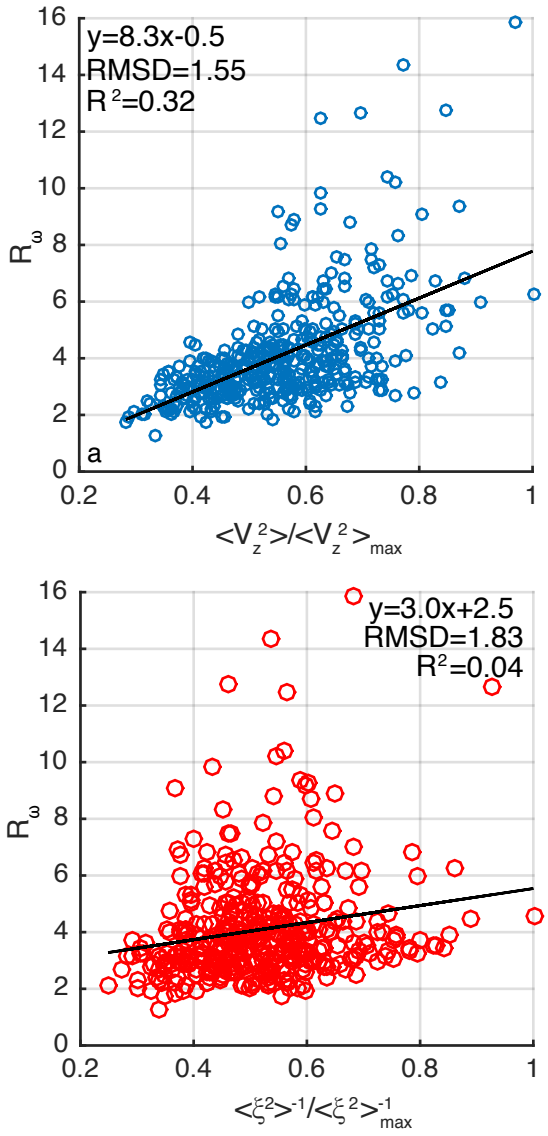

Figure 3.9: Scatter plot and lines of best fit for normalized a) shear vs R_ω and b) normalized strain vs R_ω at IWAP MP1. Reveals a strong positive correlation between R_ω and total shear variance. R^2 is significantly larger for shear fit vs strain indicating that the best model for R_ω using a single measured quantity would be a function of shear and not strain.

m narrow band near inertial activity focused in the upper part of our measurement range between 500 and 700 m depth and that the variability in R_ω can best be predicted by shear variance. Inertial correlation is evident in the profile of correlation coefficients (Fig. 3.7)

and also in the time series (Fig. 3.3). These conclusions are summarized along with similar results from the other moorings in figures 3.10 and 3.11.

3.6 Results and structure of R_ω

Following the same analysis procedures, aggregated results from all mooring data are presented. We discuss observed patterns and trends from the dataset, as well as provide detailed descriptions of notable observations at particular sites.

3.6.1 Mean values and temporal scales

Figure 3.1 shows values of R_ω for each MP as well as E_{shear} and E_{strain} defined as the mean spectral variance relative to that predicted by the GM spectrum. Numerical values for R_ω with uncertainties are shown in Table 3.1.

All values are computed as averages over the entire range of the water column sampled. Results show that in all cases the spectral levels for both shear and strain are elevated above GM. The only outlier is E_{strain} at IWAP MP6, which is not statistically different from 1. Seven of the sites have E_{shear} greater than E_{strain} while five sites have E_{shear} less than E_{strain}. At the other four MPs, E_{shear} is equal to E_{strain}. E_{shear} and E_{strain} are not shown in Fig. 1 for the southern mooring from Philex (MP2) because the values are off the scale with E_{shear} reaching a level of 21 and E_{strain} reaching 24. As can be seen in these records, despite having elevated values of E_{shear} and E_{strain}, it is possible to have a GM $R_\omega = 3$ so long as $E_{shear} \approx E_{strain}$.

Time mean shear to strain ratios span a broad range from a minimum of 0.8 to a maximum of 10.4. Ten out of 16 records have a $R_\omega > 3$ and six have an $R_\omega < 3$ (a good representation of both regimes from figure 3.4). Because all values of E_{shear} and E_{strain} are above GM, the mean level relative to GM of one quantity does not correlate to the value of R_ω; R_ω above and below 3 with elevated shear and strain are apparent.

Time series of R_ω from the sites display many temporal scales of variability. At IWAP MP1 near inertial events triggered large shear events producing R_ω variability of O(7 days).

We also observe variations in R_ω with a period from 3 – 30 days. We do not observe a spring neap cycle in R_ω at any of the sites.

3.6.2 Spatial patterns

Only two of the field programs had mooring lines spanning large enough distances to potentially highlight spatial patterns. The IWAP mooring line spanned $\approx$ 1400 km while the ORE05 line spanned $\approx$ 100 km (Fig. 3.1). The IWAP moorings show a general increase in R_ω moving away from the Hawaiian Ridge. This trend in R_ω occurs because of a relatively systematic reduction in E_{strain} from MP1 to MP3 to MP6 in the inertial, diurnal, and semidiurnal bands. The increase in R_ω from MP3 to MP6 also coincides with an increase in E_{shear} that further contributes to the increasing R_ω. The decrease in strain may be caused by the weakening of the internal tide beam as it propagates away from the Hawaiian Ridge. This does not, however, explain the trend in near inertial strain or the increase in shear from MP3 to MP6.

In contrast, ORE05 has no continuous trend in R_ω. We observe elevated R_ω offshore at MP1 and MP3, followed by a reduction at MP4, before increasing towards the coast. The four most offshore moorings have similar levels of E_{strain}. This implies that the variations in R_ω are due to changes in shear variance. This uniformity in E_{strain} is surprising as MP1 is located far offshore, while the other sites are on the slope and have different characteristics [Martini et al., 2011]. The large change in R_ω observed at MP3 is due to a reduction in shear level. Previous work has shown that the ORE05 site is influenced by a combination of local forcing, remote forcing, and the offshore eddy field impacting the phasing of the internal tides[Kelly and Nash, 2010, Osborne et al., 2011, Martini et al., 2011, Nash et al., 2007]. This variable forcing along with highly inhomogeneous bathymetric roughness could provide sufficient opportunity for abrupt small scale spatial variations in R_ω such as we observe from MP3 to MP4 to MP5. However, the exact mechanism remains unknown.

3.6.3 Wavenumber distribution of correlation

Computing wavenumber profiles of band passed correlation coefficient between shear or strain and R_ω for every mooring reveals a clear separation between the magnitudes of various correlation coefficients at each site. Seven out of 16 sites show the greatest correlation between R_ω and shear variance while the remainder are more correlated with strain variance. Because of the magnitude of the disparity in the correlations, we only show the parameter (shear or strain) associated with the largest correlation with R_ω and each frequency band – inertial, diurnal, and semidiurnal (Fig. 3.10).

Of particular interest is that many of the sites show a narrow band of wavenumbers with strong correlations. As with the narrow correlation peak between shear variance and R_ω from IWAP MP1 (section 3.5), many of the other sites have similar narrowband correlations, but they appear not only in shear but in strain as well. The implication is that at sites with these narrow peaked correlation functions, R_ω is responding to a specific frequency of forcing as well as a particular vertical scale.

The other IWAP moorings used in this analysis show slightly different patterns than IWAP MP1. IWAP MP3 shows a strong correlation between R_ω and near inertial and diurnal shear but it does not have the same narrow wavenumber structure as at MP1. MP3 has a double peaked correlation with peaks at 166m and at 50m. MP6 also shows this double peaked correlation function but it is shifted to higher wavenumbers with the peaks at 133m and 330m. Additionally, at MP6 we see a stronger correlation with semidiurnal shear than at either of the other IWAP moorings.

All three of the MPs from Philex have R_ω strongly correlated with strain yet they all have a different wavenumber structure. The lower MP at the MP1 mooring shows a distinct peak in correlation coefficient with semidiurnal 20m strain. The upper MP at MP1 shows strong correlations in both diurnal and semidiurnal strain but at different wavenumbers. The 2 cpd peak is quite broad with the largest amplitude at 50m, while the 1 cpd peak is centered at 160m and is less broad. MP2 has far less separation between the inertial, diurnal, and

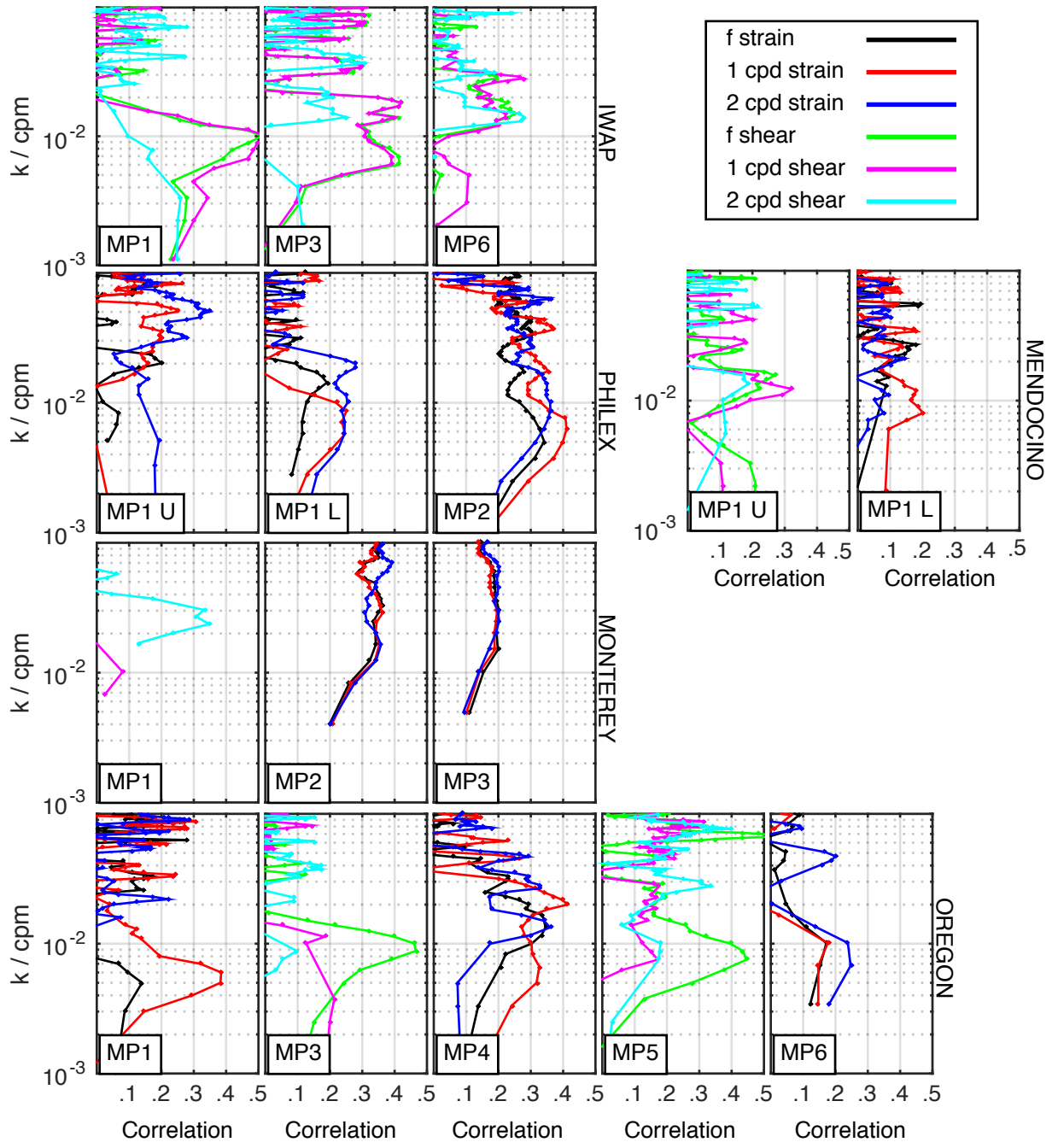

Figure 3.10: Wavenumber profiles of bandpassed correlation coefficient between shear or strain and R_ω for every MP to highlight the frequent occurrence of narrow band wavenumber correlation peaks in both shear and strain. Correlations failing the student T test for statistical significance are not shown.

semidiurnal R_ω–strain correlation coefficients.

Similar to the Philex MP1 mooring, the Mendocino mooring has both upper and lower MPs. However, as opposed to Philex MP1, R_ω at the upper and lower profilers at Mendocino are correlated with different parameters. R_ω from the upper MP at Mendocino is correlated with shear in all three frequency bands at scales between 50 and 100m. The lower MP, however, has the strongest correlation between R_ω and strain at diurnal frequencies and 100m scales.

The ORE05 moorings have similar spatial variability in R_ω correlation wavenumber structure as was observed in mean R_ω values. That is, there is no consistent pattern progressing towards the coast. The moorings alternate between R_ω strongly strain correlated and strongly shear correlated. MP1 shows a strong correlation peak at 200m in diurnal strain while MP3 has a near inertial correlation peak at 110m and MP5 has a strong near inertial correlation peak at 125m. The existence of large but persistent changes in R_ω over small distances highlights the importance of having a highly localized understanding of the shear and strain state of a location in order to reduce scatter in parameterized estimates of diffusivity (e.g., knowledge of the shear and strain field at MP3 does not aid in predicting R_ω at MP4).

3.6.4 Vertical structure

Figure 3.11 shows vertical profiles of R_ω, E_{shear}, and E_{strain} computed from half overlapping 300 m windows for all sites that have sufficient vertical range. This allows us to determine the way shear and strain covary with depth and how those changes influence R_ω. A range of behaviors within the set of E_{shear}, E_{strain}, and R_ω profiles is apparent.

At every mooring E_{strain} is either increasing with depth or constant. Sites with E_{strain} increasing are typically records that approach the bottom. Oregon MP3-MP5 are relatively shallow moorings on the continental shelf, Philex MP1 and MP2 are located upstream and downstream of a narrow channel in an archipelago, while the Mendocino MP1 mooring is north of the Mendocino escarpment. Increasing strain with depth appears indicative of a

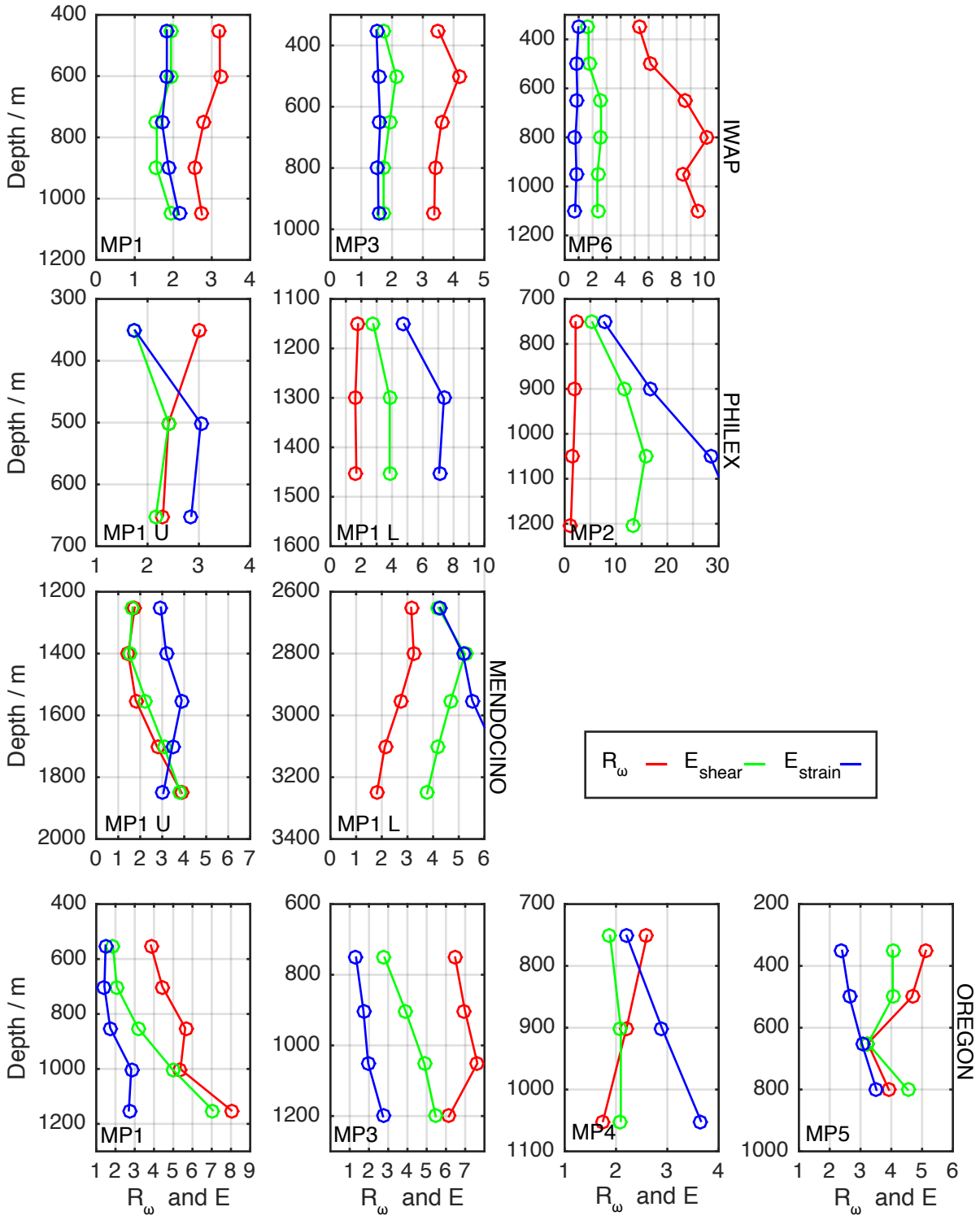

Figure 3.11: Vertical profiles of R_ω and E_{shear} and E_{strain}

strain process that is heavily influenced by topographic interaction and proximity to the bottom.

As opposed to E_{strain}, the data used contain examples of E_{shear} increasing, decreasing, and remaining constant as a function of depth. This indicates that shear variance is possibly driven by phenomena with a more complex vertical structure, and potentially from multiple generation mechanisms.

We expect that sites with strong wind generated near inertial activity would exhibit decreasing E_{shear} with depth as the surface generated near inertial waves weaken as they progress deeper. However, there are counter examples.IWAP MP6 shows E_{shear} increasing with depth, despite being an open ocean site that is expected to be strongly driven by the atmosphere. This increase with depth is potentially caused by mid depth nonlinear interactions or could be the high mode "wake" from previous winters storms [Pickering et al., in prep.].

Mendocino has a unique E_{shear} signature with a mid-depth maximum at ≈2000m. The Mendocino region contains internal tides generated to the south at the Mendocino escarpment. Alford [2010] reports that this depth range is very close to where the predicted ray paths of semidiurnal tidal beams would fall. This implicates topographically generated internal tide rays as a source of mid depth variations in R_ω. As internal tides can propagate large distances, it also illustrates the potential for local changes in R_ω being caused by remote disturbances.

We have identified that the vertical structure of R_ω can be strongly influenced by both shear and strain. Key influences appear to be topographic interactions, near inertial waves from atmospheric forcing or nonlinear interactions, and narrow band tidal beams. The maximum change in R_ω in the vertical for a single MP is 4, with a typical amplitude of variation being 1. For this set of sites the impact of vertical structure in R_ω, though potentially important, is less significant than spatial and temporal variability.

3.6.5 Fits

If the shear to strain ratio could be inferred from either E_{strain} or E_{shear} alone it would allow for significant improvements in our ability to estimate diffusivity. Correlations between shear or strain and R_ω are complicated functions of frequency, wavenumber, and depth, and are subject to temporal variations in forcing. However, our analysis has shown that in general at each site either shear or strain is the better predictor. In an attempt to find a parameterized relationship between shear or strain and R_ω we perform a set of linear regressions and discuss the resulting projections of shear and strain variance into R_ω.

We classify our fits as local because they are solely dependent on the shear and strain information present at the mooring itself. In these fits we are only considering the vertical mean dependence of R_ω. Despite showing the existence of vertical structure in R_ω, E_{shear}, and E_{strain}, we omit it here for simplicity.

Quality of fitting

Here, we use R^2 computed between shear or strain variance and R_ω as a metric of fit quality. R^2 is defined as

$$R^2 \equiv 1 - \frac{\sum(y_i - y_{fit})^2}{\sum(y_i - \bar{y})^2}. \tag{3.15}$$

where $\bar{y}$ is the average value of the observations. A high R^2 indicates how well observed values fit a statistical model. In this case, it explains how well R_ω is modeled by our linear fits from shear or strain. For the majority of sites our results show that there is a significant separation in R^2 between shear and strain local fits (Fig. 3.12). That is, either strain or shear sets R_ω. We find that in general, sites that are in shallow water or near large constraining topographic features have have a higher R^2 in strain (Philex sites and at the Montery Canyon (MC09) sites). However, we do not observe this same relationship in the near shore ORE05 moorings as may be expected given their relatively shallow depths.

The IWAP moorings all have the highest R^2 for the linear fit between shear variance and

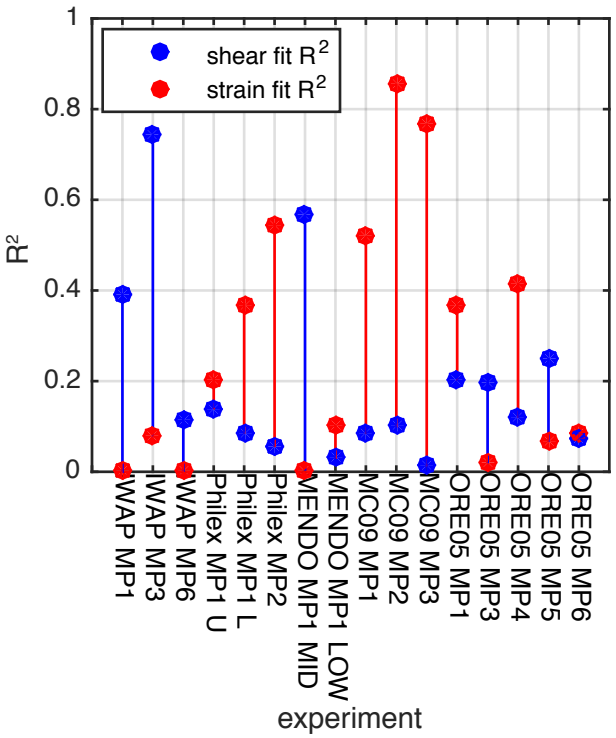

Figure 3.12: R^2 for local shear vs R_ω and strain vs R_ω highlighting the clear separation in R^2 magnitude for shear vs strain on a site by site basis. Bar color denotes if shear or strain has a higher R^2 for clarity.

R_ω as well as the upper MMP from the MENDO MP1 mooring. The lower MP from the MENDO MP1 shows a weaker separation between shear and strain R^2 with strain having a slightly better fit. This vertical pattern in fit quality transitioning from shear to strain as a function of depth at the MENDO MP1 mooring is similar to that observed in E_{shear} and E_{strain}, which shows E_{strain} far exceeds E_{shear} in the lower mooring while at the mid depth MP the averages are very similar. This connection between fit quality and shear or strain level reinforces the dominance of one or the other at each location.

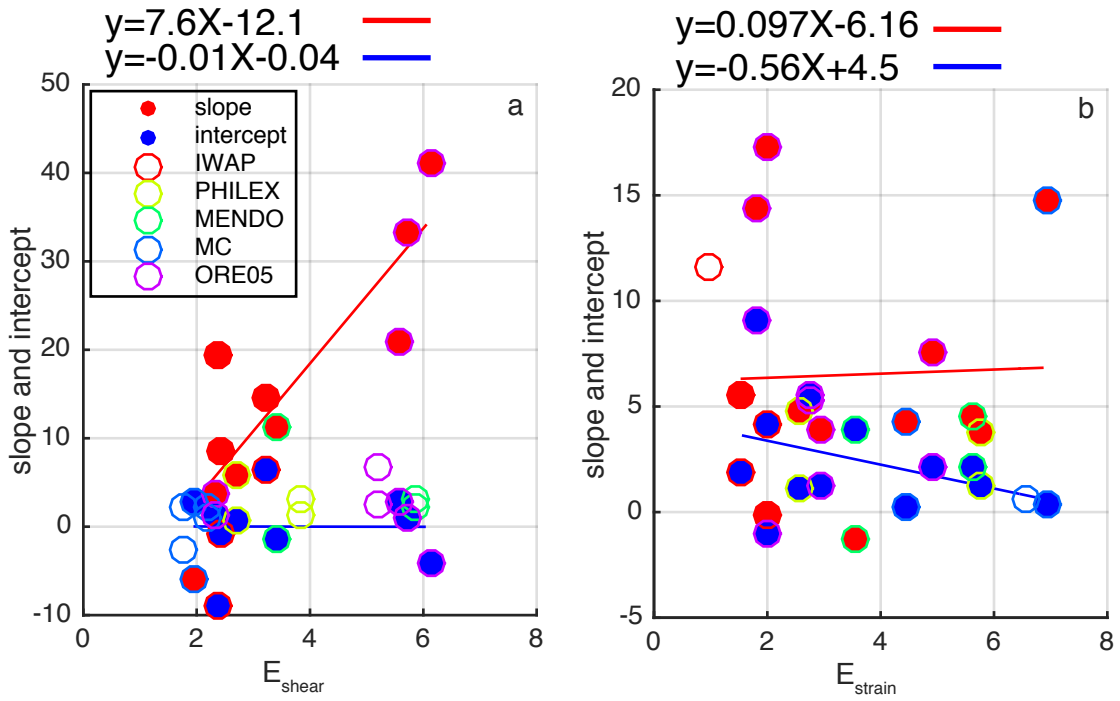

Figure 3.13: Lines of best fit through scatter plots of slope and intercept from a) local shear vs R_ω and b) local strain vs R_ω. Color of dot correspond to slope and intercept while halo color indicates experiment. We see a strong functional dependance between slope of local shear vs R_ω and time mean E_{shear} while shear vs R_ω intercept remains constant regardless of E_{shear}. Strain global fit shows a decrease in both slope and intercept of local strain vs R_ω as a function of E_{strain}.

Local fit properties vs mean E_{shear}/E_{strain}

In addition to the above separation between sites by shear or strain dominance, the slope of the dependence of R_ω and shear or strain appears to scale with overall energy level across all sites. As an example, plotting the slope and y intercept of all the linear local fits versus time mean E_{shear} and E_{strain} reveals a strong relationship (Fig. 3.13).

Local shear fits show a positive correlation between slope and E_{shear} with the intercept value being largely independent of E_{shear}(Fig. 3.13a). Strain local fits show a different pattern with both slope and intercept lines having a flat slope (Fig. 3.13b). These clear relationships

illustrate the potential influence of shear and strain on R_ω but have only limited predictive capabilities.

Error in projections of R_ω

Estimates of R_ω for each of the sites based on the optimal local fit (fit with highest R^2) are computed along with RMSD relative to the actual time series of R_ω. Additionally, a similar RMSD calculation is performed for a constant of $R_\omega = 3$. At all sites the optimal local fit produces lower values of RMSD when compared to one using a constant $R_\omega = 3$ (table 3.2). On average, local fits provide a 30% improvement in RMSD when compared to $R_\omega = 3$. The implication is that by having a good characterization of a site it is possible to estimate a time varying R_ω that is a significant improvement over choosing $R_\omega = 3$.

3.6.6 R_ω as a function of E_{shear}

The GM model has a constant shear to strain ratio regardless of E_{shear} level when shear and strain are both integrated to the critical wavenumber. In order to maintain a constant R_ω, as shear increases, strain must increase equally.

The calculation of R_ω produces a constant shear variance of $0.661 N^2$ (3.7), regardless of E_{shear}, but has a time varying k_c. Because of this, we will use k_c as the basis for a temporally varying metric for shear level. At vertical wavenumber less than k_c, the ratio of the average spectral levels is

$$E_{shear} = \frac{\overline{\Phi_{shear}^{observed}}}{\overline{\Phi_{shear}^{GM}}} = \frac{0.1}{k_c} \tag{3.16}$$

Bin–averaged strain variance, computed by integrating the strain spectrum out to k_c shows the resultant average dependence of strain variance as a function of E_{shear} (Fig. 3.14a). A histogram of E_{shear} values observed in our records reveals a skewed distribution with an average of ≈ 3 (Fig. 3.14b).

The horizontal black line at 0.221 shows the strain variance needed to produce $R_\omega = 3$

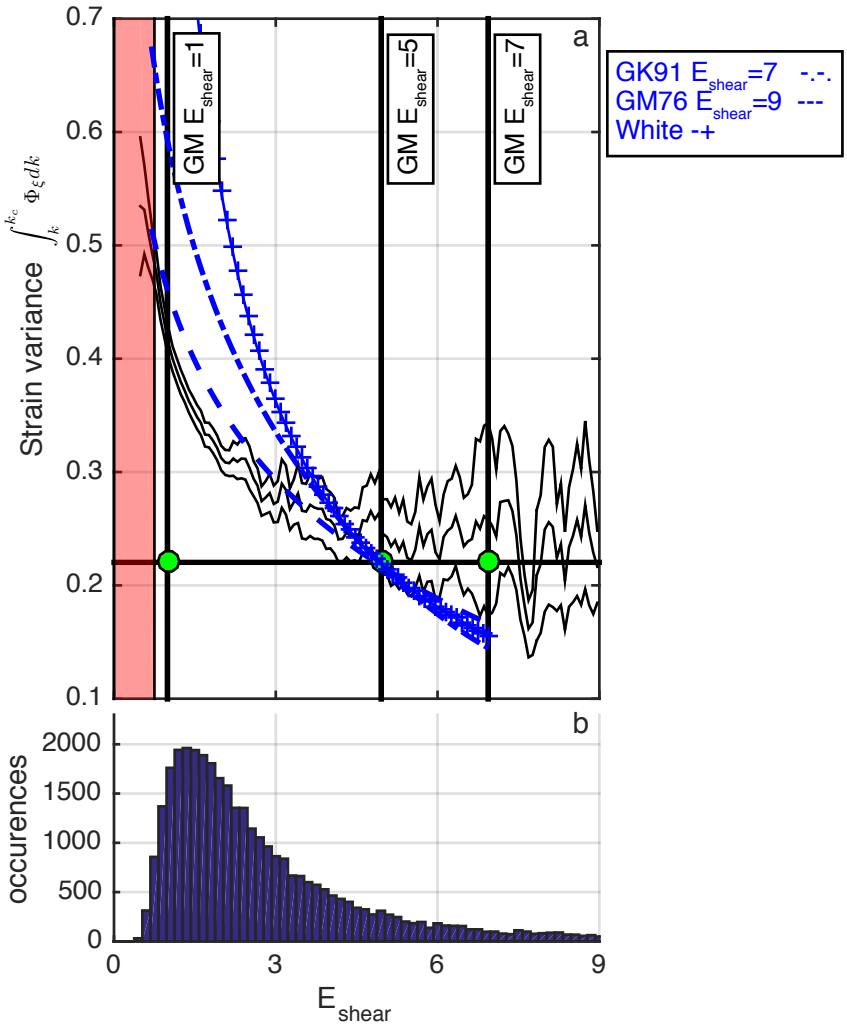

Figure 3.14: (caption on the following page)

Figure 3.14: a) Strain variance as a function of E_f level computed from k_c (section 3.6.6). Horizontal black line is the behavior predicted by GM model corresponding to $R_\omega = 3$. Black lines show the mean value of strain variance as a function of E_{shear} and standard error. Blue dashed lines show strain variance as a function of E_{shear} for a GM76 $E_{shear} = 9$ and a Gk91 $E_{shear} = 7$ spectrum that have been held at a constant level and integrated out to increasing levels of k_c to provide strain variance as a function of E_{shear}. Here GM76 refers to the standard GM model using the parameters from Garrett and Munk [1975] while GK91 refers to the GM model but makes use of the parameters from Gregg and Kunze [1991]. The blue -+ curve shows a similar computation but with a white strain spectrum whose level is set such that it converges to the observations at E_{shear}=5. These model curves have similar shape to the observed behavior in that the levels increase as E_{shear} decreases however they do not asymptote towards a constant strain variance in the region of $E_{shear} > 4$. The solid blue curve is a spline fit to the data with the constraint that the slope=0 at $E_{shear} = 5$. The shaded red region corresponds to E_{shear} levels with corresponding K_c values that encounter the upper wavenumber noise limit of strain and would produce contaminated strain variance integrals. b) histogram of equivalent E_{shear} values showing distribution and range of E_{shear} values sampled.

with a GM shear variance of $0.661N^2$. The black curves show the mean value of strain variance associated with an E_{shear} bin and the standard error computed as $\sigma/\sqrt{n}$. There is a significant discrepancy between the mean state of our observations and the strain behavior needed to maintain $R_\omega = 3$. Instead of a constant level of strain variance, we find a significant trend showing increasing strain variance as E_{shear} decreases. At an E_{shear}=1 level we find twice the strain variance needed for $R_\omega = 3$. As E_{shear} increases, however, we find that the behavior of strain converges towards $R_\omega = 3$. Unfortunately, we have less data at these high E_{shear} levels so the confidence in this high E_{shear} behavior is reduced compared to E_{shear} <5.

As the level of $\phi_{V_z}(k_z)$ decreases, k_c increases (3.7). In order for the strain variance to remain constant, the strain spectral level needs to go down at the same rate as shear. Since our observations show an increasing level of strain variance when integrating strain out to k_c, this indicates that the strain spectra is not changing its level as rapidly as shear.

Visual examination of the strain spectra corresponding to low E_{shear} levels from our data reveals that, indeed, the strain spectral level does change slower than shear for all E_{shear} levels < 5. From average shear and strain spectra for each E_{shear} value, we can calculate the rates of change from $E_{shear} = 1$ to $E_{shear} = 5$ and from $E_{shear} = 5$ to $E_{shear} = 10$ (Fig. 3.15).

As E_{shear} increase from 1 to 5, we expect a 5 times increase in spectral level. Our observations of shear are consistent with this expectation showing an increase of 4.9 times over this E_{shear} range. Strain, however, only increases by 2 times. As E_{shear} increases from 5 to 10, we expect a 2 times increase in level. Mean spectra show an increase in shear level of 2.8 times with strain increasing by 1.5 times. This confirms that for E_{shear} values less than 5, the strain level does not vary at the same rate as shear and is 3 times slower. For $E_{shear} > 5$, shear and strain spectral levels increase at much closer to the same rate, as is needed to maintain a constant R_ω.

Since strain spectral levels remain relatively constant at low energy levels when compared to the rate of increase needed to maintain $R_\omega = 3$ we attempt to replicate this behavior by assigning a constant GM strain spectral level for all E_{shear} values less than 5. We find that a GM76 $E_{shear} = 9$ or a GK91 $E_{shear} = 7$ spectrum produce similar values at $E_{shear} = 1$ and $E_{shear} = 5$ when compared to observations, but fails to asymptote to a strain variance of 0.221. Here GM76 refers to the standard GM model [Garrett and Munk, 1975] using the parameters from Cairns and Williams [1976] while GK91 refers to the version of the GM model that makes use of the parameters from Gregg and Kunze [1991].

Potential explanations

A potential explanation for this behavior is high wavenumber noise contamination. As $k_c$increases, our strain integration may encounter the instrument noise floor resulting in a

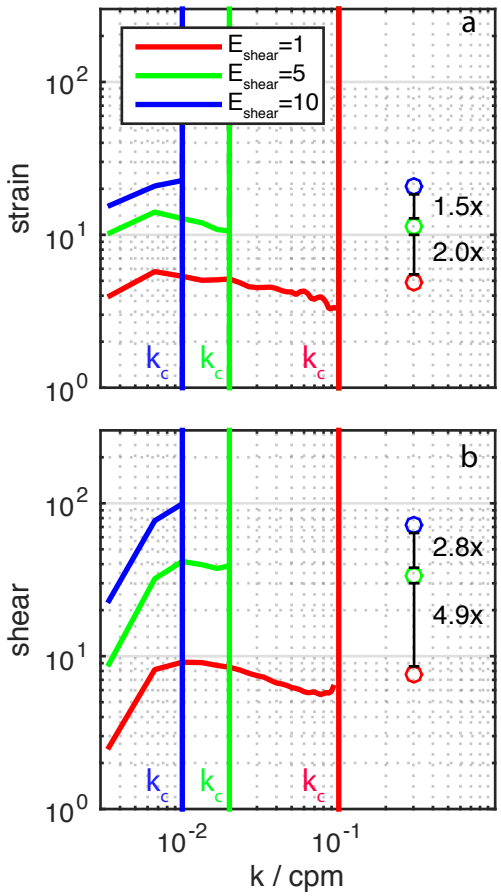

Figure 3.15: Shear (b) and strain (a) spectra associated with E_{shear}. Mean shear and strain spectra are shown for $E_{shear} = 1, 5, 10$. The GM spectrum, in order to maintain a $R_\omega = 3$ at all E_{shear} levels, requires that shear and strain spectra elevate at the same rate. Moving from $E_{shear} = 1$ to $E_{shear} = 5$ requires a five times increase in mean shear level. Panel b shows in shear we have a 5x increase in mean shear level from $E_{shear} = 1$ to $E_{shear} = 5$. However, in strain we see only a 2x increase in strain level. From $E_{shear} = 5$ to $E_{shear} = 10$ we need to see an associated 2x increase in levels. Shear level shows an increase of 2.8x and strain shows an increase of 1.5x. From $E_{shear} = 1$ to $E_{shear} = 5$ shear level increases slower than is predicted by the GM model while for values $E_{shear} > 5$ we see levels increasing very close to the rate anticipated by GM. Vertical colored lines indicate the appropriate k_c for each E_{shear} level.

contaminated integral. However, careful analysis of all of the low E_{shear} strain spectra, and associated k_c values, shows that noise floor contamination is not an issue at E_{shear} levels

greater than 0.75 (as can be seen from the shape of the lowest E_{shear} binned spectrum in Fig.3.15). We mark this region as the shaded red patch on figure 3.14 and do not consider this contaminated region in our analysis.

Additionally, assuming that a noise saturated density spectrum is completely white and has a level relatively independent of E_{shear}, as observed, we can compute the resulting strain variance as a function of E_{shear}. The spectral variance from the white noise spectrum (blue crosses in Fig. 3.14a) increases far too rapidly as E_{shear} approaches 1 from higher values. This indicates that the observed structure in strain requires a spectral shape with a high wavenumber roll off to simulate our results and cannot be represented as a white density spectrum.

While it is possible that a high wavenumber roll off could be produced from a noise spectrum that has been acted upon by a filter, we have attempted to correct for the wavenumber response of all processing operations that we understand. Also, the high wavenumber behavior does not appear as a function of a response to a filtering operation because the slope is nearly constant.

Implication and discussion

Our sites represent highly energetic often strongly tidally driven and/or wind driven regimes that may act not as the background state but as the sources of energy for the rest of the system. Our results demonstrate that the mean state of these regimes differs greatly but predictably from the state predicted by a model with a constant R_ω. This has potentially significant implications. Initially, it draws into question the universality by which the finescale parameterizations should be applied. It also indicates that it may be necessary to reformulate the structure of the reference spectrum, and how the spectra vary in relation to each other, in energetic regimes. In particular, it seems as though additional empirical corrections may be needed to convert the finescale parameterization from shear based to strain based.

3.7 Conclusions

We have presented data from five field programs and 14 moorings spread across a variety of regions in an attempt to characterize and understand variability in the shear to strain ratio and the impact of this variability on our ability to estimate diffusivity via finescale parameterizations.

Variations in R_ω have been shown to occur on a variety of temporal and spatial scales. The magnitude of these variations, at a single location, is significant enough to introduce changes in estimates of parameterized diffusivity that cover an order of magnitude. The structure of the variability in R_ω has been shown to have strong correlations with near inertial shear and tidal strain. Near-inertial energy, presumably wind driven, produces large mixing events, and changes in diffusivity, that are not well represented strain. This has strong implications about the potential for both seasonal and general fair weather bias in direct shipboard measurements of diffusivity as the weather patterns causing these events are not conducive to ship based finestructure measurements. It is very possible that short field programs with direct or inferred diffusivity measurements may only capture one state of a dynamic system.

Systematic changes in R_ω, E_{shear}, and E_{strain} have been observed in the vertical. We conclude that the vertical structure of R_ω has strong ties to topographic interactions because sites near large topographic features, where R_ω tends to decrease in depth, show a coincident increase in E_{strain}. Generally, decreases in R_ω as a function of depth are not caused by a reduction in E_{shear}. In contrast, shear driven sites in the upper water column, and away from topographic features, often exhibit an increase in R_ω with depth resulting from an increase in E_{shear}. These two paradigms were highlighted at the Mendocino mooring where the lower MP shows an increase in R_ω as a function of depth but the upper MP shows the opposite.

Our attempts to model R_ω as a function of other parameters have shown that each site has an optimal variable (shear or strain) by which R_ω can be predicted. These predictions yield significant improvements in terms of root mean square deviation relative to the full

time varying R_ω when compared to the error from assuming a constant of $R_\omega = 3$.

Wavenumber profiles of correlation coefficient revealed that the strongest correlations between R_ω and shear or strain generally occur at only a narrow band of wavenumbers and at a specific frequency. R_ω is not responding to a uniform heaving of the internal wave spectrum, as predicted by the GM model, but to specific forcing events occupying a limited region of the wavenumber frequency space.

We find that at E_{shear} levels less than 5, the level of strain variance does not change as rapidly as shear. This is in direct contrast to a GM model that has shear and strain spectral levels covarying for all E_{shear} levels, as described by Gargett [1990], to maintain $R_\omega = 3$. To fit our observations, the strain spectrum requires a very GM like shape, with a low and high wavenumber roll off. If this effect were to simply be the result of instrument noise, or resolution limits, we would not expect it to require such a shape.

It is a challenge to parameterize diffusivity without full knowledge of the shear and strain fields because assuming a value for R_ω incorrectly can introduce significant error. Even with a characterization of the wave field, predicting an instantaneous value of R_ω is difficult because features, e.g. tides and atmospheric forcing, that strongly influence R_ω are temporally variable.

It is our hope that the work presented herein has highlighted the importance of having accurate values of R_ω for use in finescale diffusivity parameterizations and shown that the scale of error introduced by incorrectly assuming R_ω can potentially explain all of the disagreement between previous estimates and microstructure. In order to fully understand the way in which oceanic variability is tied R_ω, more data is required such that improved statistics can be generated about a wider range of regimes.

3.8 Acknowledgments

The author would like to acknowledge all of the people who were pivotal in shipboard operations and/or the design and deployment of the instrumentation used in each of the field programs. Additionally, we are indebted to the captain, crew, and marine technicians of the

R/V Wecoma, the R/V Melville, and the R/V Revelle. Useful comments were provided by Byron Kilbourne, John Guthrie, and Brian Rasmussen. This research was funded by NSF grant OCE-1129565.

3.9 Bibliography

Matthew H Alford. Sustained, full-water-column observations of internal waves and mixing near Mendocino Escarpment. *J. Phys. Oceanogr.*, 40(12):2643–2660, 2010. doi: 10.1175/2010JPO4502.1.

Matthew H Alford, Jennifer A MacKinnon, Zhongxiang Zhao, Robert Pinkel, Jody Klymak, and Thomas Peacock. Internal waves across the Pacific. *Geophys. Res. Lett.*, 34(L24601): doi:10.1029/2007GL031566, 2007.

J. L. Cairns and G. O. Williams. Internal wave observations from a midwater float, 2. *J. Geophys. Res.*, 81:1943–1950, 1976.

Brian Chinn, Matthew H Alford, and James B Girton. Observations of internal waves and parametric subharmonic instability in the Philippines archipelago. *J. Geophys. Res.*, 117 (C05019):1–12, 2012. doi: doi:10.1029/2011JC007392.

G D Egbert and R D Ray. Significant dissipation of tidal energy in the deep ocean inferred from satellite altimeter data. *Nature*, 405(6):775–778, june 2000.

B H Ferron, H Mercier, K Speer, A Gargett, and K Polzin. Mixing in the Romanche Fracture Zone. *J. Phys. Oceanogr.*, 28:1929–1945, 1998.

Ann E. Gargett. Do we really know how to scale the turbulent kinetic energy dissipation rate ϵ due to breaking of oceanic internal waves? *J. Geophys. Res.*, 95(C9):15971–15974, 1990.

C. J. R. Garrett and W. H. Munk. Space-time scales of internal waves: A progress report. *J. Geophys. Res.*, 80(3):291–297, january 1975.

James B Girton, Brian Chinn, and Matthew H Alford. Internal Wave Climates of the Philippine Seas. *Oceanography*, 24(1):100–111, 2011.

M. C. Gregg and E. Kunze. Shear and Strain in Santa Monica Basin. *J. Geophys. Res.*, 96 (C9):16709–16719, 1991.

M.C. Gregg. Scaling turbulent dissipation in the thermocline. *J. Geophys. Res.*, 94(C7): 9686–9698, july 1989.

M.C. Gregg and T.B. Sanford. Signatures of mixing from the Bermuda Slope, the Sargasso Sea and the Gulf Stream. *J. Phys. Oceanogr.*, 10(1):105–127, january 1980.

Michael C. Gregg, Thomas B. Sanford, and David P. Winkel. Reduced mixing from the breaking of internal waves in equatorial waters. *Nature*, 422:513–515, April 2003.

Rob A Hall, Matthew H Alford, Glenn S Carter, Michael C Gregg, Ren-Chieh Lien, Danielle J Wain, and Zhongxiang Zhao. Transition from partly standing to progressive internal tides in Monterey Submarine Canyon. *Deep-Sea Res II*, 104:164–173, 2013.

M. J. Harrison and R. W. Hallberg. Pacific subtropical cell response to reduced equatorial dissipation. *Journal of Physical Oceanography*, 38(9):1894–1912, 2014/07/09 2008.

F. S. Henyey, J. Wright, and S. M. Flatté. Energy and action flow through the internal wave field. *J. Geophys. Res.*, 91(C7):8487–8495, July 1986.

S R Jayne. The impact of abyssal mixing parameterizations in an ocean general circulation model. *J. Phys. Oceanogr.*, 39:1756—1775, 2009.

Sam Kelly and Jonathan D Nash. Internal-tide generation and destruction by shoaling internal tides. *Geophys. Res. Lett.*, 37(L23611):1–5, 2010. doi: doi:10.1029/2010GL045598.

Sam Kelly, Jonathan D Nash, Matthew H Alford, and Kim I Martini. The cascade of tidal energy from low to high modes on a continental slope. *J. Phys. Oceanogr.*, 42(7):1217–1232, 2012.

Eric Kunze, Eric Firing, Jules Hummon, Teresa K Chereskin, and Andreas Thurnherr. Global abyssal mixing inferred from lowered ADCP shear and CTD strain profiles. *Journal of Physical Oceanography*, 36(8):1553–1576, 2006.

J. A. MacKinnon, Matthew H. Alford, O. Sun, R. Pinkel, Zhongxiang Zhao, and Jody Klymak. Parametric Subharmonic Instability of the internal tide at 29N. *J. Phys. Oceanogr.*, 43(1):17–28, 2013a.

Jennifer A. MacKinnon, Matthew H. Alford, Rob Pinkel, Jody Klymak, and Zhongxiang Zhao. The latitudinal dependence of shear and mixing in the Pacific transiting the critical latitude for PSI. *J. Phys. Oceanogr.*, 43(1):3–16, 2013b.

K I Martini, Matthew H Alford, Sam Kelly, and Jonathan D Nash. Observations of internal tides on the Oregon Continental Slope. *J. Phys. Oceanogr.*, 41(9):1772–1794, 2011.

C. Henry McComas and Peter Müller. Time scales of resonant interaction among oceanic internal waves. *J. Phys. Oceanogr.*, 11:139–147, 1981.

Angelique Melet, Robert Hallberg, Sonya Legg, and Kurt L Polzin. Sensitivity of the ocean state to the vertical distribution of internal-tide-driven mixing. *J. Phys. Oceanogr.*, 43(3): 602–615, 2013. doi: http://dx.doi.org/10.1175/JPO-D-12-055.1.

W. Munk and C. Wunsch. Abyssal recipes II: energetics of tidal and wind mixing. *Deep-Sea Res. Part I*, 45:1977–2010, 1998.

J D Nash, Matthew H Alford, Eric Kunze, Kim I Martini, and Sam Kelly. Hotspots of deep ocean mixing on the Oregon continental slope. *Geophys. Res. Lett.*, 34(L01605): doi:10.1029/2006GL028170, 2007.

T. R. Osborn. Estimates of the local rate of vertical diffusion from dissipation measurements. *J. Phys. Oceanogr.*, 10:83–89, 1980.

J. J. Osborne, A. L. Kurapov, G. D. Egbert, and P. M. Kosro. Spatial and temporal variability of the m2 internal tide generation and propagation on the oregon shelf. *J. Phys. Oceanogr.*, 41(11):2037–2062, 2011/12/13 2011. doi: 10.1175/JPO-D-11-02.1. URL `http://dx.doi.org/10.1175/JPO-D-11-02.1`.

Andrew Pickering, Matthew H Alford, Zhongxiang Zhao, Jennifer A MacKinnon, Rob Pinkel, and Jody M Klymak. Near-Inertial Waves During the Internal Waves Across the Pacific Experiment. in prep.

K. L. Polzin, J. M. Toole, J. R. Ledwell, and R. W. Schmitt. Spatial variability of turbulent mixing in the abyssal ocean. *Science*, 276:93–96, 1997.

Kurt L. Polzin, John M. Toole, and Raymond W. Schmitt. Finescale parameterizations of turbulent dissipation. *J. Phys. Oceanogr.*, 25:306–328, 1995.

R M Samelson. Large scale circulation with locally enhanced vertical mixing. *J. Phys. Oceanogr.*, 28(4):712–726, 1998.

Z. D. Tessler, A. L. Gordon, L. J. Pratt, and J. Sprintall. Transport and dynamics of the Panay Sill overflow in the Philippine Seas. *J. Phys. Oceanogr.*, 40:2679–2695, 2010. ISSN 1520-0485.

S.A. Thorpe. Turbulence and mixing in a Scottish Loch. *Philos. Trans. R. Soc. London Ser. A*, 286:125–181, 1977.

D J Wain, M C Gregg, Matthew H Alford, R C Lien, G S Carter, and R A Hall. Propagation and dissipation of the internal tide in upper Monterey Canyon. *J. Geophys. Res.*, 118: 4855–4877, 2013.

Caitlin B Whalen, Lynne D Talley, and Jennifer A MacKinnon. Spatial and temporal variability of global ocean mixing inferred from argo profiles. *Geophys. Res. Lett.*, 39(L18612): doi:10.1029/2012GL053196, 2012.

Caitlin B. Whalen, Jennifer A. MacKinnon, Lynne D. Talley, and Amy F. Waterhouse. Estimating the mean diapycnal mixing using a finescale strain parameterization. *Journal of Physical Oceanography*, 45(4):1174–1188, 2015/05/13 2015. doi: 10.1175/JPO-D-14-0167.1. URL `http://dx.doi.org/10.1175/JPO-D-14-0167.1`.

Lixin Wu, Zhao Jing, Steve Riser, and Martin Visbeck. Seasonal and spatial variations of southern ocean diapycnal mixing from argo profiling floats. *Nature Geosci.*, 4:363–366, 2011.

Zhongxiang Zhao, Matthew H. Alford, Jennifer A. MacKinnon, and Rob Pinkel. Long-range propagation of the semidiurnal internal tide from the Hawaiian Ridge. *J. Phys. Oceanogr.*, 40(4):713–736, 2010. doi: 10.1175/2009JPO4207.1.

Zhongxiang Zhao, Matthew H. Alford, Ren-Chieh Lien, Michael C. Gregg, and Glenn S. Carter. Internal tides and mixing in a submarine canyon with time-varying stratification. *J. Phys. Oceanogr.*, 42:2121–2142, 2012. doi: 10.1175/JPO-D-12-045.1.

Table 3.1: Experiment name, mooring ID, location, depth, sampling depth, duration, and time mean R_ω and error from each of the MPs aggregated in this analysis. R_ω deviations from 3 affect diffusivity by a factor of h1 (3.3) or h2 (3.11) in the shear–based and strain–based parameterizations, respectively

Experiment	Mooring	Lat (°N)	Lon (°E)	Depth (m)	Sampled range(m)	Duration (days)	mean(R_ω)
IWAP	MP1	25.5	194.9	4874	100-1400	41	3.6±.9
	MP3	28.9	196.5	5359	100-1400	50	4.6±1.2
	MP6	37.1	200.8	5810	100-1400	44	10.4±1.8
Oregon Slope 05	MP1	43.2	-120.26	2995	70-2000	40	8.4±2.6
	MP3	43.2	-125.20	1780	200-1700	30	10.3±2.3
	MP4	43.2	-125.1	1452	50-1430	43	2.4±.65
	MP5	43.2	-125.0	1077	60-1050	43	6.4±1.3
	MP6	43.2	-124.90	500	70-480	22	3.2±.95
Mendocino 09	MP1 U	40.32	-126.06	3700	1000-2150	66	3.0±.6
	MP1 L	40.32	-126.06	3700	2200-3600	66	3.3±.7
Mindoro Strait	MP1 U	12.83	120.6	1850	100-930	72	3.18±.6
	MP1 L	12.83	120.6	1850	950-1800	72	2.0±.34
	MP2	10.35	121.733	1535	80-1430	57	2.6±.45
Monterey	MP1	36.78	-121.92	489	50-470	10	1.5±.66
	MP2	36.78	-121.90	363.5	50 - 350	56	.85±.11
	MP3	36.79	-121.87	287	50-270	56	.81± .13

Table 3.2: Root mean square deviations of observed R_ω from both linear fits and a constant $R_\omega = 3$. Categorized by experiment name, mooring ID, local shear, local strain, $R_\omega = 3$

Experiment	Mooring	local shear	local strain	$R_\omega = 3$
IWAP	MP1	1.5	1.9	2.2
	MP3	1.9	2.1	3.2
	MP6	5.5	6.4	10.8
Oregon Slope 05	MP1	5.2	5.8	9.0
	MP3	10.6	11.5	15.1
	MP4	1.1	1.0	1.3
	MP5	4.2	4.8	6.6
	MP6	3.8	3.9	4.3
Mendocino 09	MP1 U	1.4	1.9	1.9
	MP1 L	2.8	2.8	3.0
Philex	MP1 U	1.6	1.7	2.0
	MP1 L	1.3	1.4	1.5
	MP2	4.1	3.8	4.4
Monterey	MP1	0.9	0 .8	1.6
	MP2	2.0	1.1	2.3
	MP3	5.7	3.9	5.7

3.10 Appendix

3.10.1 IWAP

The Internal Waves Across the Pacific (IWAP) experiment was comprised of ship based spatial transects from a Hydrographic Sonar System (HDSS) and 6 MP moorings set in a line moving north from the Hawaiian ridge that spanned $\approx$ 1400 km. The goal of the experiment was to determine the fate of the internal tide beam emanating from near French Frigate Shoals, Hawaii, as it moved past the critical latitude and continued north. Analysis of the internal tide signals are reported in Alford et al. [2007], Zhao et al. [2010], MacKinnon et al. [2013a], MacKinnon et al. [2013b]. Later analysis also made use of these data to quantify the variability in the near inertial wave field at these locations. Results from this work are documented in Pickering et al. [in prep.]

3.10.2 ORE05

The goal of the Oregon 2005 experiment was to determine whether remote or local processes lead to the turbulent energy dissipation that had been found over the Oregon slope. The experiment was comprised of a 40 day field program and 6 MP moorings. Results are discussed in Kelly et al. [2012], Martini et al. [2011], Nash et al. [2007]

3.10.3 MENDO

The Mendocino 2010 experiment was designed to study the relative strength of near inertial waves and Internal tides to the north of Mendocino escarpment. A single mooring with two MPs was deployed in this region of strong internal tides to establish a base line on the relative contributions of near inertial waves. Results are reported in Alford [2010].

3.10.4 PHILEX

The Office of Naval Research Philippines Straits Dynamics Experiment (Philex) was partially tasked with exploring the contribution of small-scale oceanic processes, including internal

waves, to turbulence and mixing. Results are reported in Chinn et al. [2012], Tessler et al. [2010], Girton et al. [2011].

3.10.5 MC09

The Monterey Canyon 2009 experiment was designed to investigate the horizontal and depth distribution of dissipation in Monterey submarine canyon. Canyons can focus internal waves and can potentially produce globally significant levels of turbulent mixing. Results are reported in Zhao et al. [2012], Wain et al. [2013], Hall et al. [2013]

Chapter 4

THE NATURE AND SHAPE OF THE WAVENUMBER FREQUENCY SPECTRUM

4.1 Introduction

The internal wave continuum is thought of as the spectral pathway through which energy input at narrow band frequencies, inertial, diurnal, semidiurnal, flows to smaller scales and eventual dissipation. The shape of this spectrum has been studied by many, and is frequently compared to a simple model spectrum (GM76) developed by Garrett and Munk [1972] as modified by Cairns and Williams [1976]. This model makes use of several assumptions to facilitate a "convenient representation" of the spectrum. Since, as noted by Garrett and Munk [1972], a truly separated form is incompatible with the MV coherence, the GM76 model assumes that the shape of the spectrum is invariant with respect to frequency, but allow for a scale factor. The validity of this assumption, however, appears less than universal.

Ideally, we would describe the oceanic internal wave field in a four dimensional spectral space spanning all three physical dimensions and time. Unfortunately, from contemporary measurement platforms, such sampling is unattainable and choices must be made about which dimensions to measure in. We focus on two of the four dimensions, specifically vertical wavenumber and frequency. A variety of measurement platforms exist which make different choices about dimensions to sample in, ranging from Lagrangian floats, such as EM–APEX floats and ARGO floats, which move with the fluid and record properties as a function of time and depth following a fluid parcel, to Eulerian platforms such as point current profiler equipped moorings which sample in time but at a fixed set of depths and in a single location. In the following work, we focus specifically on data from McLane Moored profilers (MP). Because the MP samples at high resolution in both time and depth simultaneously, we

can decompose patterns of variability into variance density as a function of both vertical wavenumber and frequency. This allows us to diagnose the wavenumber structure of each frequency independently without having to assume a single unified form as was done in GM76.

Being able to distinguish the wavenumber and frequency structure of strain and shear is important as these properties are often used as quantities from which turbulent dissipation of kinetic energy / vertical diffusivity are estimated (Kunze et al. 2006; Whalen et al. 2012). If the distribution of variance density with frequency is unknown, as in the case of profiling ARGO floats, all frequencies of shear and strain variance will be attributed to internal waves. Previous studies have shown that the vortical mode (zero frequency) component of strain is potentially significant and attributing this variance to internal waves could bias parameterized estimates of vertical diffusivity high.

Previous works have examined the wavenumber frequency spectrum of both shear and strain, unfortunately, the data used in these studies typically cover only a relatively short period of time and only a single location. This makes drawing general conclusions difficult. The moored profiler archive presents a unique opportunity to examine the two dimensional spectrum of velocity and strain over a wide range of forcing parameters and look for factors that influence and control changes in the spectral shape.

This chapter characterizes the two dimensional spectrum of shear and strain at various locations and establishes a framework by which the inherent variability can be reduced to a finite number of scalar parameters. Variability within the set of data are then related to various properties of the locations in order to deduce how different properties of the deployment site impact different regions of the spectrum. Additionally, we evaluate the assumption of separability by computing ideal separable estimates of the two dimensional spectral field and evaluate the variance preserved in this estimate and how the distribution of variance differs from the observations.

4.2 Data

This study makes use of the same MMP archive that was discussed in Chapter 3. Deployment parameters for each MP are listed in table 3.1 and Figure 3.1 shows the location of each mooring on a global map. The spectral resolution and bandwidth of our two dimensional spectra are controlled by the deployment parameters and the choices made in gridding the data. The resultant data are typically gridded to a 2 meter vertical resolution and 1.5 hour time interval that produces a Nyquist wavenumber and frequency of $k_z = .25$ cpm and $\omega = 8$ cpd.

We choose the largest time and depth aperture possible while avoiding the mixed layer. The minimum time aperture used ranges from 10 days with a maximum of ≈ 60 days and the vertical aperture ranges from 200 to 1000m. Cyclic resolution is given by the inverse of the record length in days or meters.

4.3 Methods

4.3.1 Two dimensional spectrum

The distribution of velocity and strain variance in vertical wavenumber and frequency space is examined by computing the two dimensional power spectrum of complex velocity $(u + iv)$ and strain (ζ). We calculate the power spectrum by taking the two dimensional fast Fourier transform of each field.

$$\hat{F} = fft(F) \tag{4.1}$$

The Fourier components are then squared and normalized by the wavenumber resolution and the frequency resolution such that Parseval's theorem is upheld and the integral of the power spectrum is the variance.

$$\hat{\Phi}(k, \omega) = \hat{F}\hat{F}^*/(\delta k \delta \omega) \tag{4.2}$$

This produces a two dimensional spectral estimate of variance density with resolution in frequency and wavenumber given by the size of aperture ($\delta\omega$ or $\delta k = 1/$aperture width) and the nyquist frequencies of $\omega_{ny} = \frac{1}{2\delta\omega}$ and $k_{ny} = \frac{1}{2\delta k}$.

From $\hat{\Phi}(k,\omega)$ we can compute the total vertical wavenumber spectrum and the frequency spectrum as the integrals over the other dimension. EG

$$\hat{\Phi}(\omega) = \int_{k_0}^{k_n} \Phi(k,\omega)dk \tag{4.3}$$

$$\hat{\Phi}(k) = \int_{\omega_0}^{\omega_n} \Phi(k,\omega)d\omega \tag{4.4}$$

In this paper we also compute average spectra in a frequency/wavenumber band by, instead of integrating over all frequencies or wavenumbers, averaging over a range of frequencies or wavenumbers. For example, the average wavenumber spectrum near the frequency ω_i with a frequency bandwidth of $[\omega_i - 0.1 \ : \ \omega_i + 0.1]$ cpd would be computed as.

$$\hat{\Phi}(k)_{\omega_i} = \frac{1}{(\omega_i - 0.1) - (\omega_i + 0.1)} \int_{\omega_i - 0.1}^{\omega_i + 0.1} \Phi(k,\omega)d\omega \tag{4.5}$$

Though these computations are similar the normalization is different.

4.3.2 Evaluation of separability

The GM model relies upon several assumptions. One of these assumptions is that the spectrum is separable, or that the vertical wavenumber structure of the spectrum does not change with frequency and vice versa. With the broad range of regimes represented by the data used here, it is possible to evaluate the degree to which the spectrum can be separated under various forcing and topographic areas. To quantify the level of separability, and to examine where deviations from separability occur, we use the singular value decomposition (SVD) to create an optimal separable representation of the spectrum. First, the total spectrum is computed by summing the four quadrant two dimensional spectrum so that all variance is in a single quadrant. We then calculate the SVD of this total spectrum.

A best k-rank approximation,$\hat{A}_k$, of A is given by zeroing out the r-k ($r \equiv$ rank(A)) trailing singular values of A or

$$\hat{A}_k = U\hat{S}_k V^T \tag{4.6}$$

$$\hat{S}_k = diag(\sigma_1, ..., \sigma_k, 0, ...0) \tag{4.7}$$

This minimizes the Euclidean norm

$$||A - \hat{A}_k||_f = \sqrt{\sigma_{k+1}^2 + ... + \sigma_r^2}. \tag{4.8}$$

Since the singular values are proportional to the variance explained by each pair of vector forms, minimizing the sum of the $[k+1 : r]$ singular values means that the form defined by the k singular value and vectors is the rank k form that has as much variance as can be explained by a rank k representation of the observations. In our case we take $k = 1$ since we want a rank 1(separable) approximation of the 2d spectrum and call this representation the optimal separable representation. In other words, what the above does is to find the separable representation of the spectrum that is as close to the observation as possible.

4.4 Results

4.4.1 Separable spectrum

To evaluate the separability of the internal wave spectrum, optimal spectra were computed from both velocity and strain for each of the MPs following the methods described in section 4.3.2. Despite the broad range of forcing regimes captured by this set of moorings, they exhibit some remarkably similar patterns. In order to highlight these patterns we present a detailed analysis of the IWAP MP1 mooring and comment on the features that are common to the entire set of moorings while the remaining total two dimensional spectra for each mooring are included in appendix 4.9 as a reference for comparison.

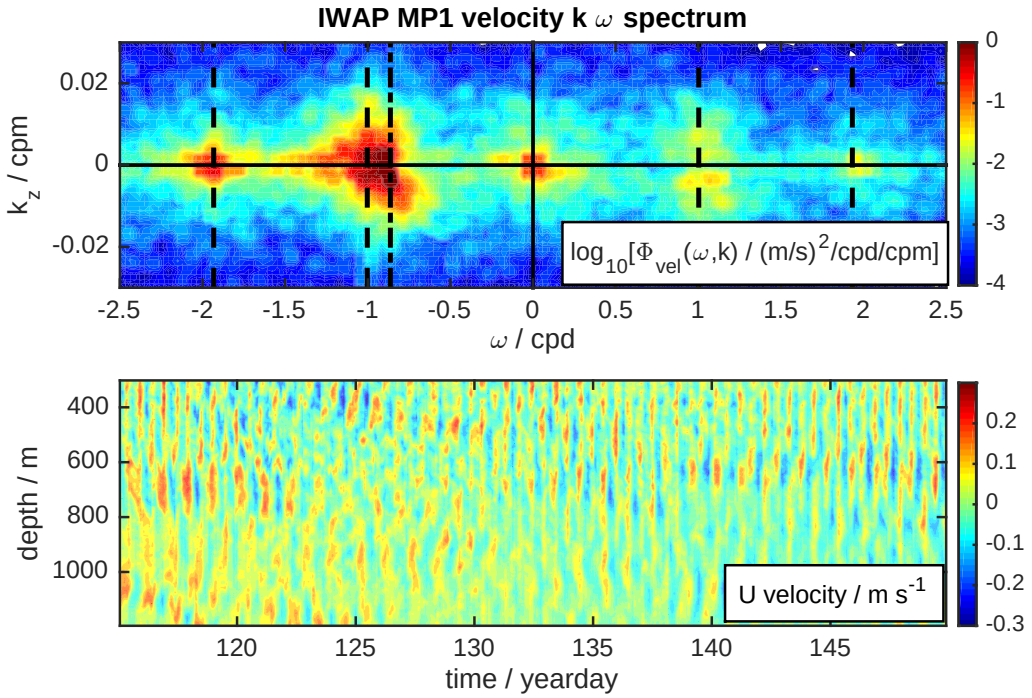

Figure 4.1: IWAP MP1 wavenumber frequency spectrum of velocity and time depth map of U velocity used to form the complex velocity $u + iv$ used to compute the two dimensional spectrum.

At IWAP MP1, the aperture over which the two dimensional spectrum is calculated spans 300 to 1200 m in depth and from year day 115 to 150. The time depth map of U velocity corresponding to this aperture is shown in figure 4.1. Following the steps in section 4.3.1 we compute a wavenumber frequency power spectrum of velocity for this aperture (Fig. 4.1).

The IWAP MP1 mooring was located at 25.48°N and the inertial frequency at this latitude is 0.8630 cpd. In the two dimensional spectrum we see strong components of energy at the 0 cpd, inertial, diurnal, and semidiurnal frequencies. The inertial, diurnal, and semidiurnal bands show an asymmetric distribution with frequency with more variance in the negative frequency components as we expect for internal waves in the northern hemisphere. All frequencies show an even distribution of variance between positive and negative wavenumbers with the exception of the inertial band which appears to have a more variance at nega-

tive wavenumbers that we would associate with downward propagating waves [Leaman and Sanford, 1975].

To evaluate overall level of separability, we compute the total two dimensional spectrum by summing all four quadrants of the velocity spectrum for IWAP MP1 (Fig. 4.2) and focus only on frequencies that are greater than the local inertial.

The most prominent features in the record are strong peaks at the diurnal and semidiurnal frequency (though at this latitude cleanly separating the diurnal from the inertial is not possible). These peaks appear as large amplitude narrow band frequency spikes in variance density that decay rapidly as a function of wavenumber. By approximately $k = 0.02$ cpm, these narrow band peaks have nearly returned to the values of the "background continuum". In this analysis, the "background continuum" is considered to be the regions of frequency space that do not contain diurnal, semidiurnal, inertial, and vortical frequencies. The spectrum at $k > 0.02$ cpm appears nearly uniform at frequencies of $\omega < 4.5$ cpd. As frequency increases beyond ≈ 4.5 cpd, we see the spectral levels begin to attenuate with frequency.

Frequency band averaged vertical wavenumber spectra of velocity for all of the IWAP moorings illustrate this pattern (Fig. 4.3). All of the frequency bands can be seen collapsing to a nearly uniform wavenumber structure at $k > 10^{-2}$ cpm.

By integrating the two dimensional spectrum as described in section 4.3.2, the optimal wavenumber and frequency functions are computed and shown against the actual wavenumber and frequency spectra of velocity as well as the spectra from the GM model based on the mean stratification and latitude of this mooring (Fig. 4.2). Both the average and optimally separated spectra are very similar to one another and show fair agreement with the GM model aside from the presence of internal tide peaks which are not present in the GM model. The optimal frequency spectrum has levels that are lower than the observed, though the two converge at the inertial frequency. The wavenumber spectra show a more marked divergence. Both the observed and optimal spectrum show similar values at low wavenumbers with peak values exceeding GM. As wavenumber increases, however, the optimal spectrum decreases far more rapidly than the observed (Fig. 4.2).

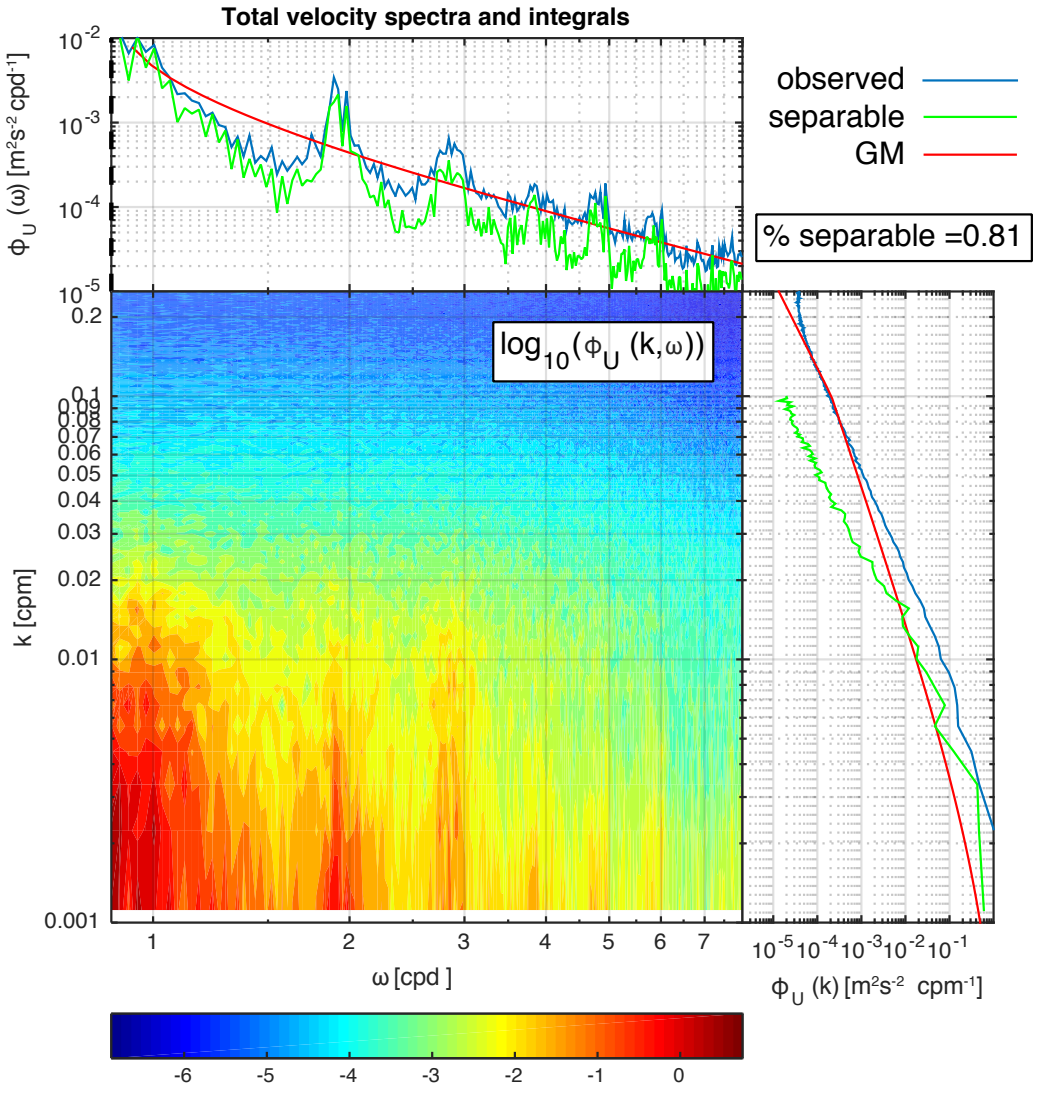

Figure 4.2: IWAP MP1 total wavenumber frequency spectrum of velocity. Sub panels show integrated wavenumber spectrum and frequency spectrum as well as optimal separable representation of the 2d spectrum and GM model results.

If we compute the optimal total two dimensional spectrum as the outer product of the optimal wavenumber function and the optimal frequency function scaled by the largest singular value we can see the effect of constraining wavenumber and frequency to a single shape. The impact of this is highlighted by examination of the observed and optimal two dimensional

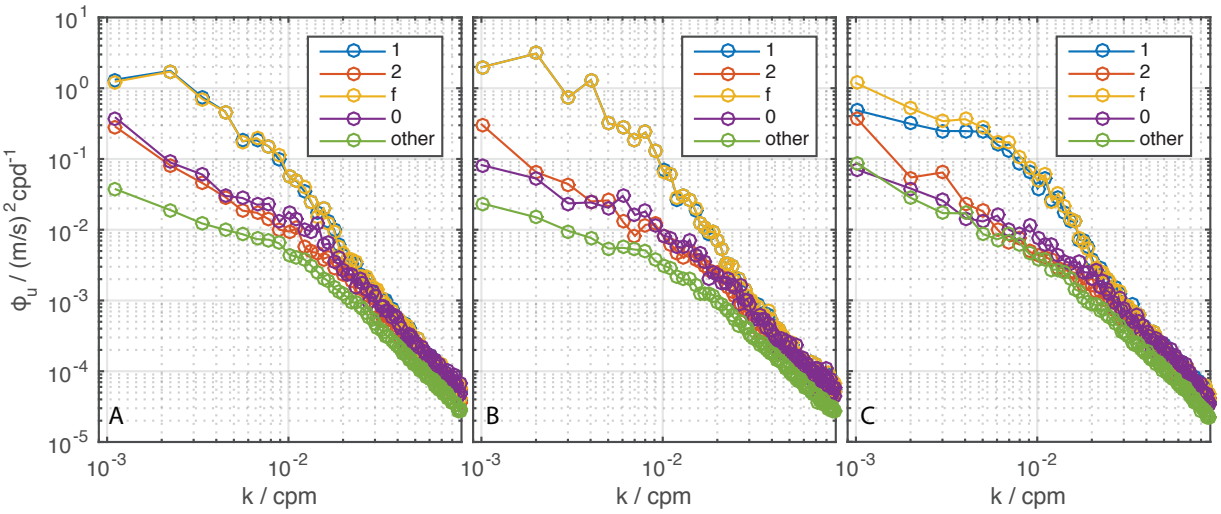

Figure 4.3: Wavenumber spectra of velocity separated by frequency band for IWAP MP1 MP3 MP6. Frequency bands considered are diurnal (1 cpd), semidiurnal (2 cpd), inertial (f), vortical (0 cpd), and other. Other is computed by averaging over all frequencies not within 0.1 cpd of 1,2,f,0 cpd.

spectra of figure 4.4.

While the optimal spectra in figure 4.2 look close to the mean observed spectra, the resultant 2d spectrum from the optimal vectors is quite different than the observed (Fig. 4.4). Because the separable spectrum is constrained to having a single structure in wavenumber, the optimal spectrum cannot match the rate of attenuation in wavenumber for both the background continuum and the narrow band peaks. Because of this, we see tidal peaks, and harmonics, that extend to very high wavenumbers (Fig. 4.4b) while in the observation they are attenuated by $k \approx 10^{-2}$ cpm (Fig. 4.4a). Figure 4.4c shows the two dimensional GM spectrum of velocity given the local stratification and latitude. Comparing the GM spectrum to the optimal spectrum we see some similar patterns in the background. There is a uniform decrease in variance density as both wavenumber and frequency increase given by the sloping iso curves of variance density. However, this is in contrast to the uniform frequency structure at $k > 0.02$ cpm and $\omega < 4.5$ cpd that appears in the observations.

These patterns are similar to observations made in previous studies of the internal wave

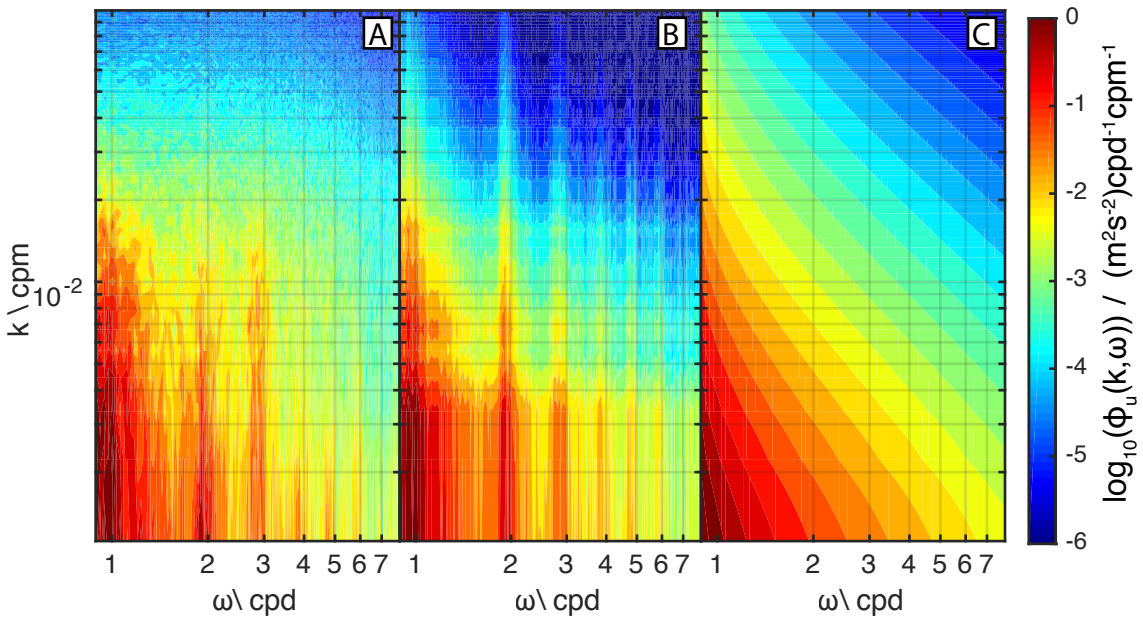

Figure 4.4: a) Total wavenumber and frequency spectrum of velocity b) Optimal separable representation of the two dimensional spectrum c) GM model result

spectrum. From an 18 day record off the coast of California, Pinkel [1984] report a similar high wavenumber cut off at $k = 0.015$ cpm and also a similar change in spectral shape at frequencies greater than 5 cpd. Remarkably, these patterns exist in nearly all of the MP records examined here. Because the same patterns were reported by Pinkel [1984], and since their study made use of an entirely different measurement platform (Doppler sonars mounted on the research platform FLIP), it is unlikely that the commonality of the patterns observed is due to some inherent property of the MP.

4.4.2 Spectral dissection

Our analysis of the separability of the two dimensional spectrum revealed that there appear to be distinct regions in the two dimensional spectrum that have different wavenumber and frequency structure. To investigate the factors that influence the magnitude and structure of variance density in these regimes, average spectra were computed over various frequency

and wavenumber bands. In particular, this work focuses on the narrow band frequency peaks at the vortical (0 cpd), diurnal, and semi diurnal frequencies. In the case of velocity, this includes both negative and positive frequencies and separation between positive and negative wavenumbers is retained. In the case of strain, the symmetry of the two dimensional spectrum of a real quantity means that maintaining all four quadrants of the spectrum is unnecessary.

Velocity wavenumber spectra

Average wavenumber spectra for each frequency band and wavenumber sign are computed over a frequency bandwidth around a frequency, ω, of $[\omega - 0.1; \omega + 0.1]$ cpd. This is a narrow band designed to capture the peak variability in the frequency bands. Average wavenumber spectra at different frequency bands are shown for every MP used in this analysis as well as average spectra of all of the sites (Fig. 4.5).

The spectra exhibit a broad range of variability both between the sites and between the different frequency bands. However, in similar fashion to the IWAP moorings, the spectral shapes tend to converge at wavenumbers greater than $k = 10^{-2}$ cpm. Though they do not have the same value, the shape is nearly the same. This is because, as noted previously, at wavenumbers greater than $k = 10^{-2}$ cpm the narrow tidal peaks have largely decreased and have approached the level of the background continuum. This is particularly clear in Fig. 4.5f where the frequency spectrum from each band, averaged over all of the sites, is shown. Nearly all of the variations in the different frequency bands exists at $k < 10^{-2}$ cpm while at $k > 10^{-2}$ cpm the average spectra from the frequency bands are essentially the same.

Wavenumber spectra associated with the positive diurnal, positive semidiurnal, and vortical frequencies show less asymmetry between positive and negative wavenumber components when compared to the negative frequencies for wavenumbers $k < 10^{-2}$ cpm. This is shown as the distance between the two black mean spectral curves on each panel of figure 4.5. The implication is that in the positive frequency bands there is an equal amount of upward propagating and downward propagating low wavenumber waves while in the negative frequency bands we see an excess of -k implying more downward propagation.

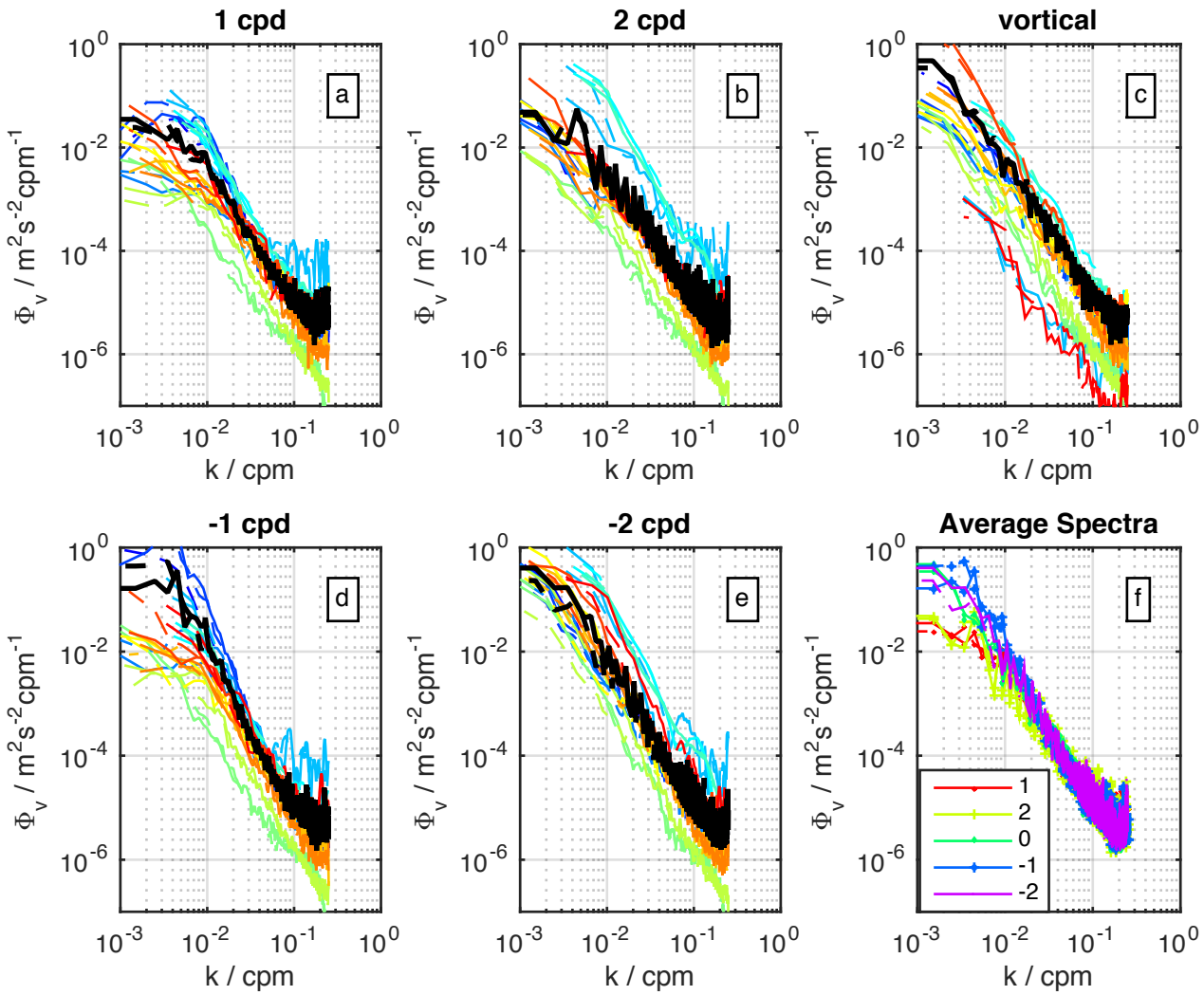

Figure 4.5: Average velocity spectra for all mooring sites separated by positive and negative frequency and vortical mode contributions. Dashed lines correspond to negative wavenumbers and solid lines correspond to positive wavenumbers. In panels a,b,c,d,e each color indicates a different mooring while in panel f colors are used to distinguish between frequency bands.

We can capture the low wavenumber structure, and the $k > 10^{-2}$ cpm, structure of the background continuum by looking at the average spectra that lie outside the bands that we are considering the peaks. We consider here all frequencies that lie outside the bandwidth that we are using in calculating the mean narrow band peak spectra. Though

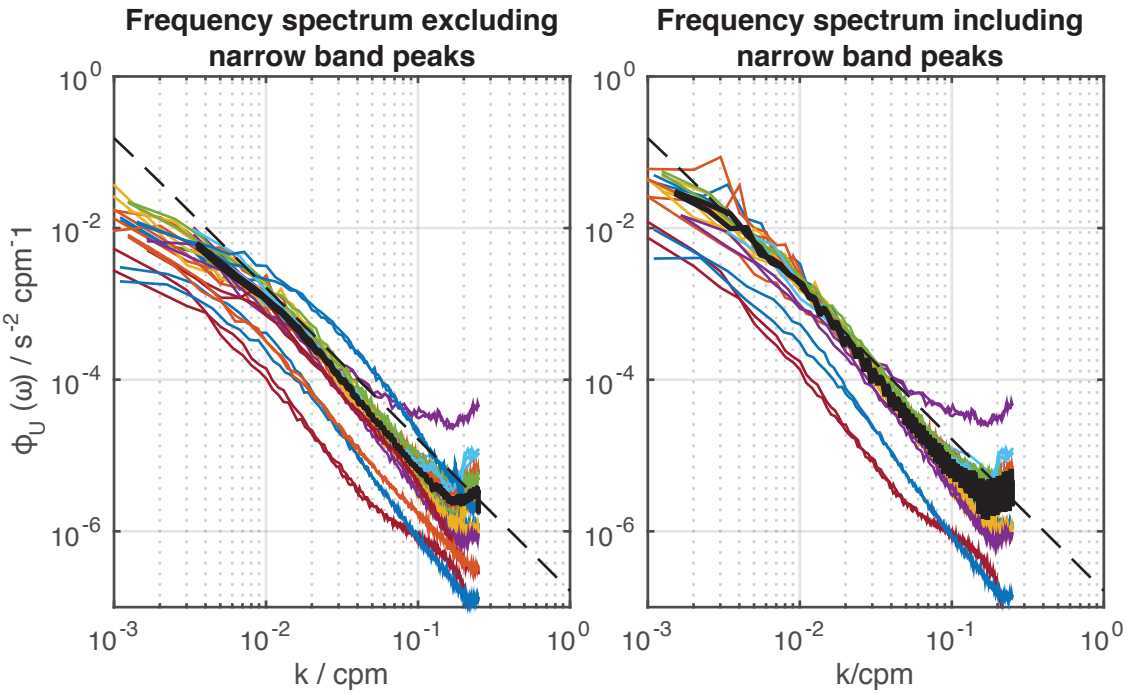

Figure 4.6: a) Average velocity spectra for all mooring sites in frequencies that are not ± 1,2,f as well as average of all spectra. Each color represents a MP. There are two lines per color showing both positive and negative wavenumber components of the background spectrum. The background field at each site is more vertically isotropic than the spectral peaks. The thick black line shows the average of all of the site spectra. The dashed black line shows the shape of the wavenumber spectrum from the GM model. N for the GM model is chose to be a value that makes the level similar to the average spectrum. b) Average velocity spectra for all mooring sites in all frequencies. Each color represents a MP. There are two lines per color showing both positive and negative wavenumber components of the background spectrum. The thick black line shows the average of all of the site spectra. The dashed black line shows the shape of the wavenumber spectrum from the GM model. N for the GM model is chose to be a value that makes the level similar to the average spectrum. The average spectral shape in between the narrow band peaks fails to match the GM model at low wavenumbers from $[10^{-3} : 10^{-2}]$ cpm. Because of the redness of the spectra, this region, despite the small magnitude of wavenumbers, is an important contributor to total variance. Average spectral shape much more closely resembles GM in this region when the narrow band peaks of the tides and vortical mode are included.

this may include elevated levels from the edges of the narrow band peaks, we use all non peak frequencies for completeness and so that uniformity in our analysis with respect to what is

"non peak" is retained. The average background velocity spectrum for each site is shown in Fig. 4.6a. At wavenumbers $k > 10^{-2}$ cpm, as expected, the background spectra show a similar linear form in a log log space to that of the wavenumber structure of the narrow band peaks. However, at $k < 10^{-2}$ cpm, spectral levels deviate from this linear pattern and whiten, reducing the slope by nearly a half. The shape of the GM spectrum is shown along with the average background spectra for all of the moorings as a dashed line and solid black line respectively. The GM curve shown has been scaled so that it agrees with the site wide average spectrum and is simply to illustrate the general shape of the GM model as each site would have a different predicted GM level. The slope of the spectral background levels at $k > 10^{-2}$ cpm is similar to that predicted by GM, while the curvature of the spectra at $k < 10^{-2}$ cpm represents a significant deviation from the GM model. The shape and nature of this whitening of the spectra at low wavenumbers is consistent between the experiments and is a fact we will exploit and examine later in our analysis.

strain spectra

As was done with velocity, we can compute similar site average wavenumber spectra of strain. Strain was computed as $\xi = \frac{N^2}{N^2_{mean}} - 1$ and spectra (Φ_{strain}) were corrected to ($\hat{\Phi}_{strain}$) to account for the response from the first difference operator as

$$\hat{\Phi}_{strain} = \Phi_{strain} \frac{1}{sinc^2(2k)}. \tag{4.9}$$

An example of this correction is shown for IWAP MP1 (Fig. 4.7).

Average strain spectra from the narrow band peaks have a similar wavenumber structure to what was seen in velocity (Fig. 4.8). The majority of the site to site variations in average peak spectra are at wavenumbers $k < 10^{-2}$ cpm. However, unlike shear, because of the symmetry of the spectrum we cannot discern patterns in positive/negative wavenumber content in terms of positive and negative frequency. Instead, we note that on average we see a greater discrepancy between negative and positive wavenumber spectral levels at the semi

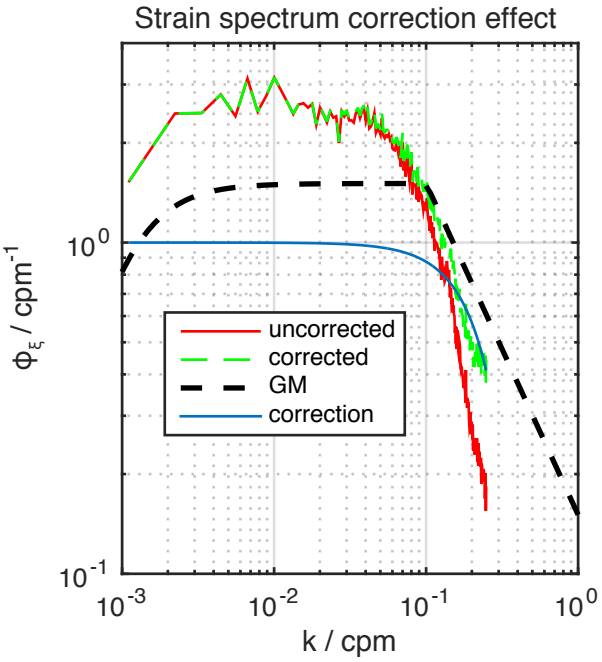

Figure 4.7: Wavenumber spectrum of strain from IWAP MP1showing uncorrected spectrum as well as the impact of correcting for the $sinc^2(2k)$ response from the first difference operator.

diurnal frequency than the diurnal. At wavenumbers $k > 10^{-2}$ cpm, we see that the spectral peaks have collapsed to the background continuum levels.

As was seen with velocity, average background spectra of strain for all of the sites have very similar shapes (Fig. 4.9). The site wide average has a form that is highly representative of each site. This form compares well with the GM model having a high wavenumber roll off at roughly $k > 10^{-1}$ cpm with a generally white level at lower wavenumbers $k < 10^{-1}$ cpm that begins to roll off as wavenumber continues to decrease. We do not see a deviation from GM at low wavenumbers as was observed in the velocity spectra.

4.5 Scale factor representation of variability

Our previous results have shown that separation of the two dimensional spectrum into different frequency regions yields site average spectra that represent the shapes of each site

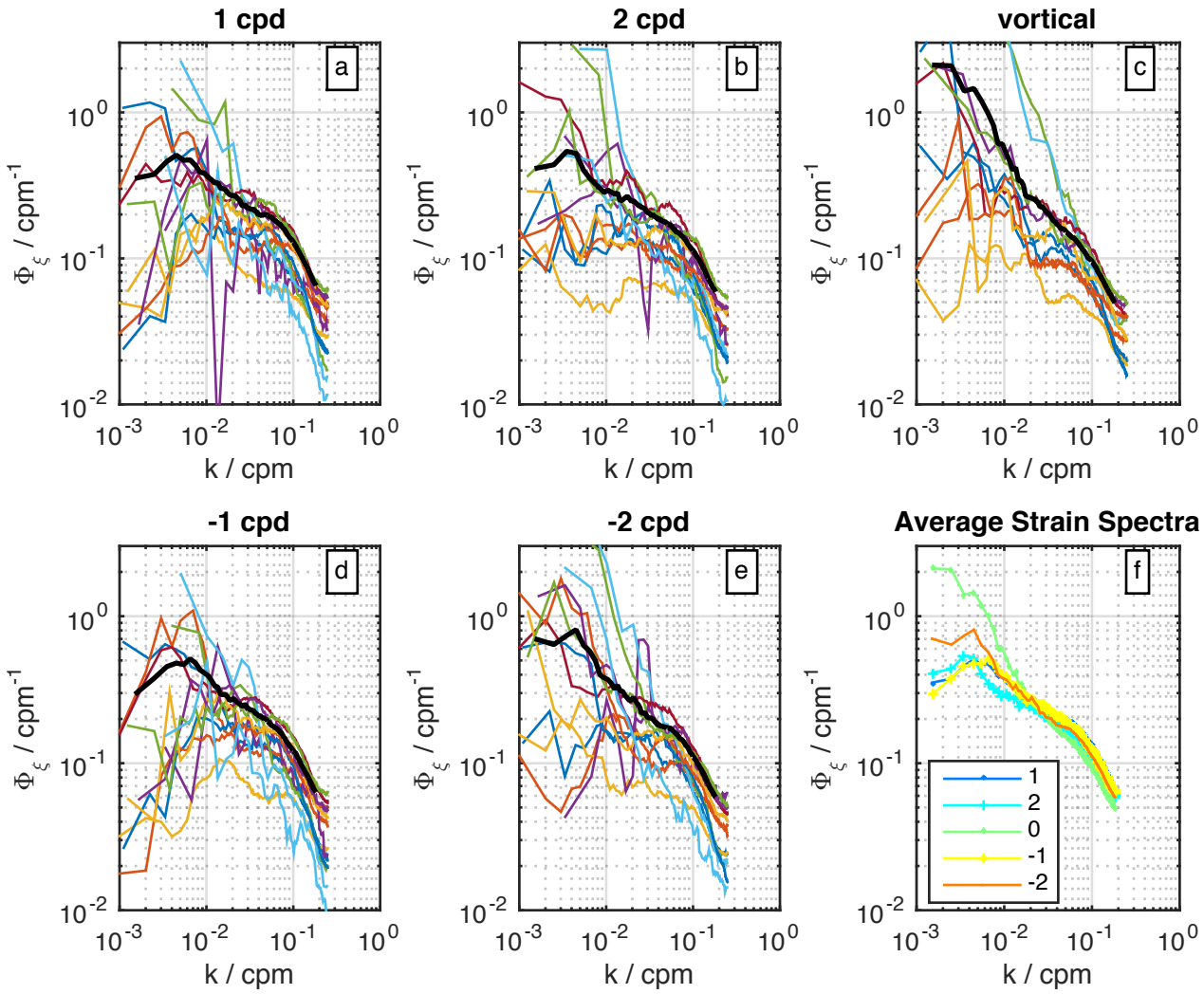

Figure 4.8: Average strain spectra for all mooring sites separated by positive and negative frequency and vortical mode contributions. In panels a,b,c,d,e each color indicates a different mooring while in panel f colors are used to distinguish between frequency bands.

well. Further, the variability in the narrow band peaks can be constrained to exist primarily at wavenumbers $k < 10^{-2}$ cpm. In order to examine what drives site to site variability in both the background continuum and in the low wavenumber narrow band peak regions, site to site variability is reduced to a set of scalar values describing the spectral level in each wavenumber and frequency region relative to the other sites.

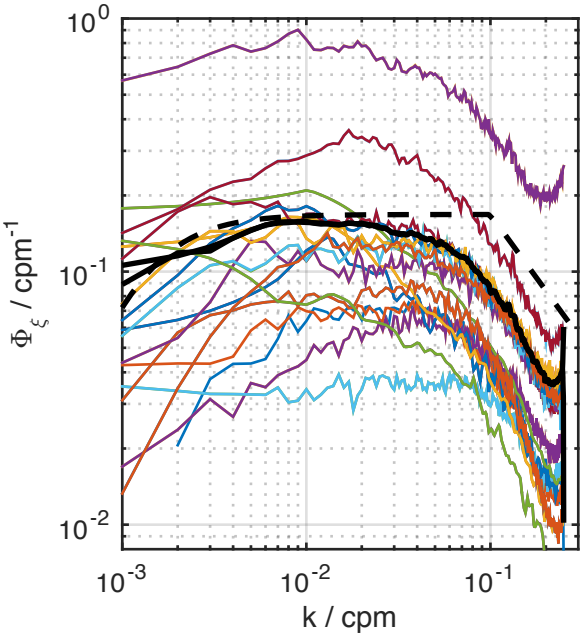

Figure 4.9: Average strain spectra for all mooring sites in frequencies that are not ± 1,2,f. Each color is a different MP, the thick black line is the average spectrum, the dashed line shows an $E_{strain} = 1$ spectrum that has been scaled so the shape can be compared to the observed non peak spectra.

Because the average wavenumber spectrum in these regions has a shape that faithfully represents the shape of the spectra at all of the sites, we can express the spectrum of each site as the scalar that when multiplied by the mean spectrum minimizes the RMS deviation from the observed. By doing this, we can express relative spectral levels of all the sites, in each frequency band, as a scale factors. This method allows us to focus on forces effecting relative variability instead of absolute magnitude or in other words to look at how the range of various local factors captured by the MPs impacts spectral power. Scale factors are calculated using a Nelder-Mead simplex minimization scheme. For the narrow band forcing frequencies the minimization is done only considering wavenumbers $k < 10^{-2}$ cpm while for the background continuum the wave wavenumber domain over which the minimization is carried out is the full range of resolved wavenumbers.

4.5.1 Background continuum scale factors

Scale factors for the background velocity field and the background strain field are shown in figure 4.10. By design, the average scale factor is 1. In strain, however, the average is biased high because of the elevated strain scale factor at Philex MP2. If we do not consider this elevated value, the average spectral scale factor is actually 0.76. This does not mean that the strain spectral levels are "low", as the method here is designed to highlight relative variability and focus should be placed on the relative magnitudes of considered points and not the absolute value.

In figure 4.10 the sites are displayed in no particular order. We see that the velocity spectral background scale factors range from roughly 0.2 to 2 while strain spectral scale factors range from 0.3 to 4.5. We find that in general each site has either elevated velocity or elevated strain spectral scale factors. All three of the Philex MPs exhibit this behavior clearly as seen in the alternating pattern of peaks in velocity and strain spectral scale factors with Philex MP2 and the lower MP at MP1 having relatively large, when compared to the other sites, strain while the upper mooring has relatively large shear.

At all three of the IWAP moorings we find average velocity spectral scale factors but relatively low values of strain. The MC09 moorings also exhibit higher relative levels of velocity than strain. The Mendo 09 mooring has high levels of strain at both the upper and lower MP while the Oregon moorings exhibit instances of both higher strain and lower strain relative to velocity.

The spatial patterns of background spectral scale factors highlights several ideas that we investigate in the following sections. Similarities in background spectral scale factors between sites in similar locations makes it clear that regional properties must influence the background spectral level. E.g. all three of the IWAP moorings are in a relatively similar location north of Hawaii, and all three have similar velocity and strain spectral scale factors. This is the case for the MC09 moorings and the Mendo mooring as well.

There are, however, deviations from this pattern of locally consistent scale factors. Par-

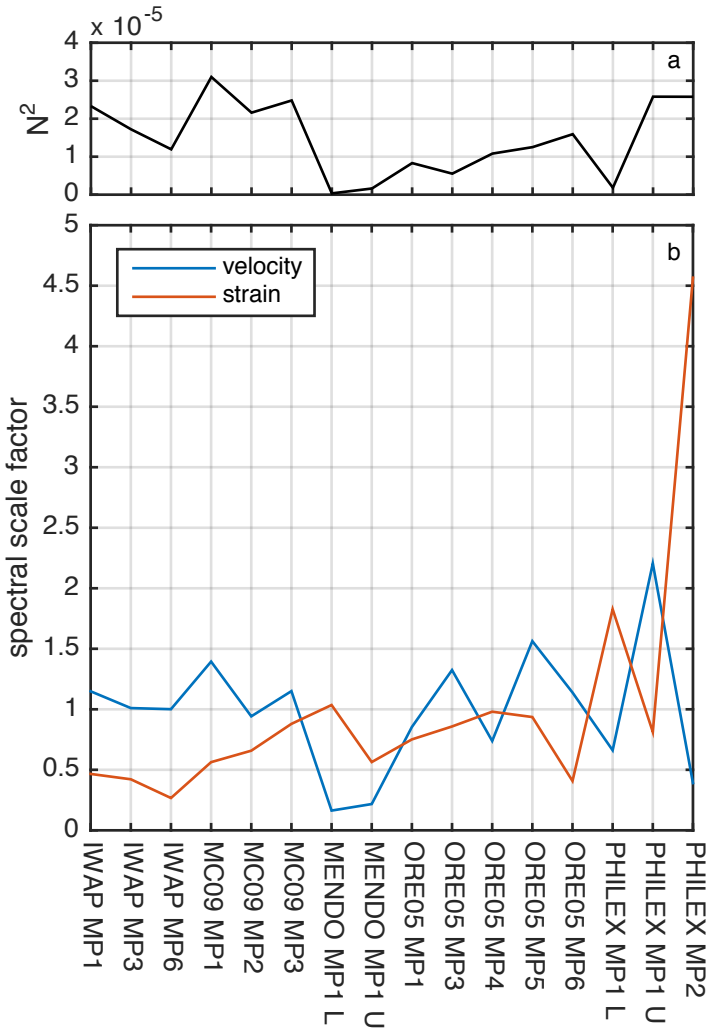

Figure 4.10: a) Average N^2 b) Velocity and strain spectral scale factors for the background continuum

ticularly the ORE05 moorings and Philex. In chapter 3 it was noted that variability in the shear to strain ratio seemed to be related to topographic effects. It is possible that the variability in scale factors at the ORE05 and PHILEX moorings is due to the particularly unique topographic regimes with the ORE05 moorings ranging nearly 100 km from the outer deep ocean mooring up the continental slope and the PHILEX moorings being located in a tidally driven, constrained channel.

Narrow band peak spectral scale factors

The scale factors for the narrow band peaks are computed the same way as the background continuum spectral factors except we are creating scale factors based only on the mean spectrum and observed spectrum at wavenumbers $k < 10^{-2}$. Figure 4.11 shows peak spectral scale factors for all of the sites and in all of the possible combinations of frequencies of interest and wavenumber sign. It is worth nothing that since spectral scale factors are calculated relative to the mean of the frequency/wavenumber grouping, that magnitudes of scale factors can only be compared with scale factors of the same frequency/wavenumber type. However, variability between sites and patterns of variation can be examined.

A prominent feature that appears in figure 4.11 is the relative magnitude of strain spectra at MP2 and at MP3 from the Monterey canyon experiment. Scale factor magnitudes are nearly 4 times the average of the rest of the sites. Curiously, MP1 does not exhibit the same elevated levels of strain. This is different from the background continuum scale factors which showed relatively low levels of scale factors at all 3 of the Monterey moorings. This pattern does not appear in velocity peak scale factors which show more uniform levels at all 3 of the MC09 moorings.

Similarly, in several of the wavenumber/frequency categories, we see that IWAP MP6 has several distinctly different characteristics than the other two IWAP moorings while in the background continuum all 3 moorings exhibit similar scale factors. It is particularly apparent in the positive and negative diurnal frequencies where scale factors at MP6 are greatly reduced.

This change in spatial patterns between scale factors from the background continuum and the narrowband peaks implies that perhaps different mechanisms are influencing the background continuum than the narrow band peaks.

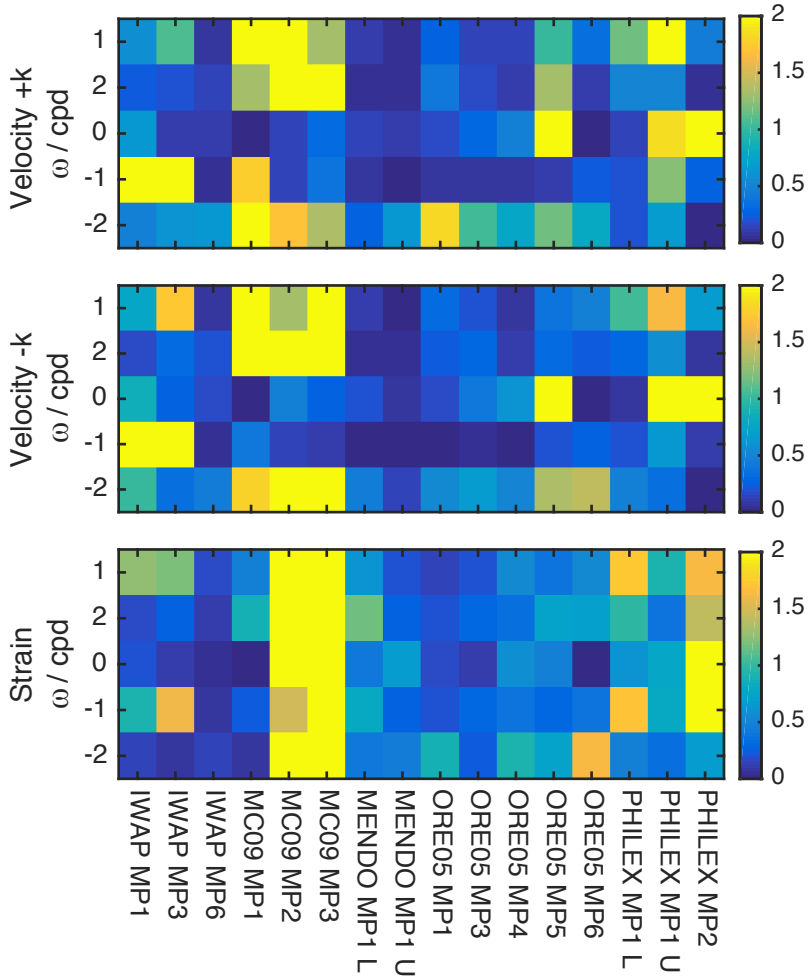

Figure 4.11: All spectral peak scale factors.

4.6 Discussion

Having previously observed different spatial patterns between scale factors in the narrow band peaks and the continuum, which insinuated the potential for different factors driving each regime, we now look for correlations between scale factors and local parameters and investigate the differences in correlations between background continuum and the narrow band peaks.

The potential parameter space is broad and while not exhaustive, we have attempted to investigate a wide range of potential influences. Results from all attempts are not presented and we focus solely on factors that exhibit strong positive relationships and or an unexpected lack of relationship.

4.6.1 Stratification

Average stratification, N, computed over the entire aperture of the two dimensional spectrum, was compared with spectral scale factors from the background continuum of both velocity and strain (Fig. 4.12).

Velocity scale factors exhibit a linear correlation with an $R^2 = 0.341$ and a positive slope. Spectral level scaling with respect to stratification is not a surprise as the GM model has a similar relationship. However, the GM model scales spectral level as a function of N^2, while our observations show the background continuum scale factor varying as a function of N.

The spectral scale factors for the background continuum of strain show no relationship to N. This too is in agreement with the GM model in which the level of the strain spectrum does not vary as a function of N. However, in the GM model the point at which the low wavenumber roll off begins does vary as a function of N. While the point at which the low wavenumber roll off starts is not captured by the spectral scale factors, examination of the mean background strain spectra (Fig. 4.9) shows very little variation in the wavenumber at which roll off is initiated.

The relationship between N and the scale factors for the narrow band peaks is far less clear (Fig. 4.13). The only correlations that approach the R^2 of the relationship between the background continuum and N are in the positive diurnal frequency band. Both the positive and negative wavenumber components of positive diurnal frequency have large values of R^2 with negative wavenumber having an R^2 10 % larger than the positive wavenumbers. None of the narrow band strain scale factors have a significant correlation with N.

Because it is thought that energy enters the internal wave continuum after being injected into narrow band peaks by the storms and the tides, one could hypothesize that the scale

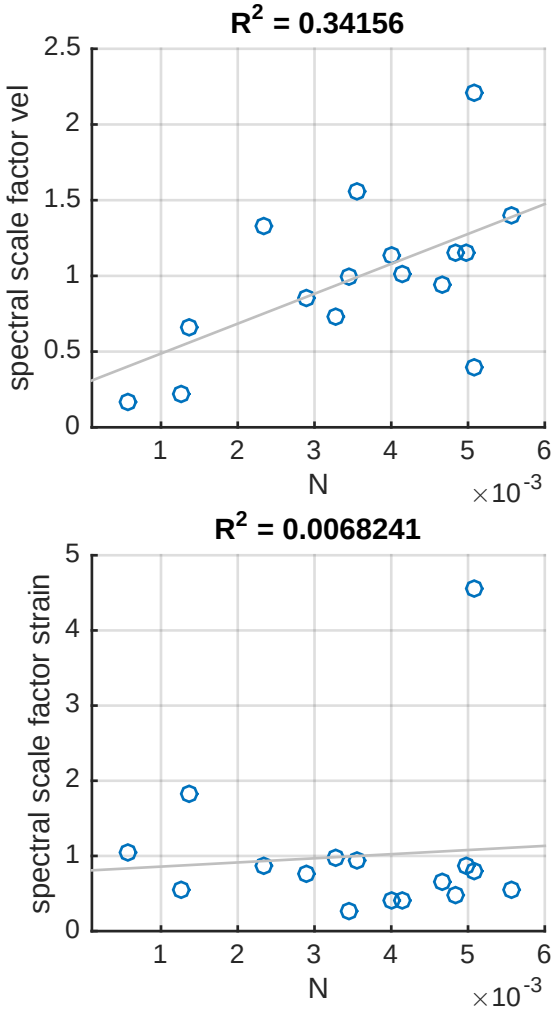

Figure 4.12: Spectral scale factors for velocity and strain plotted as a function of N. Spectral scale factors are computed as the scalar that when multiplied by the mean background spectrum produces a scaled mean spectrum that minimizes the RMS error of the mean spectrum from each site. This produces a vector of scalars that characterizes the background variability amongst our set of sites relative to their mean. This shows that the non peak spectral level scales as N while strain level does not.

factor variability in the diurnal peaks should be proportional to the scale factors in the background continuum. A one to one relationship between diurnal scale factors and background continuum scale factors is not observed (Fig. 4.14). Diurnal scale factors less than two have

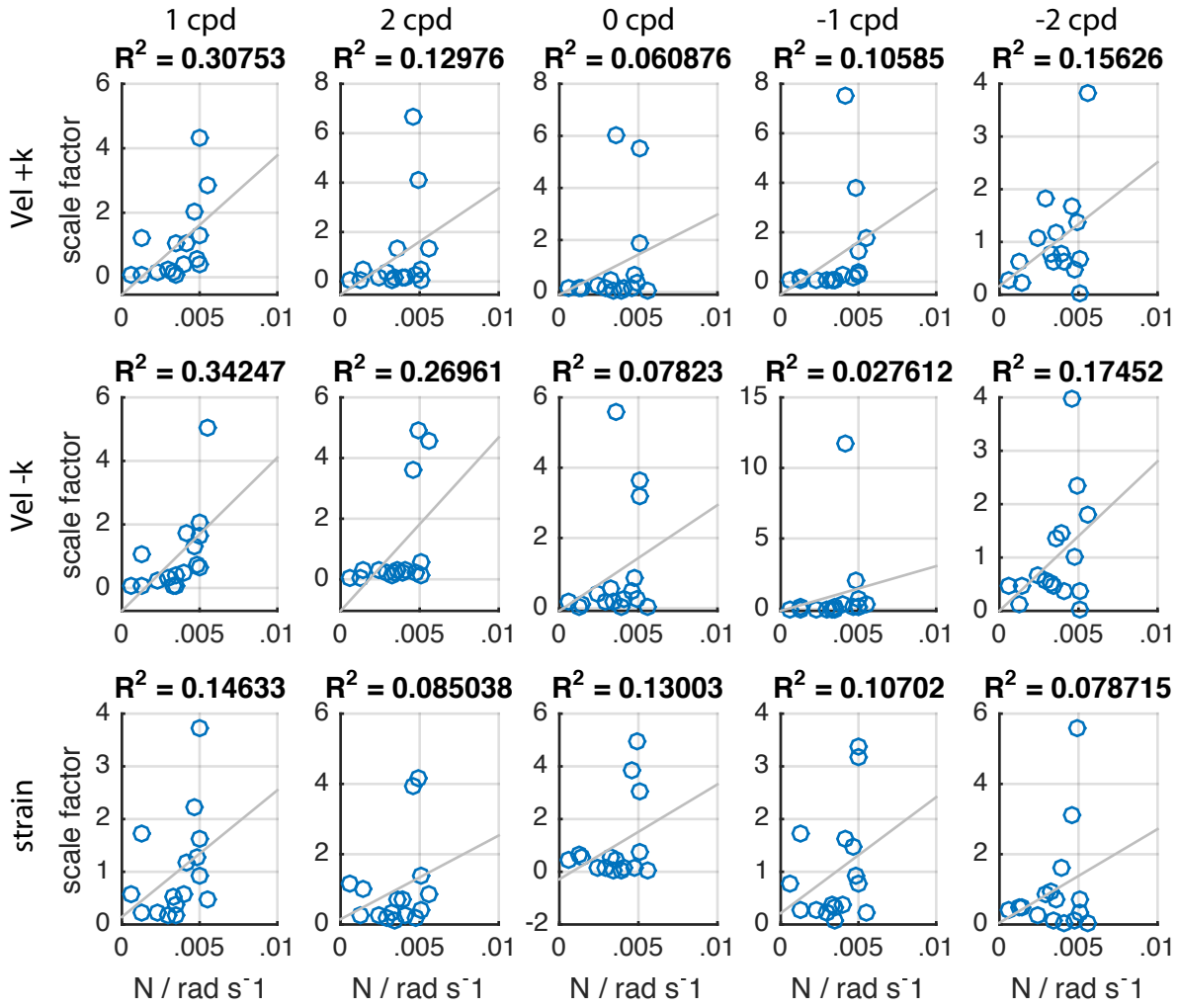

Figure 4.13: Spectral scale factors for velocity and strain plotted as a function of N. Spectral scale factors are computed as the scalar that when multiplied by the mean background spectrum produces a scaled mean spectrum that minimizes the RMS difference from the mean spectrum from each site. This produces a set of scalars that characterizes the background variability amongst our set of sites relative to their mean. This shows that the non peak velocity spectral level scales as N while strain level does not.

corresponding background scale factors that cover a broad range from near zero to 2. This means that over most of the observed range of diurnal peak variation the background spectra could have a low value or a high value relative to the average of all the sites. At higher values, diurnal scale factor > 2, there appears to be a more linear trend with the peak increasing

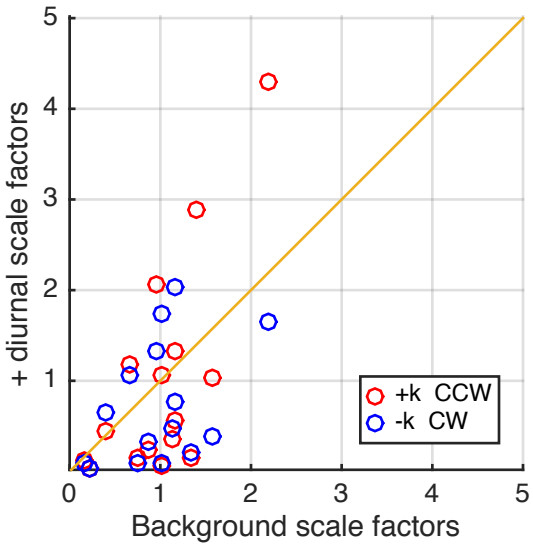

Figure 4.14: Background continuum spectral scale factors for velocity scattered against the scale factors from the positive (CCW rotating with depth) and negative (CW rotating with depth) wavenumber components of the positive diurnal frequency band.

far more rapidly than the background. This trend, however, is given by only 3 points so it is in no way a conclusive result. Again, it is important to note that the variability here is expressed in terms of level relative to the average of this set of observations.

4.6.2 Meters above bottom

In chapter 3 it was found that variability in R_ω was tied to topographic effects. Because in this analysis we can separate the spectrum into different frequency components, we refine this previous discovery.

Figure 4.15 shows both narrow band peak scale factors and background continuum scale factors plotted vs meters above bottom (MAB) computed as the difference between the water depth and the deepest depth reached by the profiler.

In all regimes, we find that the strain spectral scale factors are inversely proportional to MAB. In the background continuum we see a slightly negative slope between 100-4000 MAB

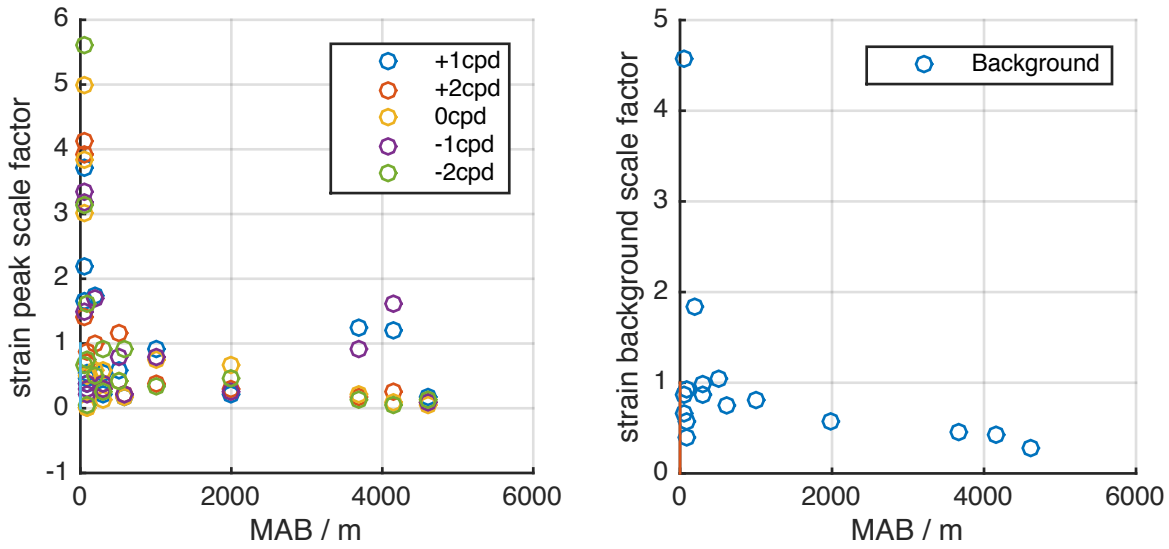

Figure 4.15: Strain spectral scale factors for all MPs at frequency peaks [$\pm 12f$] plotted as a function of meters above bottom (MAB). This shows that the range of strain spectral variability is tied to MAB in that MPs which sample near the bottom may exhibit higher levels of strain while MPs that do not approach the bottom typically have lower levels of strain.

with two sites having large scale factors at very low MAB. Both of these sites exhibiting large scale factors are from the Philex experiment. The Southern mooring, MP2, has a background continuum strain scale factor of ≈ 4.5 and the lower MP (MP1) from the Northern mooring has a scale factor of 1.9.

The narrow band peak strain scale factors exhibit a similar behavior in all frequency regions. There is a decrease in scale factor as MAB increases and a large increase in the range of scale factors at low MAB. At low MAB there is a broad range of scale factor values. As was seen with the background continuum scale factors, these elevated values are associated with Philex MP2 and MP1. At these two moorings the high background strain is accompanied by elevated strain in all 5 of the frequency bands examined here.

4.6.3 GM shape velocity spectra not including peaks

Many observations have been made of velocity spectra that show strong agreement with the GM model. It is remarkable, in fact, how well many observations fit this model considering the scope of the data that the model was based off of. Most of these observations showing agreement with GM, however, have limited capability to determine both frequency content and the wavenumber content of the wave field.

A vertical wavenumber spectrum computed from a vertical profile alone will include variability at all frequencies. The effect of this is potentially significant for a variety of reasons. Fine scale parameterizations of vertical diffusivity are based on the concept of using more readily measurable properties, fine scale shear and strain, as proxies for turbulent dissipation of kinetic energy. The structure of these parameterizations is derived from our understanding of the physics of internal waves and theoretical models that describe the rate what at which energy flows through the internal wave continuum. However, with vertical profiles alone, and no ability to separate frequency content of the wave field, non internal wave based variability will be attributed to internal waves and thus potentially bias estimates of parameterized diffusivity high.

Because these observations permit separation of frequency components, we can evaluate the contribution and spectral levels associated with the vortical mode independently. From Fig. 4.5 and Fig. 4.8 we can see that the vortical band wavenumber spectra have non trivial levels that are similar to both the diurnal and semi-diurnal bands. Frequency band averaged vertical wavenumber spectra of velocity (Fig. 4.5 f) show that at low wavenumbers ($k < 10^{-}2$ cpm) the vortical mode is the third largest frequency band, while the frequency band averaged spectra of strain show that the vortical mode is the largest component (Fig. 4.8f). Without the ability to filter out this component of variability it will attributed to internal waves.

In terms of variation in total variance associated to each frequency band, the differences between the bands is small. Because most of the variations are at low wavenumbers, the

impact of these fluctuations on variance computed by integrating the spectra is far less than the contribution to variance from higher wavenumbers. Despite this, we have found that it is important to understand the contribution of the sum of the narrowband peaks even at these low wavenumbers.

Previously, we calculated the average spectra of the not peak regions of the spectrum, or the background continuum (Fig. 4.6a). It was noted that at wavenumbers, $k > 10^{-2}$ cpm, all of the background spectra had a shape that agreed well with the slope of the GM model. However, at $k < 10^{-2}$ cpm, the spectra whitened dramatically and deviated from the GM slope. If we instead compute the wavenumber spectrum of velocity and include variability from all frequencies including the narrow band peaks we find that the total spectrum agrees much closer with GM even at $k < 10^{-2}$ cpm (Fig. 4.6b).

4.7 Conclusions

The wavenumber frequency spectrum of velocity and strain from 14 moorings has been examined to evaluate how various factors influence the shape of the spectrum. From quantifying the separability of the two dimensional spectrum, it is clear that a separable spectrum with a single wavenumber and frequency structure is incapable of representing variability at both the narrow band peak frequencies and the background continuum. While a separable model can reproduce similar quantities of total variance the constraint of having a single wavenumber structure mis–locates the variance in frequency and wavenumber space.

At wavenumbers $k > 10^{-2}$ cpm and at $\omega < 4.5$ cpd we find that the narrow band peaks have merged with the background continuum and that spectral level is essentially white in frequency and attenuating at a rate similar to GM76 in wavenumber. At $\omega > 4.5$ cpd spectral levels attenuate in frequency.

Averaging over the narrow band spectra of all of the sites reveals that the largest regions of variability in the narrow band peaks of the wavenumber frequency spectrum of velocity and strain are at $k < 10^{-2}$ cpm. While there is some site to site variability in spectral levels at $k > 10^{-2}$ cpm, the site averages all converge at wavenumbers $k > 10^{-2}$ cpm.

Spectral variability was converted into scale factors relative to the site wide average spectrum for the background continuum and each of the narrow band peak frequency bands independently. Variability in the background continuum of velocity was found to be closely tied to stratification, N, as opposed to N^2 as in the GM76. Narrow band peak scale factors were found to scale with N only weakly except in the positive diurnal band. No relationship was observed between strain scale factors for the narrow band peaks or the background continuum.

Scale factors for both the background continuum and the narrow band peaks were found to be inversely proportional to the meters above the bottom. The largest amplitude strain in the MP records considered here lies at the Southern Philex mooring and the deep mooring at the Northern Philex MP.

The average background continuum wavenumber spectrum of velocity has the same k^{-2} slope as predicted in the GM model at wavenumbers $k > 10^{-2}$ cpm. At $k > 10^{-2}$ cpm, the spectrum of the background continuum whitens and deviates appreciably from GM76. The total wavenumber spectrum of velocity, including the narrow band peaks and the background continuum, more closely resembles the shape of the GM76 spectrum at $k < 10^{-2}$ cpm. The implication is that the GM spectral shape is not that of the background continuum alone, but actually represents the combined contribution of the narrow band peaks and the background continuum.

4.8 Bibliography

J. L. Cairns and G. O. Williams. Internal wave observations from a midwater float, 2. *J. Geophys. Res.*, 81:1943–1950, 1976.

C. Garrett and W. Munk. Space-time scales of internal waves. *Geophys. Fluid Dyn.*, 3: 225–264, 1972.

K. D. Leaman and Thomas B Sanford. Vertical energy propagation of inertial waves: A vector spectral analysis of velocity profiles. *J. Geophys. Res.*, 80(15):1975–1978, 1975.

R Pinkel. Doppler sonar observations of internal waves: the wavenumber-frequency spectrum. *J. Phys. Oceanogr.*, 14(8):1249–1271, 1984.

4.9 Appendix

Observed wavenumber frequency spectrum of velocity and optimal separable representations for each of the MPs used in this analysis.

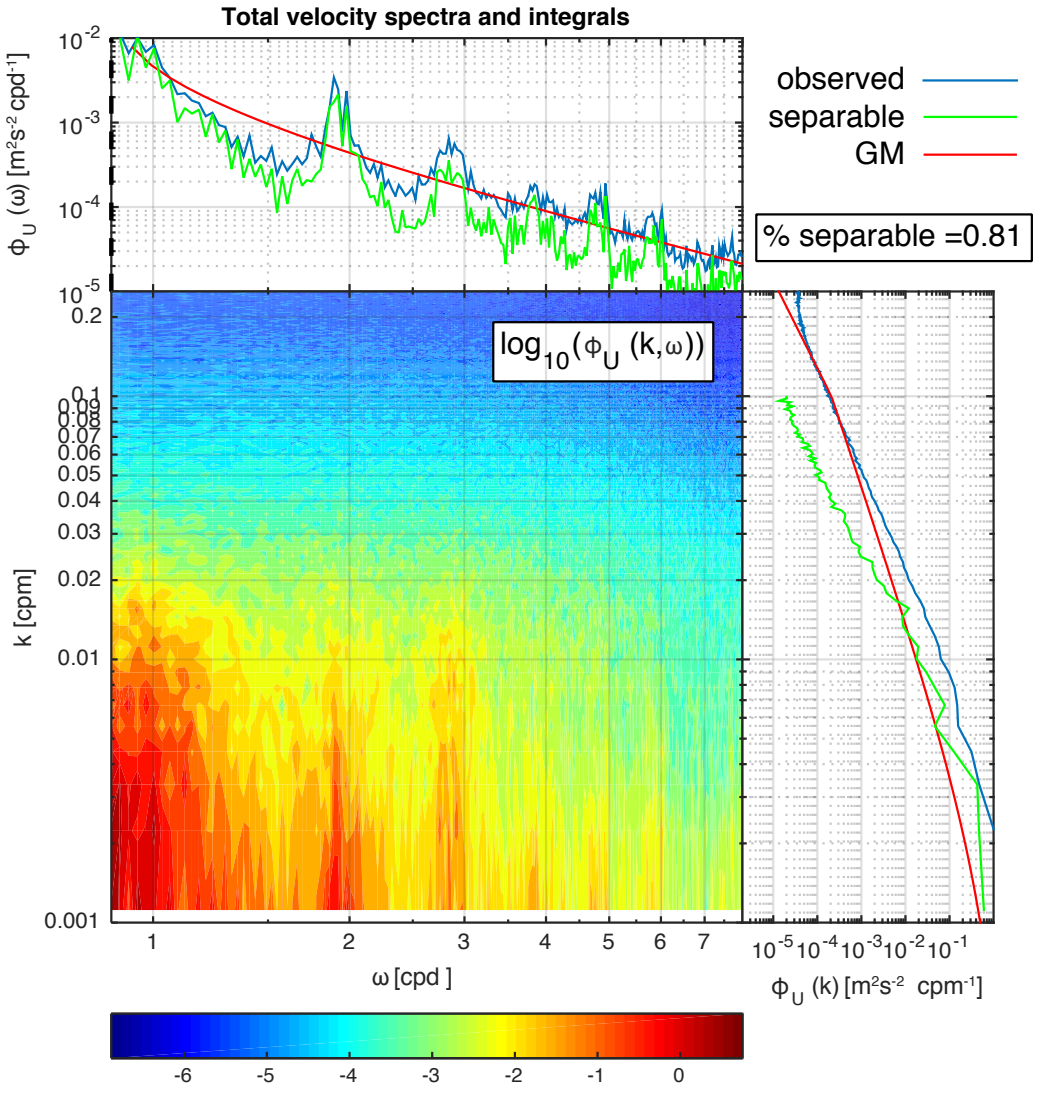

Figure 4.16: Total velocity spectrum from IWAP MP1 shown with integrated frequency spectrum and integrated wavenumber spectrum of observations and optimal separable wavenumber and frequency forms.

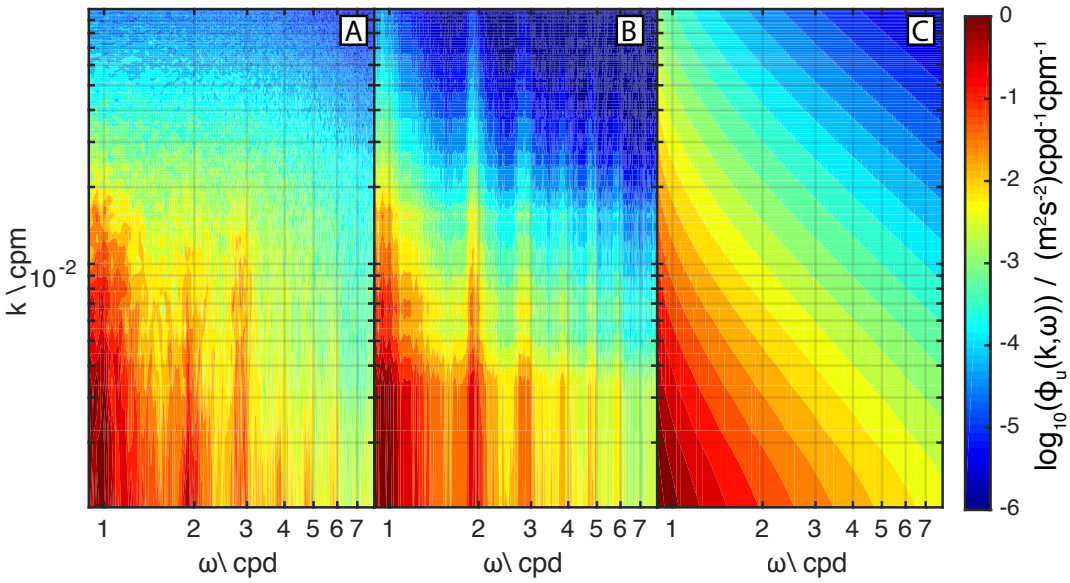

Figure 4.17: IWAP MP1 total velocity spectra a) observed, b) optimal separable, c) GM model

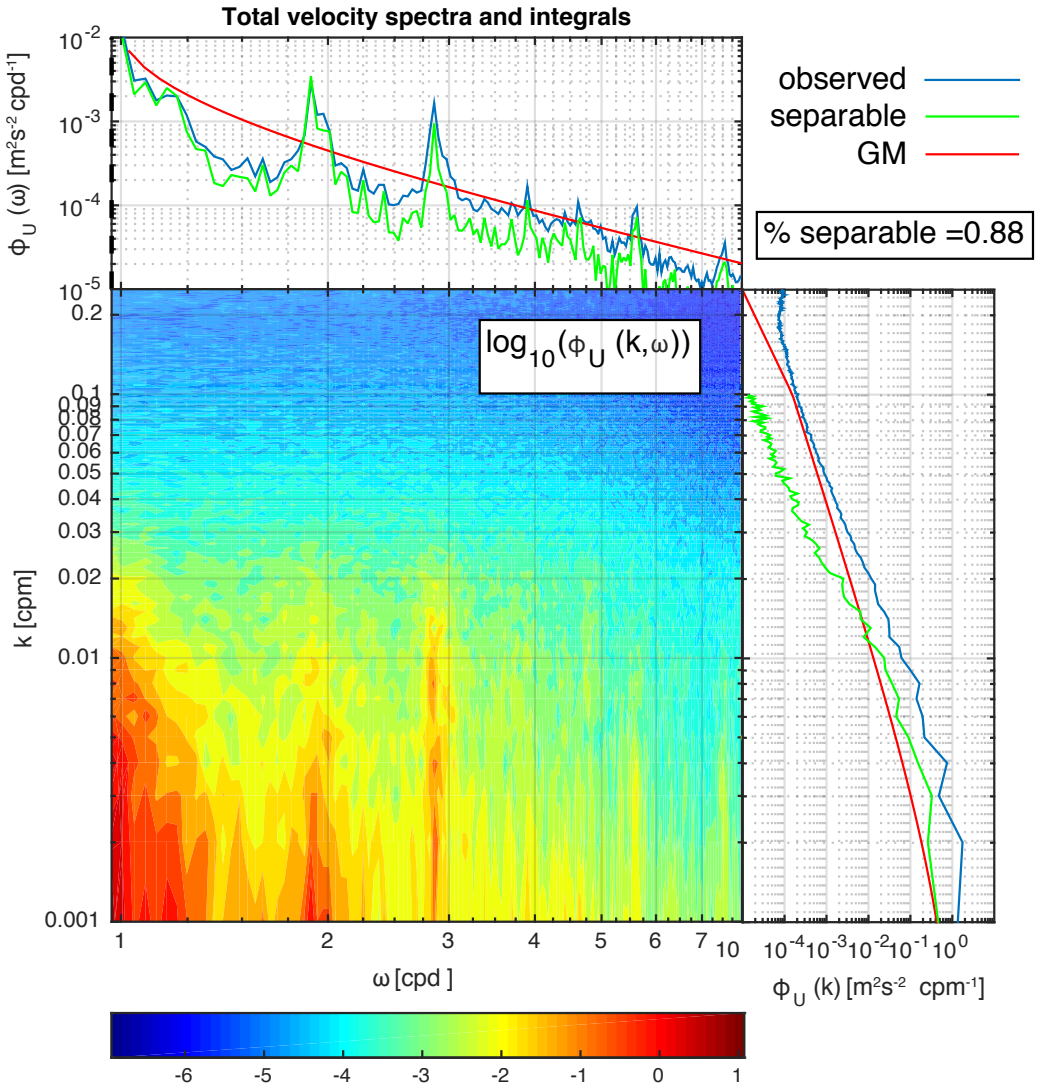

Figure 4.18: Total velocity spectrum from IWAP MP3 shown with integrated frequency spectrum and integrated wavenumber spectrum of observations and optimal separable wavenumber and frequency forms.

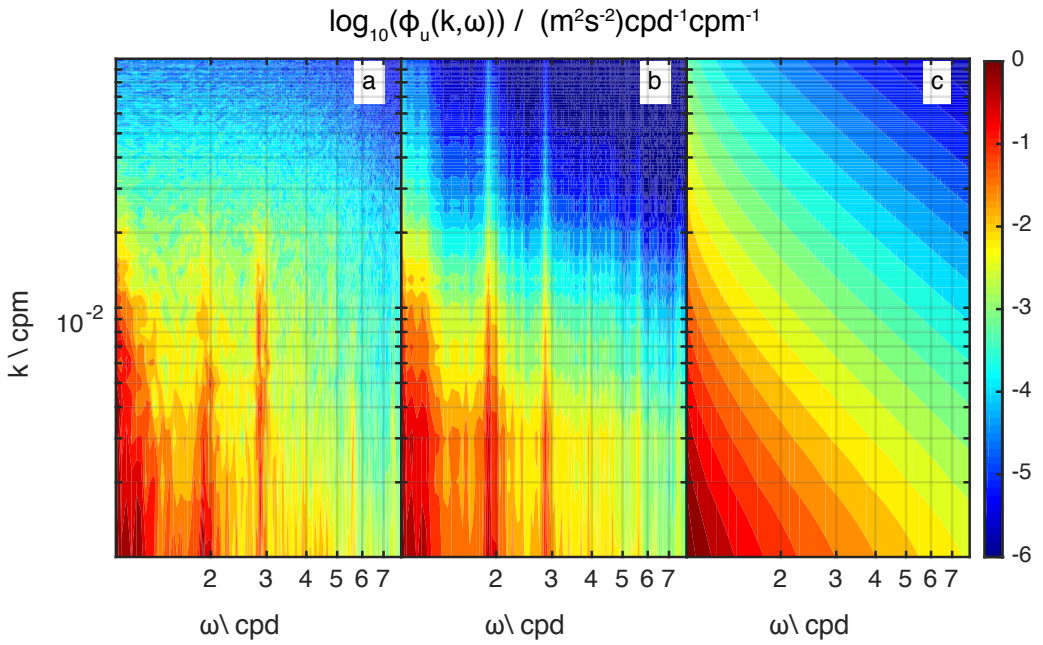

Figure 4.19: IWAP MP3 total velocity spectra a) observed, b) optimal separable, c) GM model

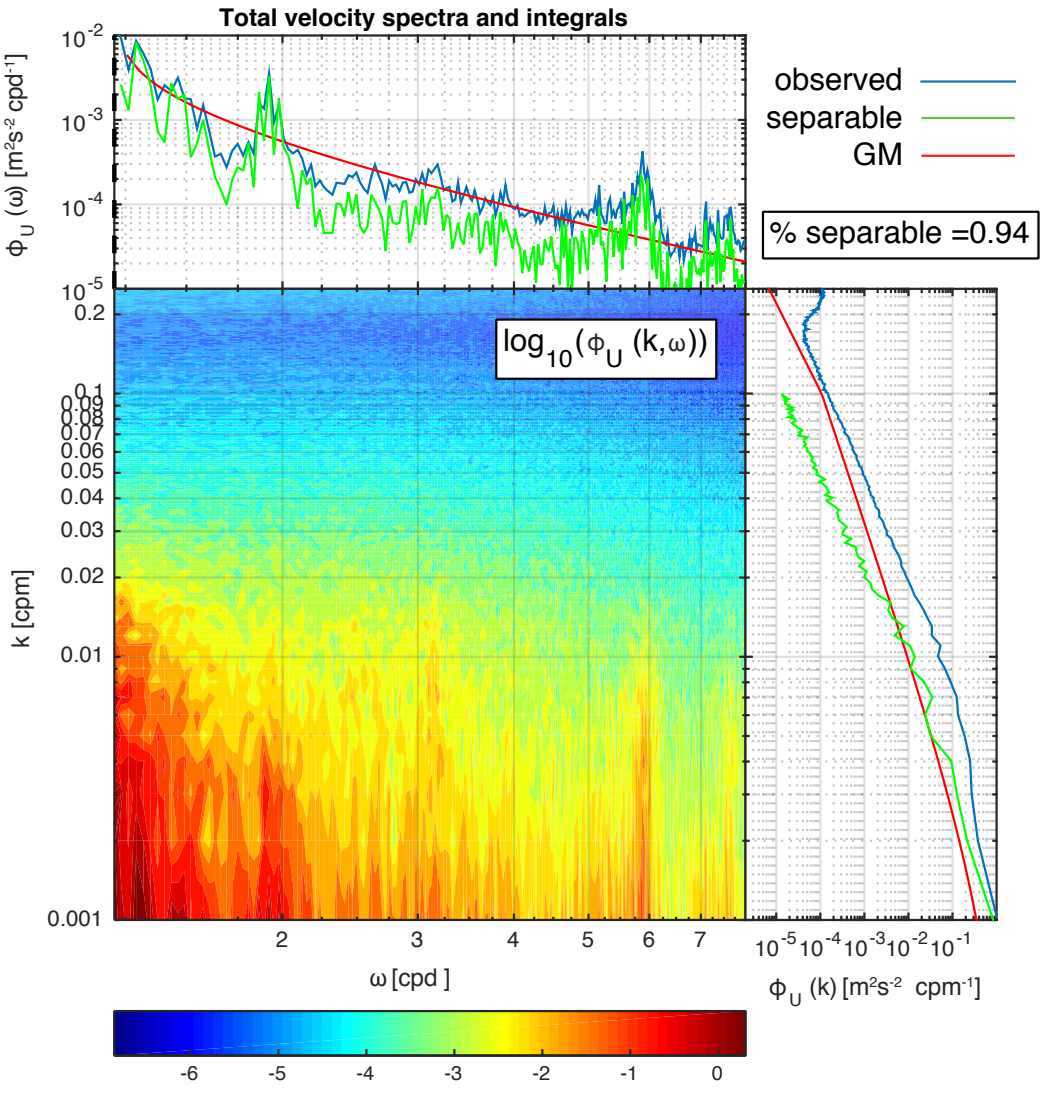

Figure 4.20: Total velocity spectrum from IWAP MP6 shown with integrated frequency spectrum and integrated wavenumber spectrum of observations and optimal separable wavenumber and frequency forms.

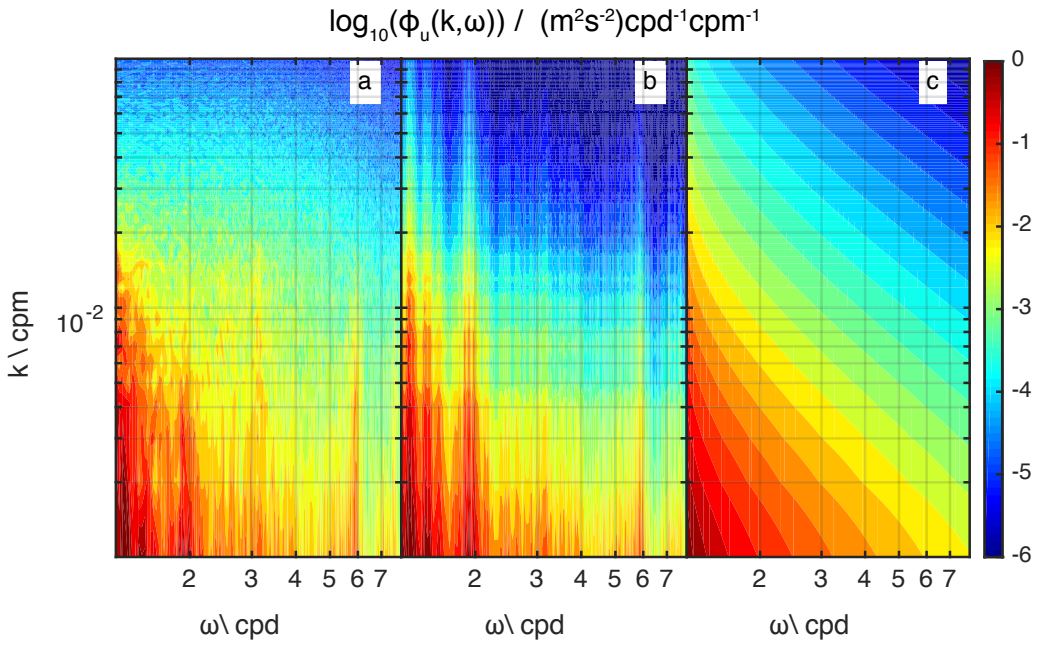

Figure 4.21: IWAP MP6 total velocity spectra a) observed, b) optimal separable, c) GM model

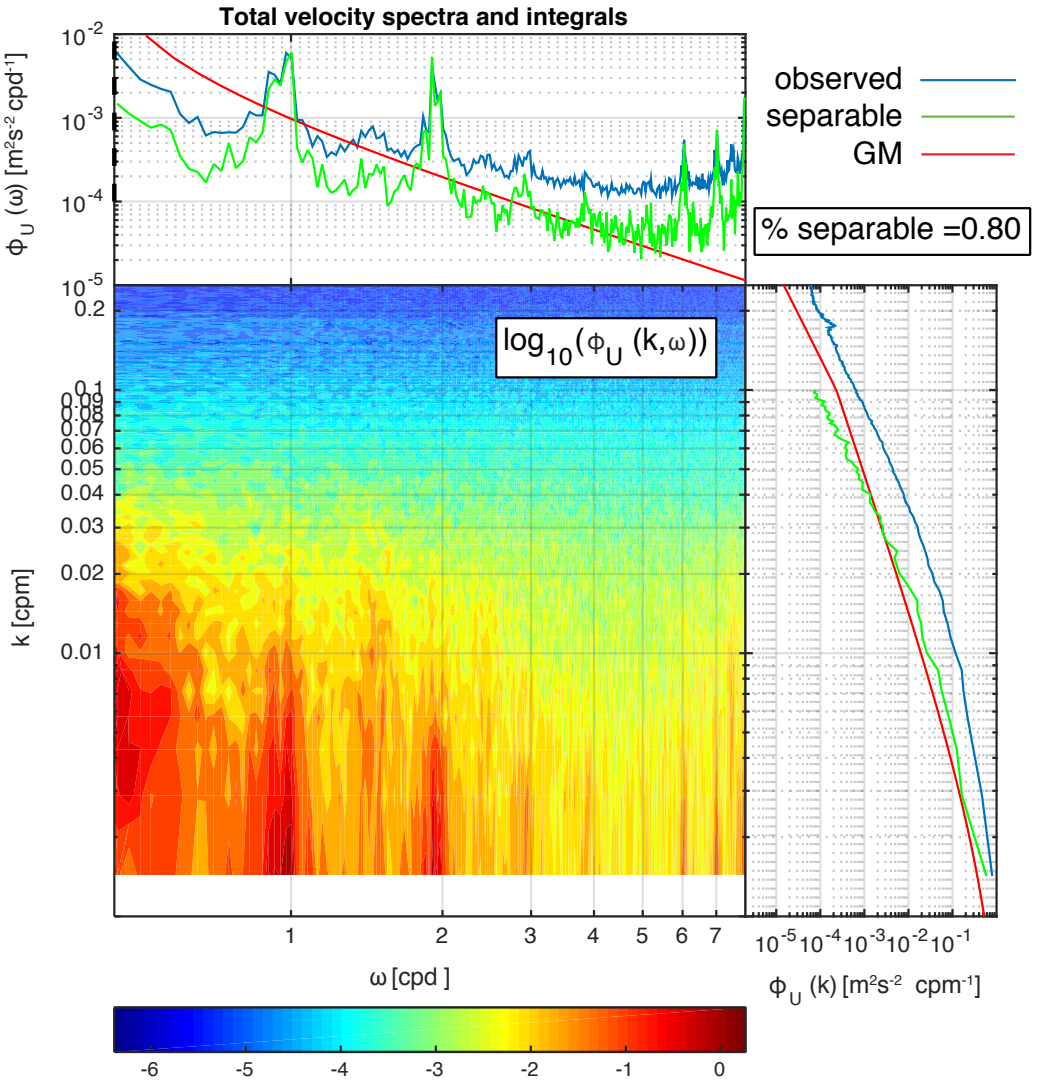

Figure 4.22: Total velocity spectrum from Philex MP1 upper shown with integrated frequency spectrum and integrated wavenumber spectrum of observations and optimal separable wavenumber and frequency forms.

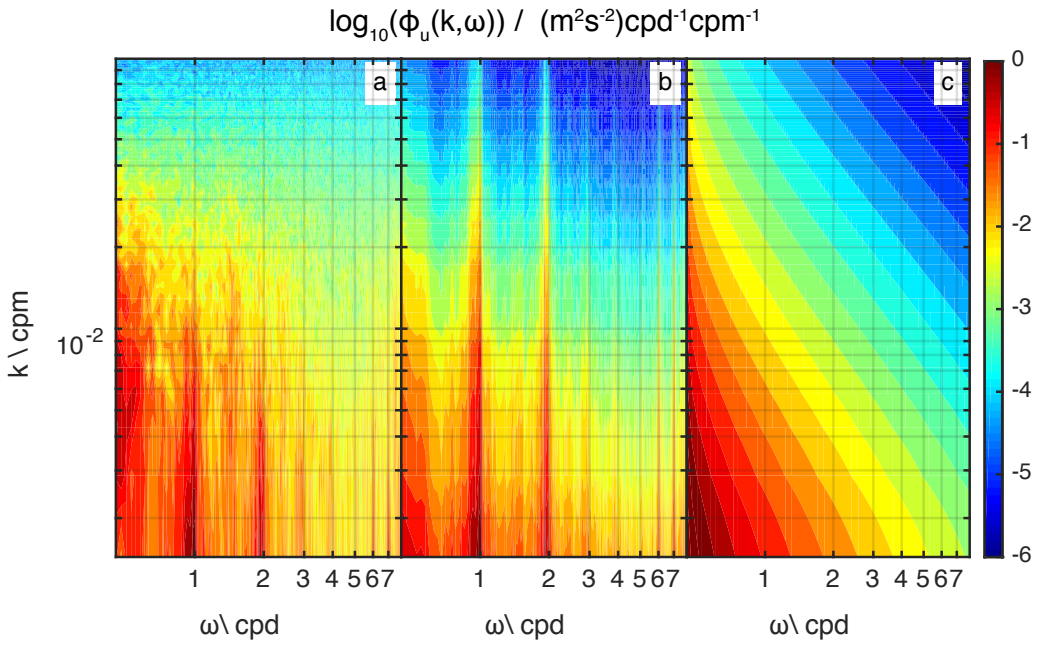

Figure 4.23: Philex MP1 upper total velocity spectra a) observed, b) optimal separable, c) GM model

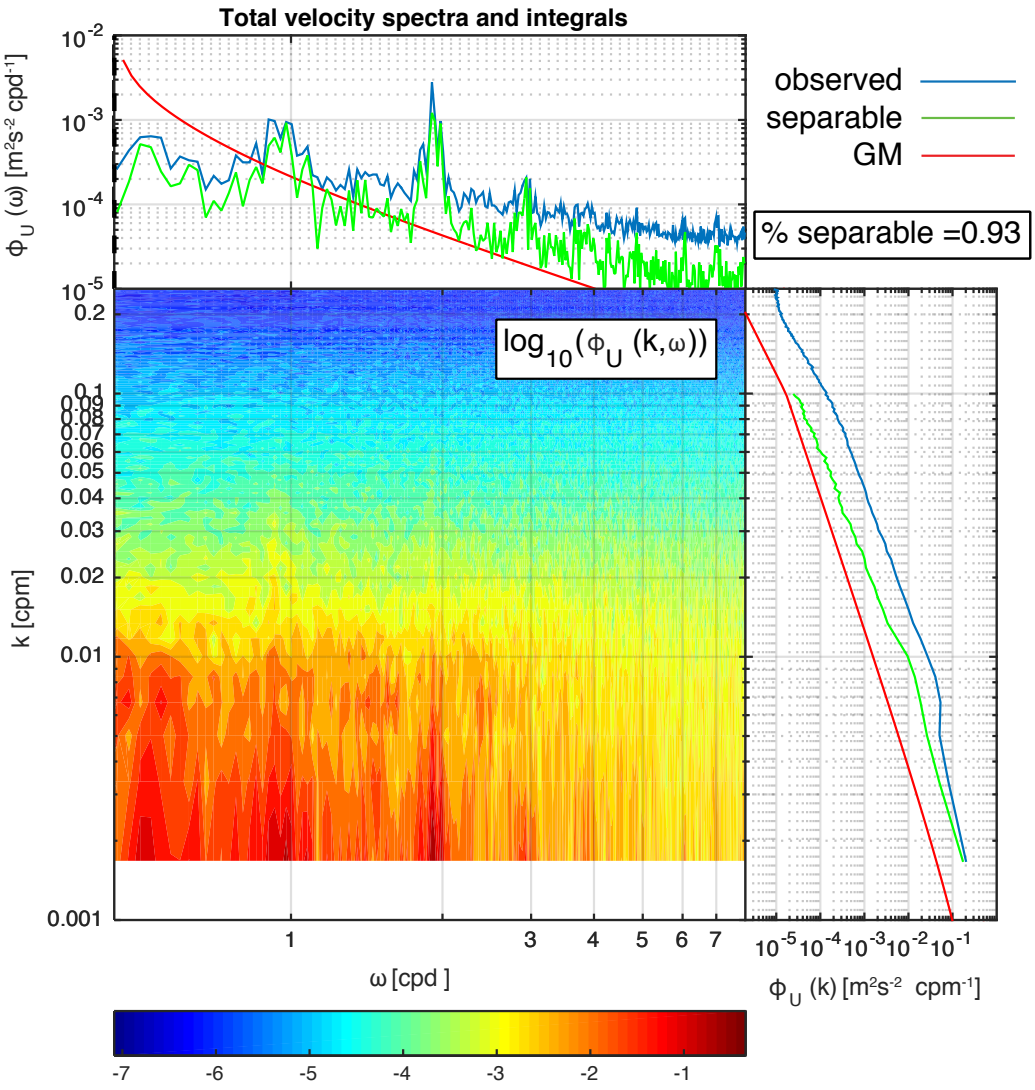

Figure 4.24: Total velocity spectrum from Philex MP1 lower shown with integrated frequency spectrum and integrated wavenumber spectrum of observations and optimal separable wavenumber and frequency forms.

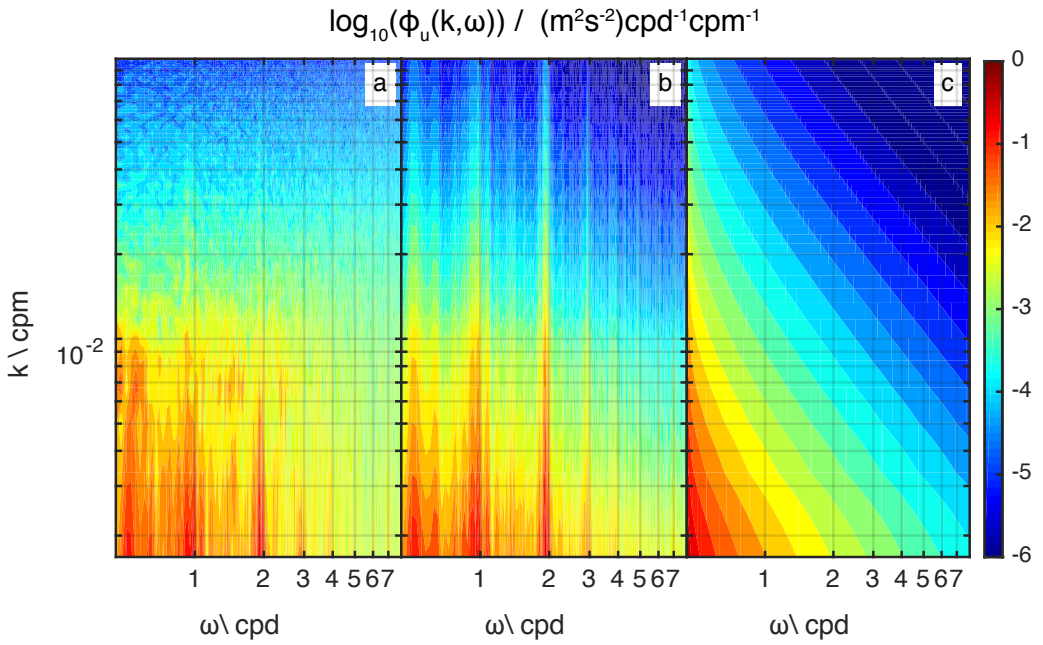

Figure 4.25: Philex MP1 lower total velocity spectra a) observed, b) optimal separable, c) GM model

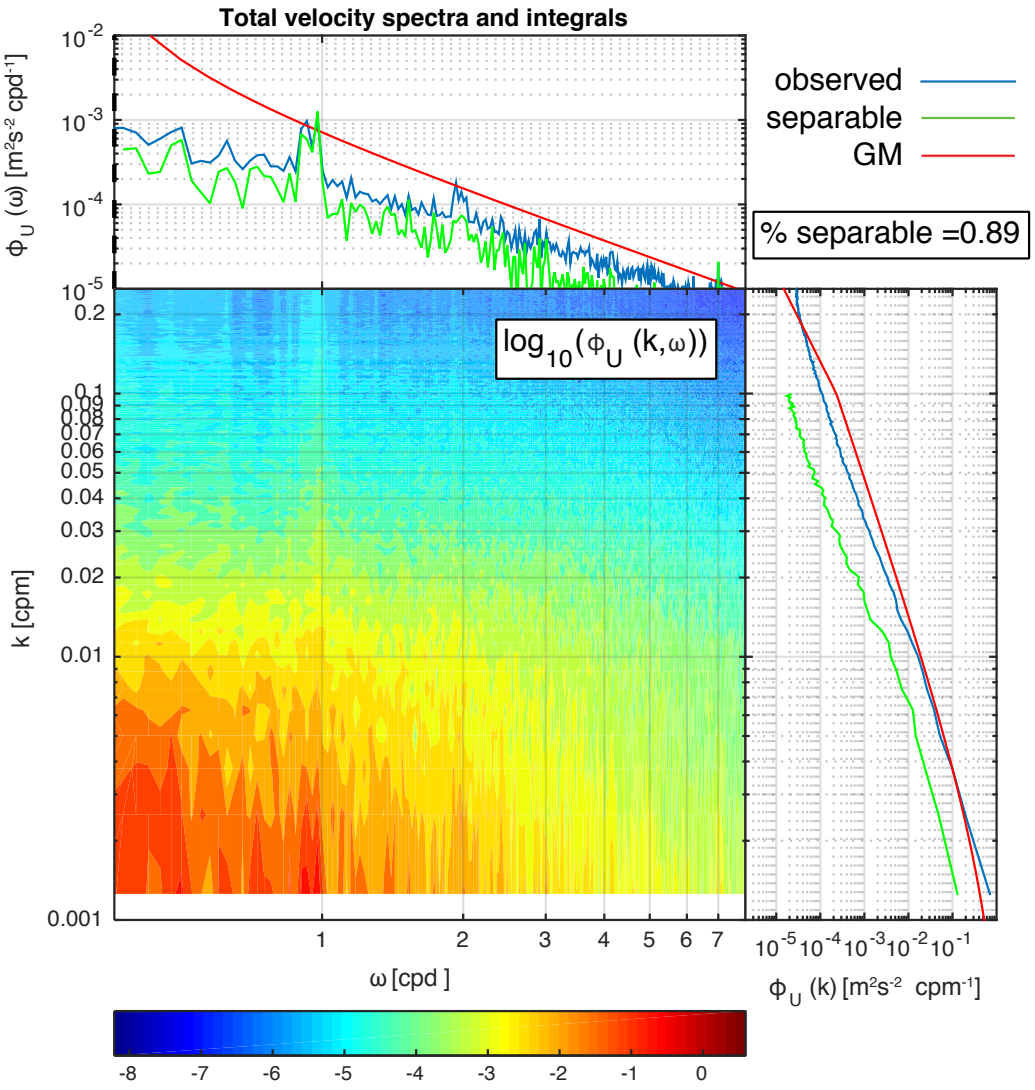

Figure 4.26: Total velocity spectrum from Philex MP2 shown with integrated frequency spectrum and integrated wavenumber spectrum of observations and optimal separable wavenumber and frequency forms.

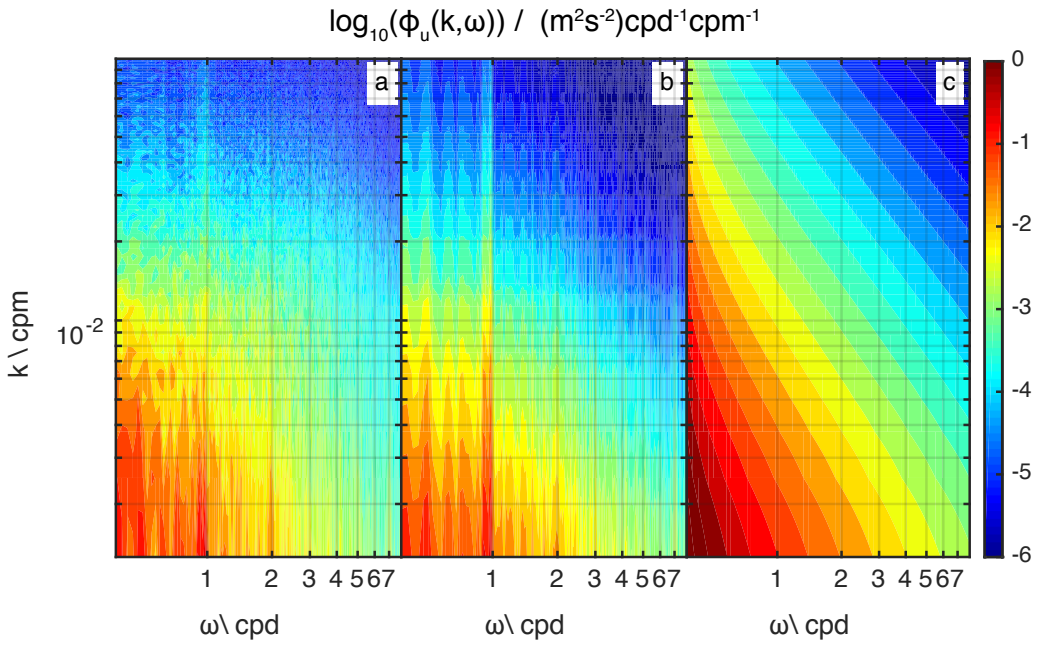

Figure 4.27: Philex MP2 total velocity spectra a) observed, b) optimal separable, c) GM model

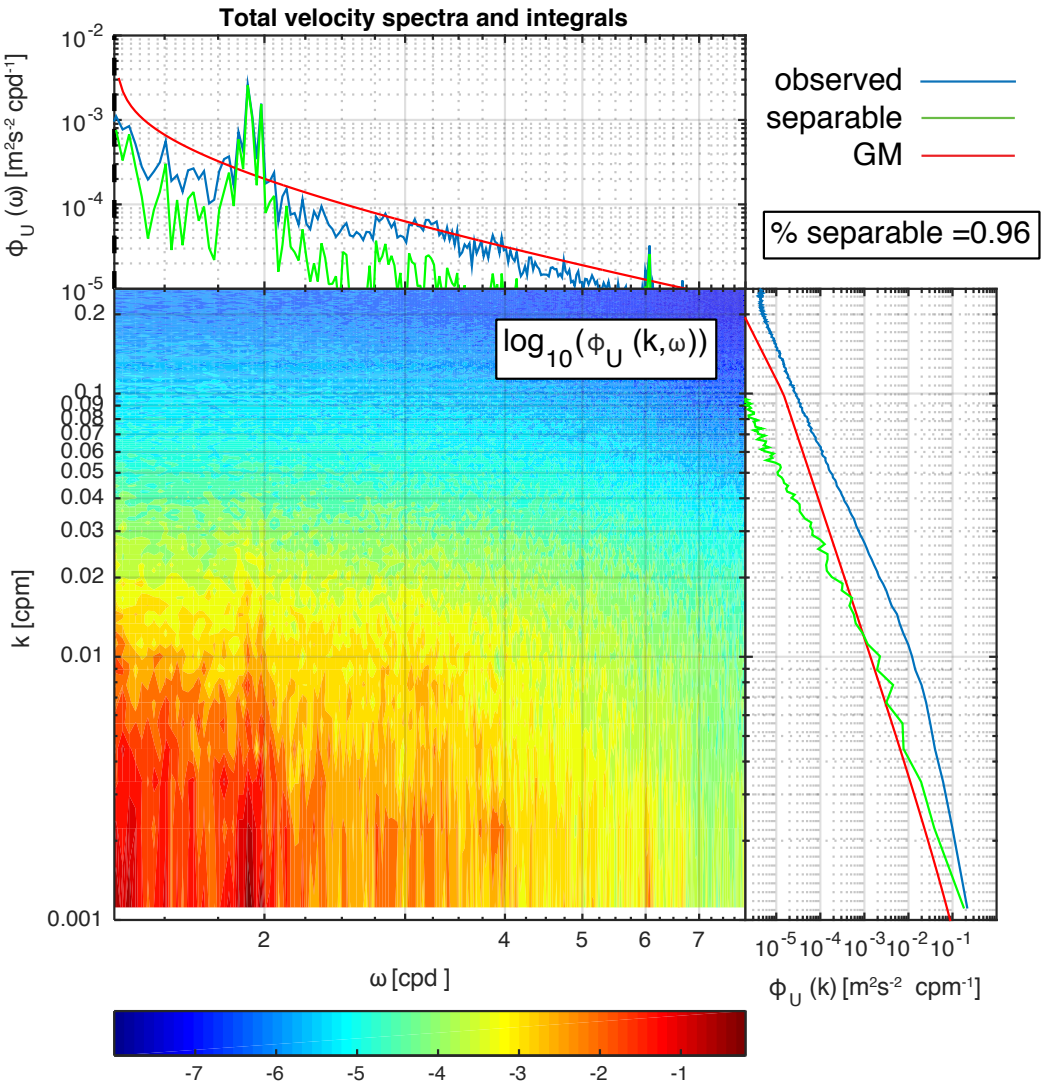

Figure 4.28: Total velocity spectrum from Mendocino MP1 upper shown with integrated frequency spectrum and integrated wavenumber spectrum of observations and optimal separable wavenumber and frequency forms.

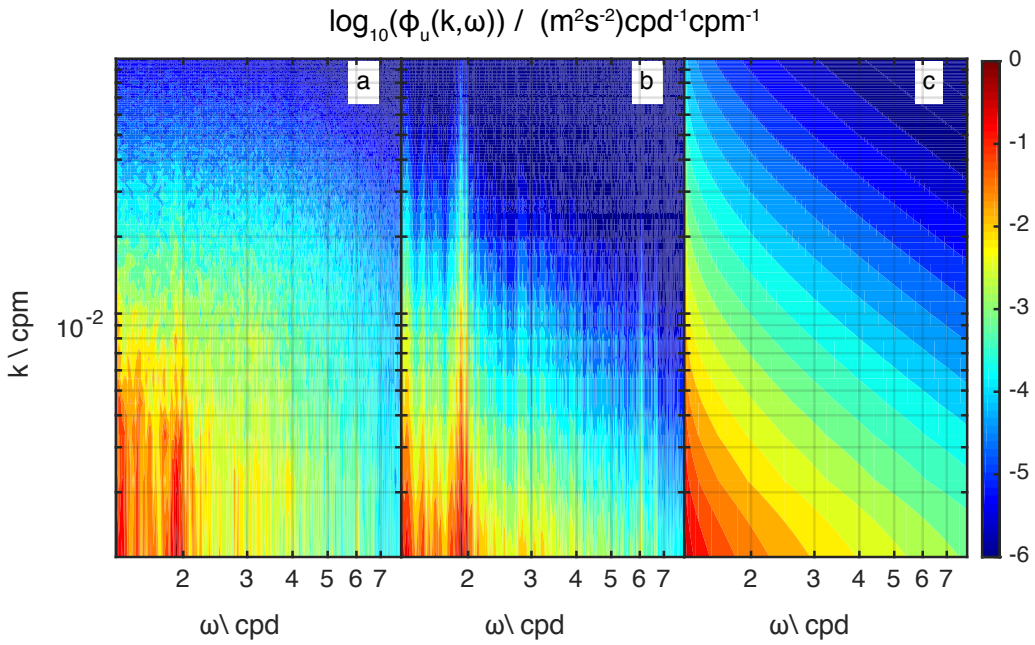

Figure 4.29: Mendocino MP1 upper total velocity spectra a) observed, b) optimal separable, c) GM model

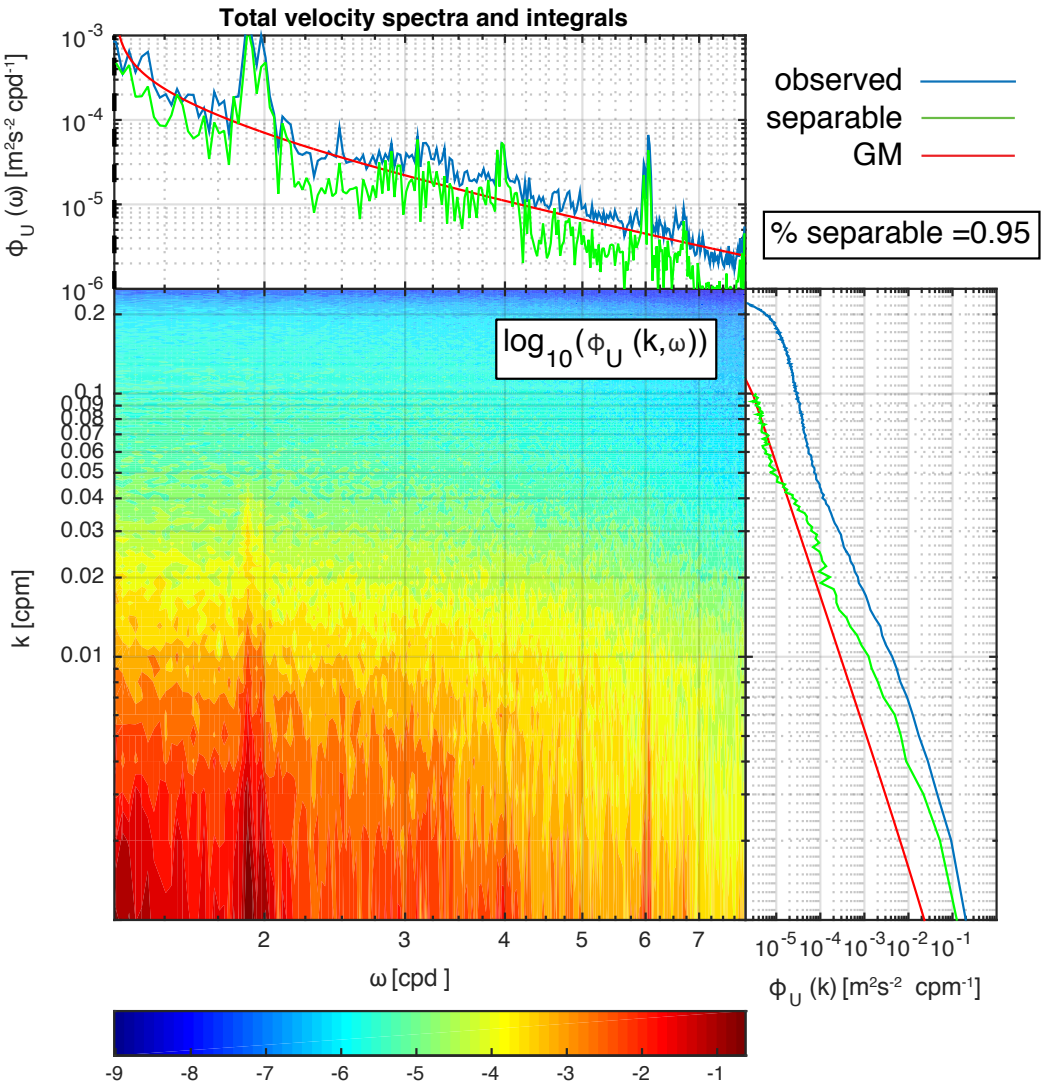

Figure 4.30: Total velocity spectrum from Mendocino MP1 lower shown with integrated frequency spectrum and integrated wavenumber spectrum of observations and optimal separable wavenumber and frequency forms.

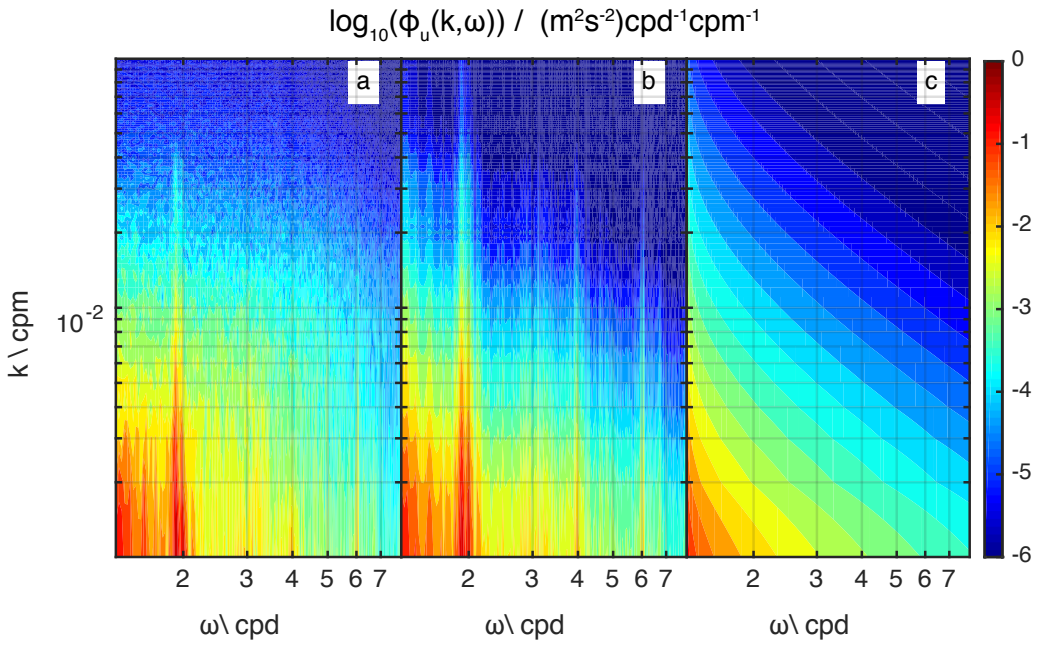

Figure 4.31: Mendocino MP1 lower total velocity spectra a) observed, b) optimal separable, c) GM model

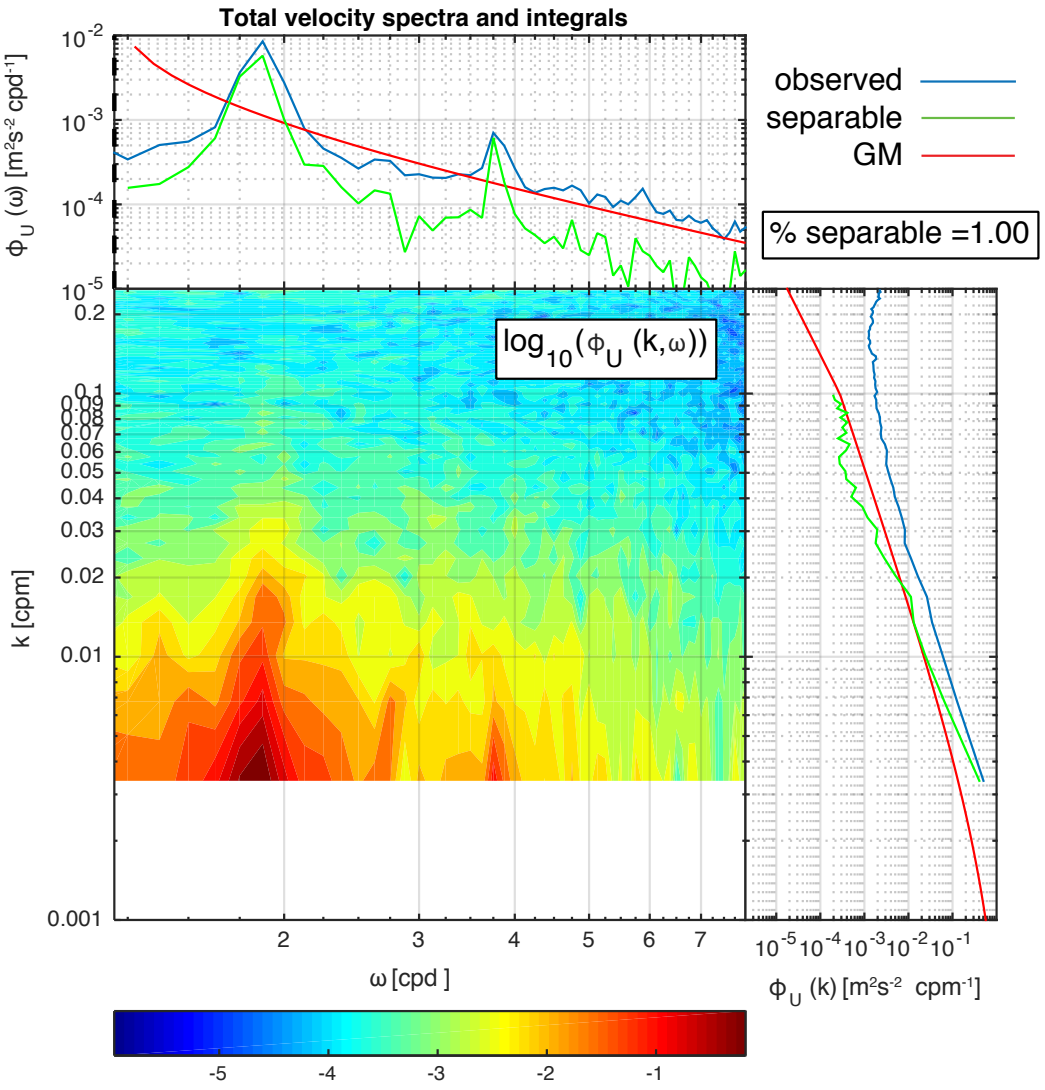

Figure 4.32: Total velocity spectrum from MC09 MP1 shown with integrated frequency spectrum and integrated wavenumber spectrum of observations and optimal separable wavenumber and frequency forms.

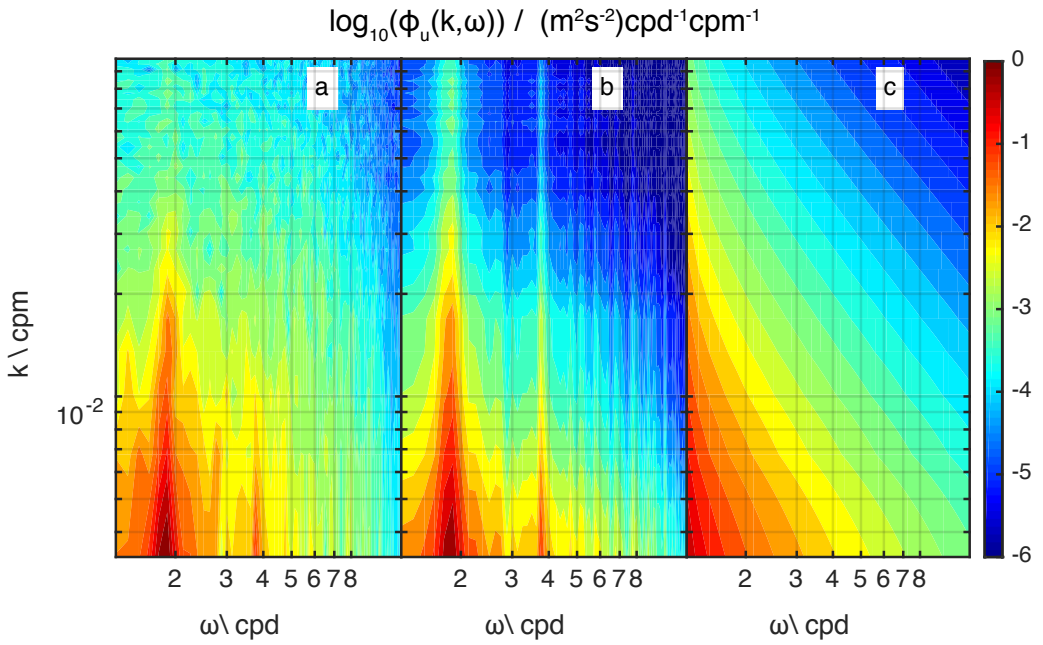

Figure 4.33: MC09 MP1 total velocity spectra a) observed, b) optimal separable, c) GM model

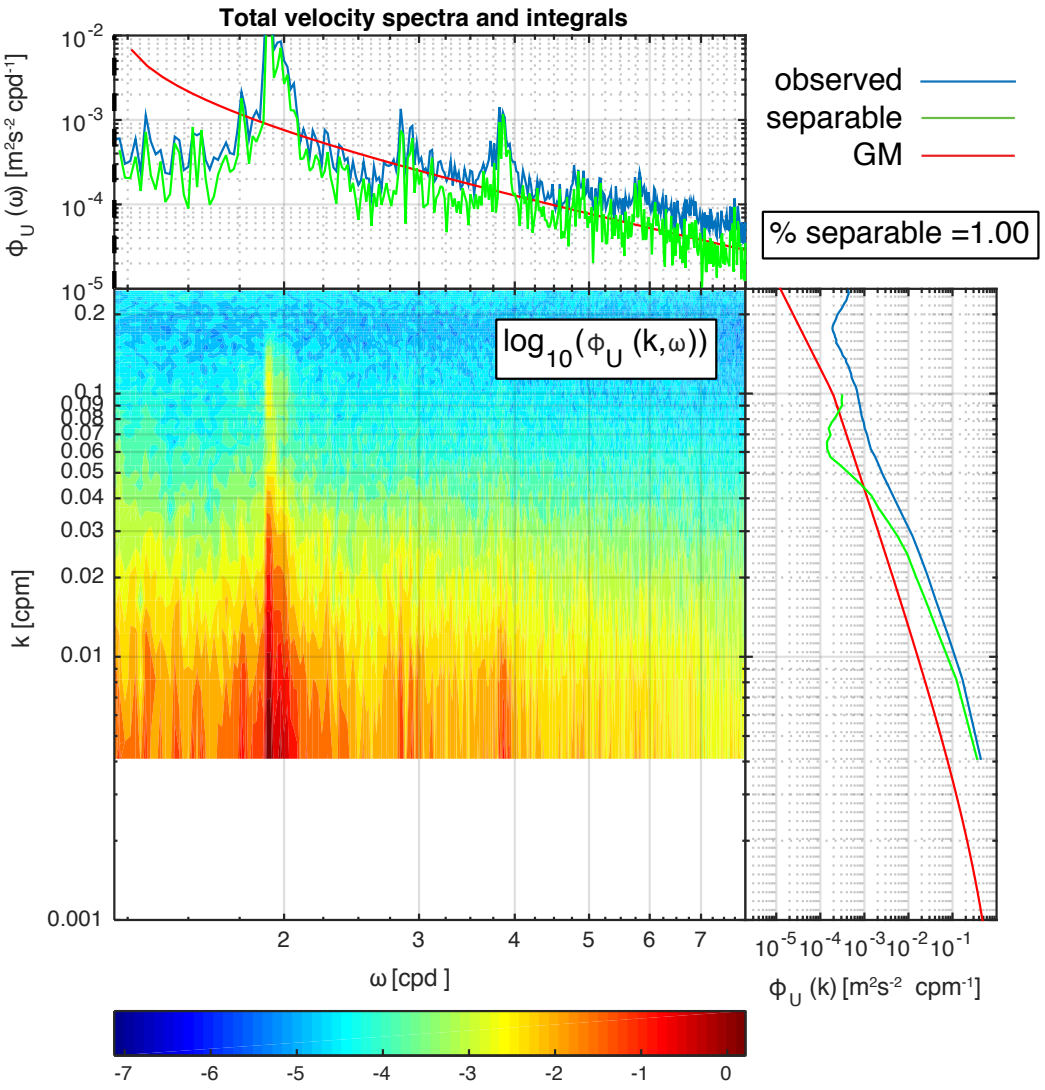

Figure 4.34: Total velocity spectrum from MC09 MP2 shown with integrated frequency spectrum and integrated wavenumber spectrum of observations and optimal separable wavenumber and frequency forms.

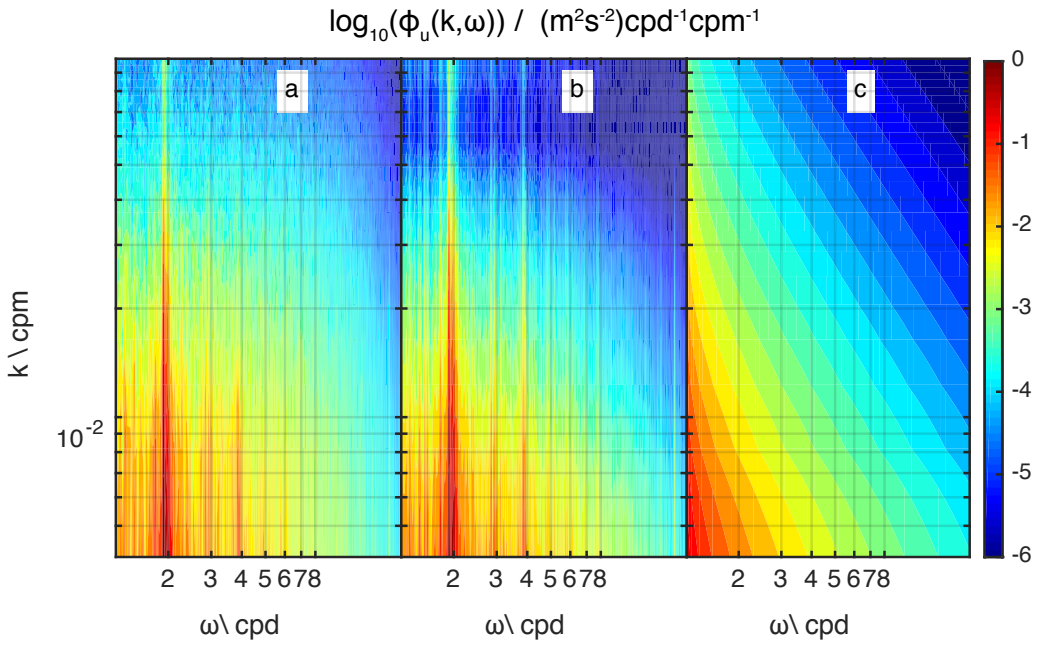

Figure 4.35: MC09 MP2 total velocity spectra a) observed, b) optimal separable, c) GM model

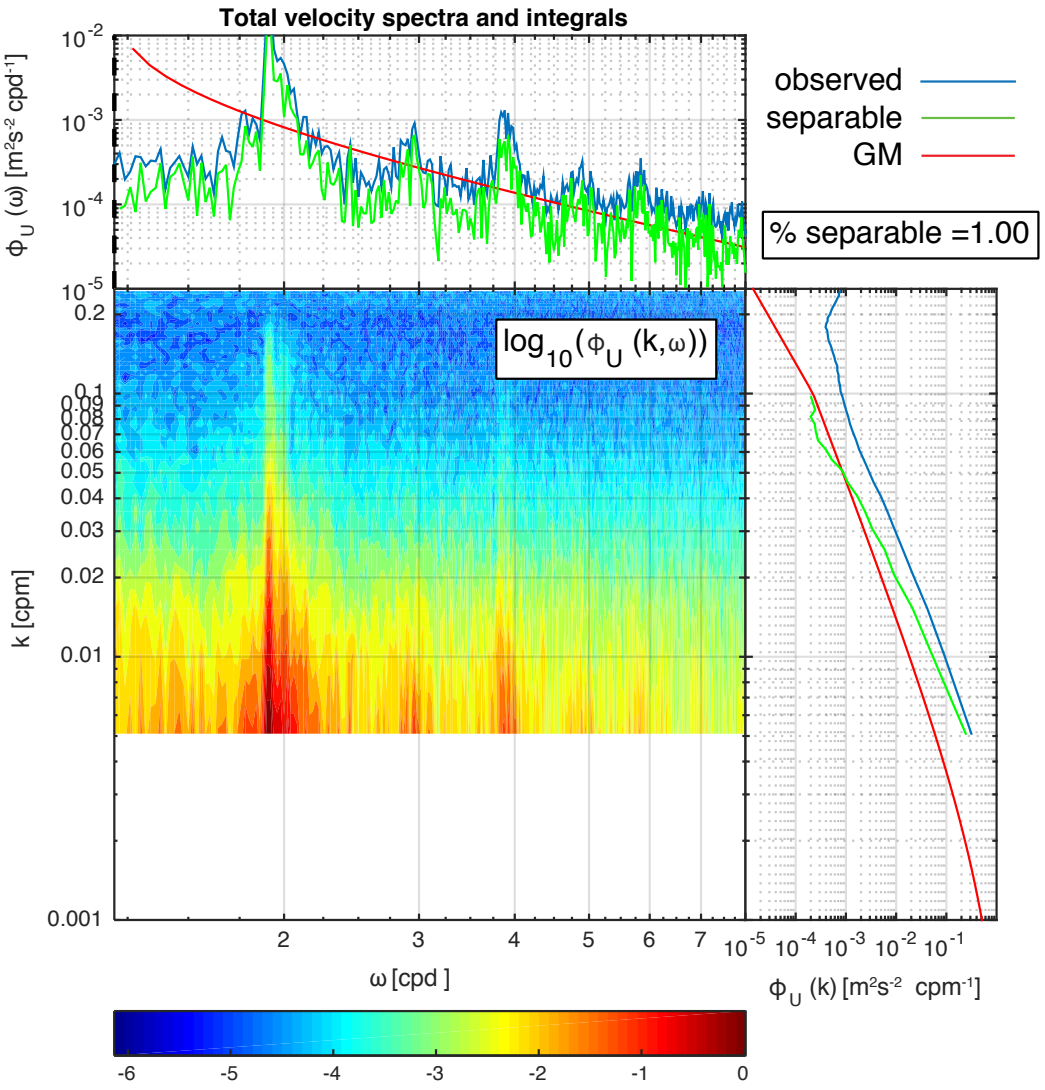

Figure 4.36: Total velocity spectrum from MC09 MP3 shown with integrated frequency spectrum and integrated wavenumber spectrum of observations and optimal separable wavenumber and frequency forms.

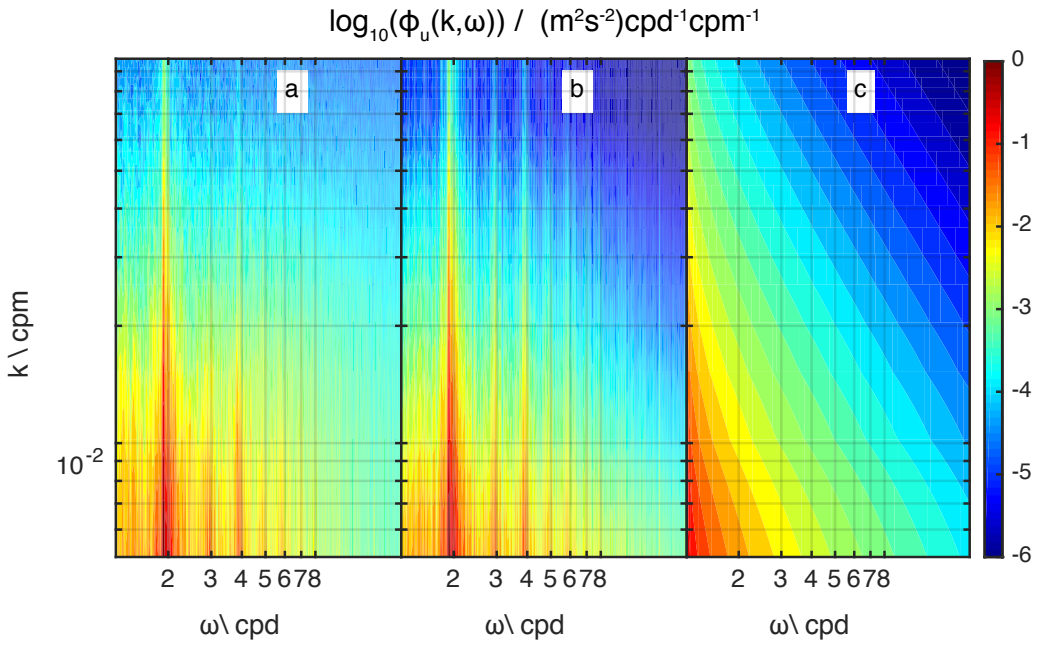

Figure 4.37: MC09 MP3 total velocity spectra a) observed, b) optimal separable, c) GM model

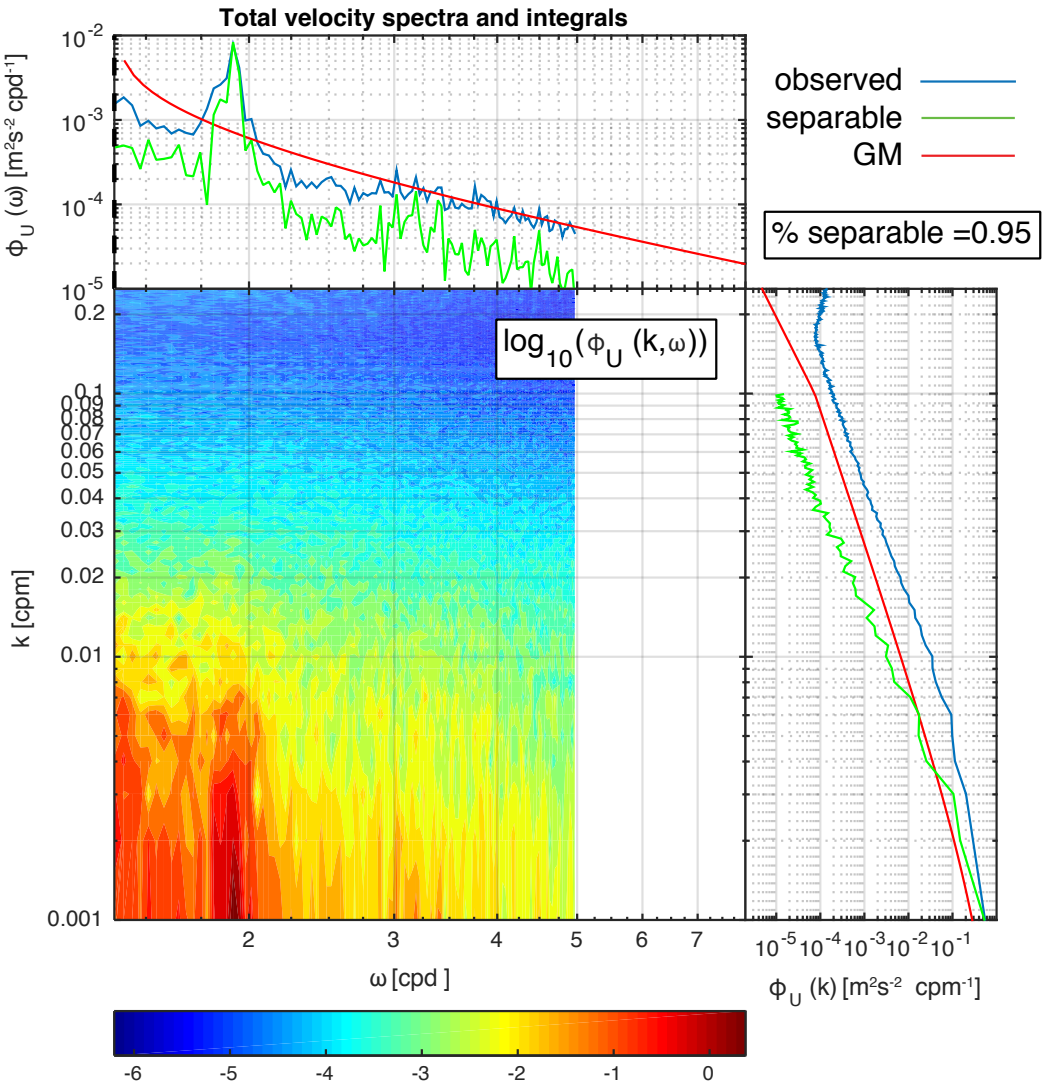

Figure 4.38: Total velocity spectrum from ORE05 MP1 shown with integrated frequency spectrum and integrated wavenumber spectrum of observations and optimal separable wavenumber and frequency forms.

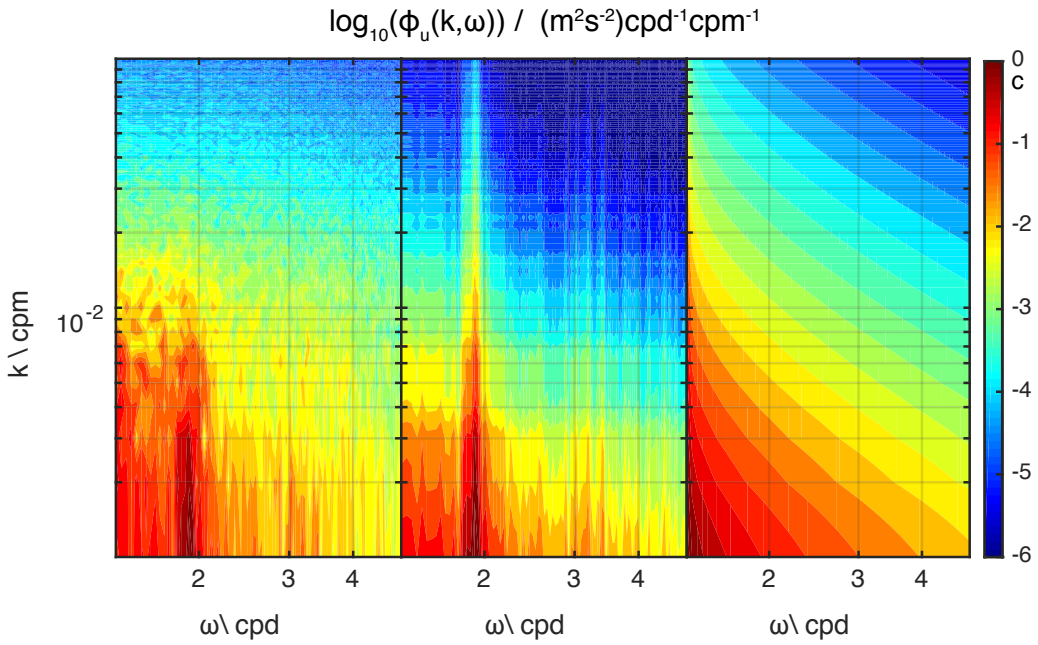

Figure 4.39: ORE05 MP1 total velocity spectra a) observed, b) optimal separable, c) GM model

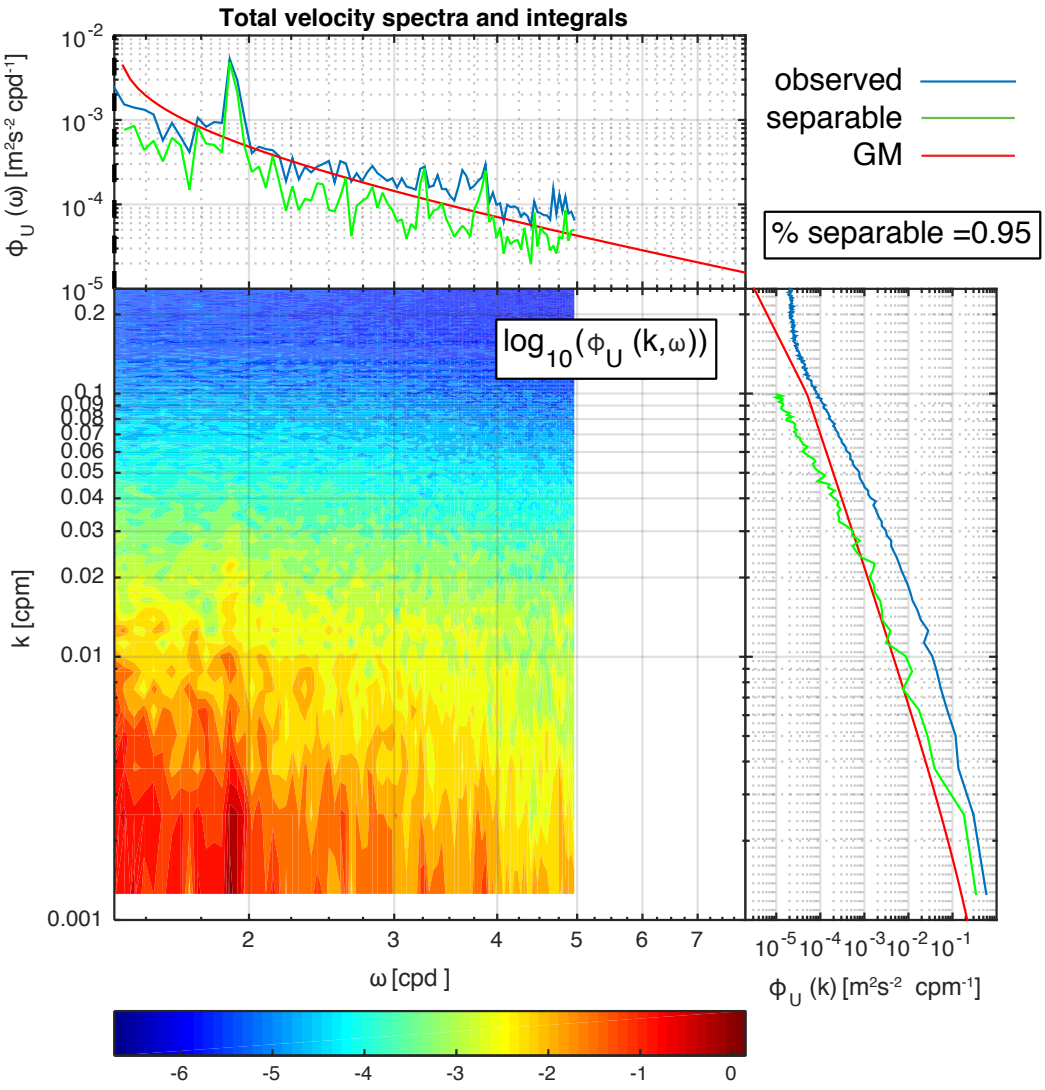

Figure 4.40: Total velocity spectrum from ORE05 MP3 shown with integrated frequency spectrum and integrated wavenumber spectrum of observations and optimal separable wavenumber and frequency forms.

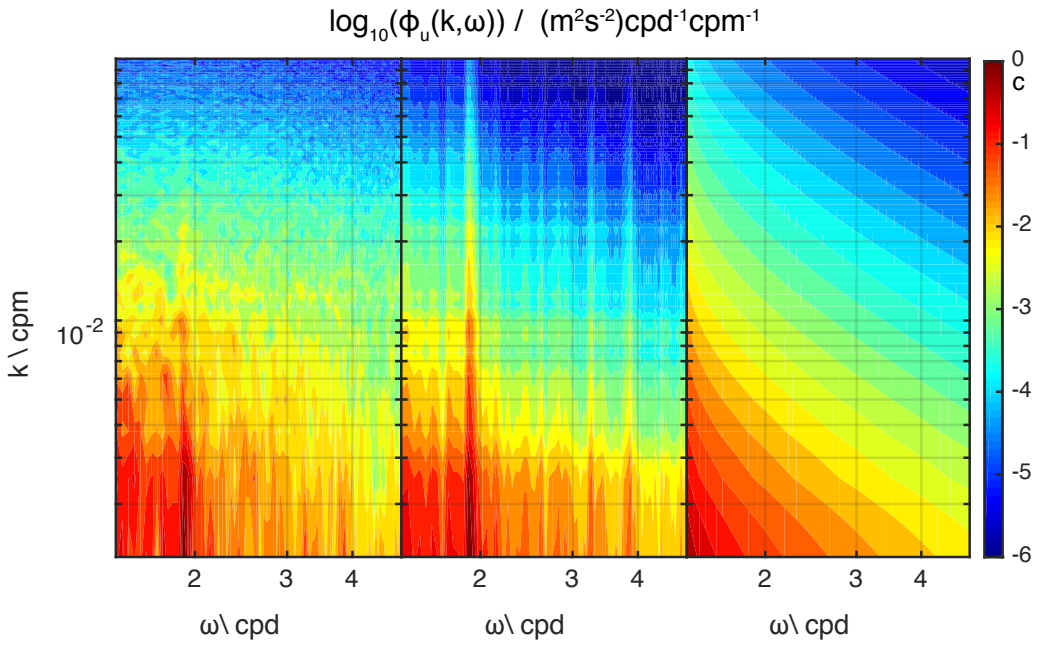

Figure 4.41: ORE05 MP3 total velocity spectra a) observed, b) optimal separable, c) GM model

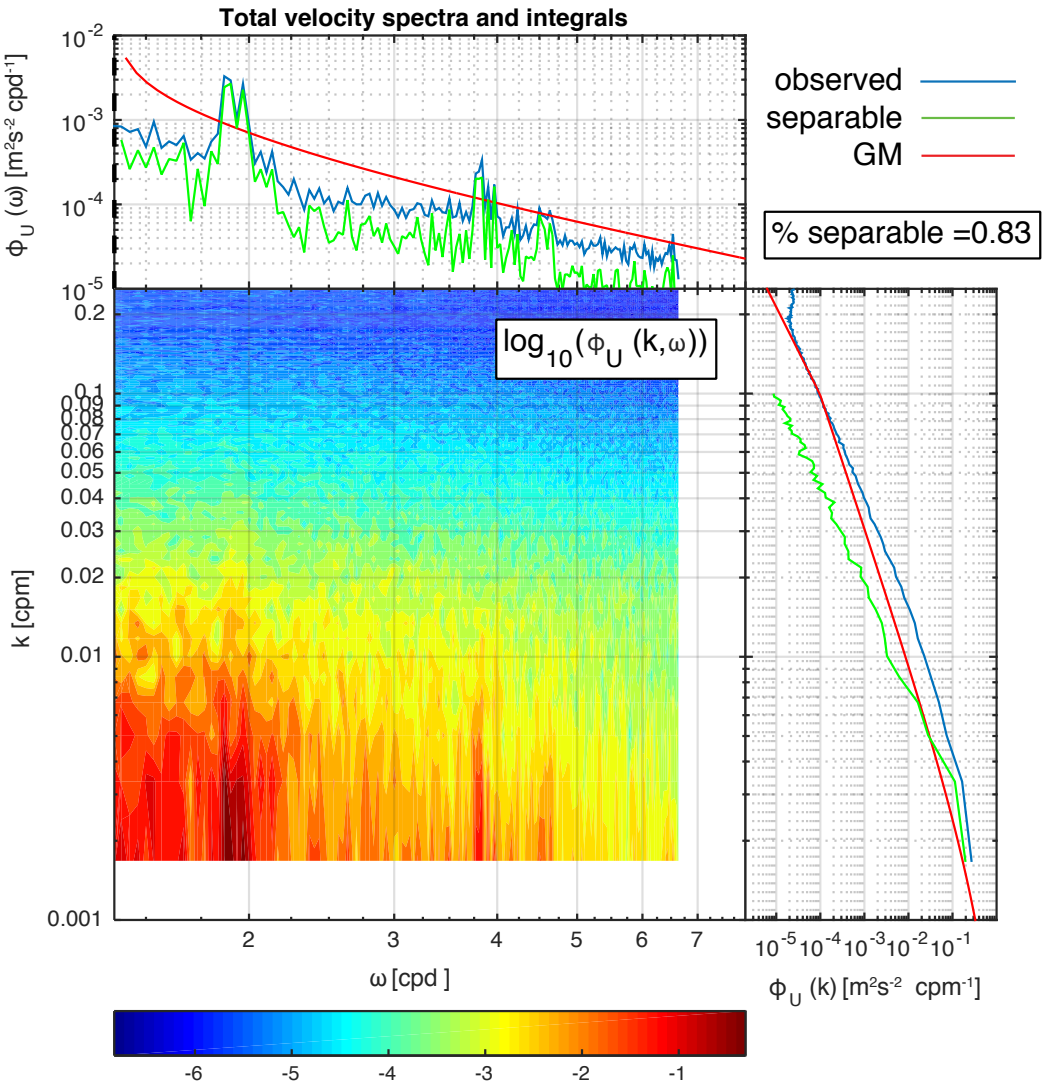

Figure 4.42: Total velocity spectrum from ORE05 MP4 shown with integrated frequency spectrum and integrated wavenumber spectrum of observations and optimal separable wavenumber and frequency forms.

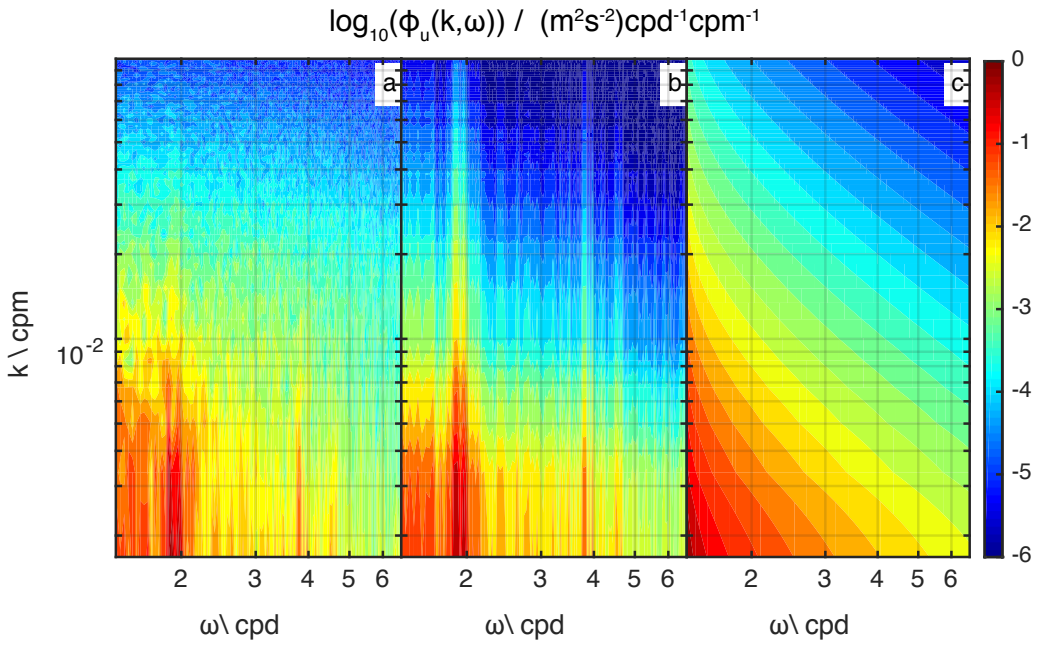

Figure 4.43: ORE05 MP4 total velocity spectra a) observed, b) optimal separable, c) GM model

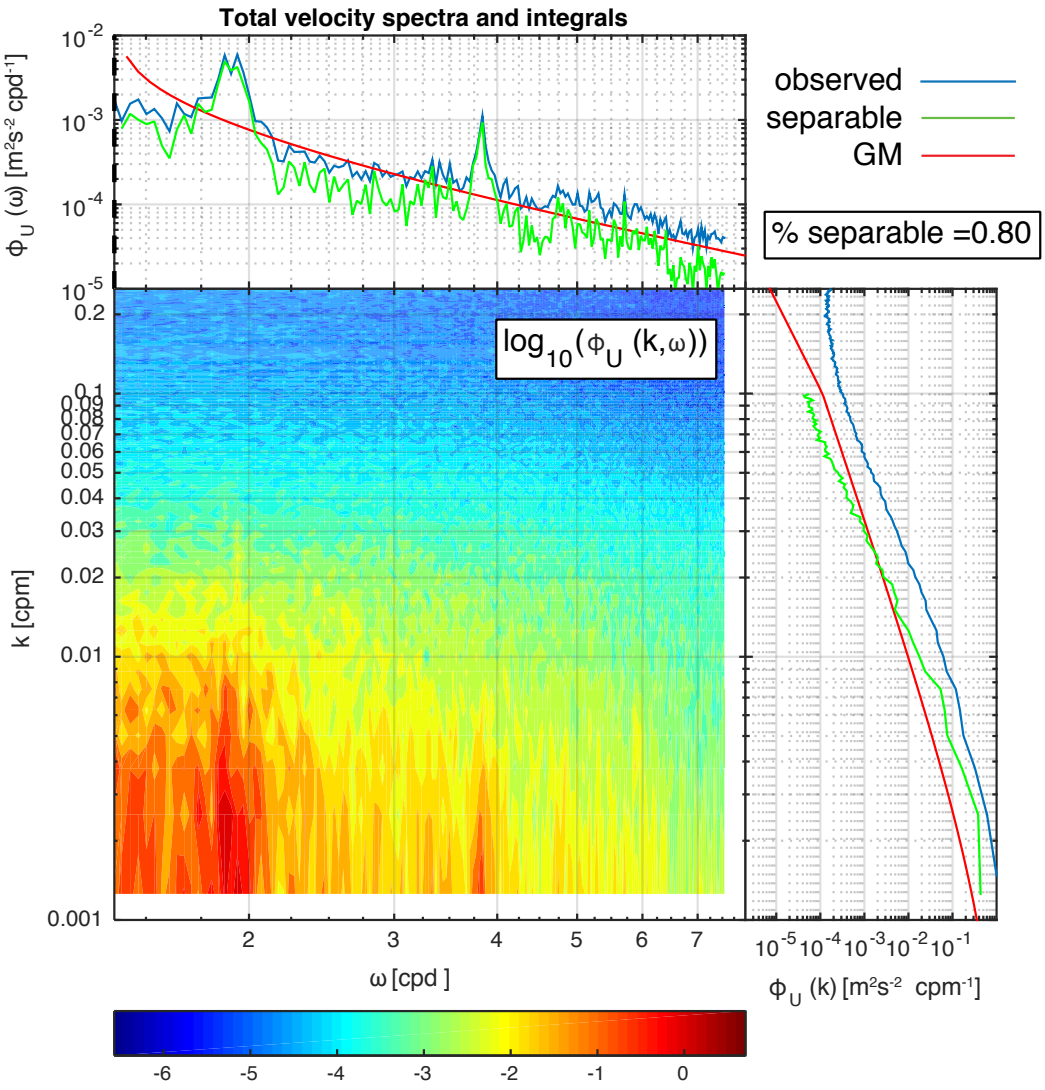

Figure 4.44: Total velocity spectrum from ORE05 MP5 shown with integrated frequency spectrum and integrated wavenumber spectrum of observations and optimal separable wavenumber and frequency forms.

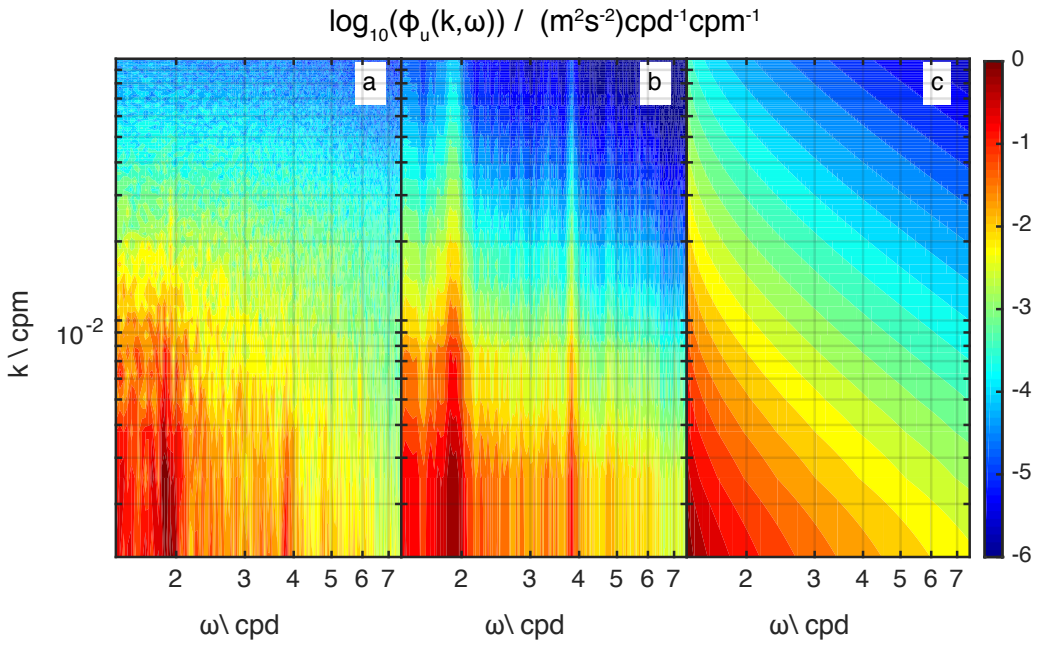

Figure 4.45: ORE05 MP5 total velocity spectra a) observed, b) optimal separable, c) GM model

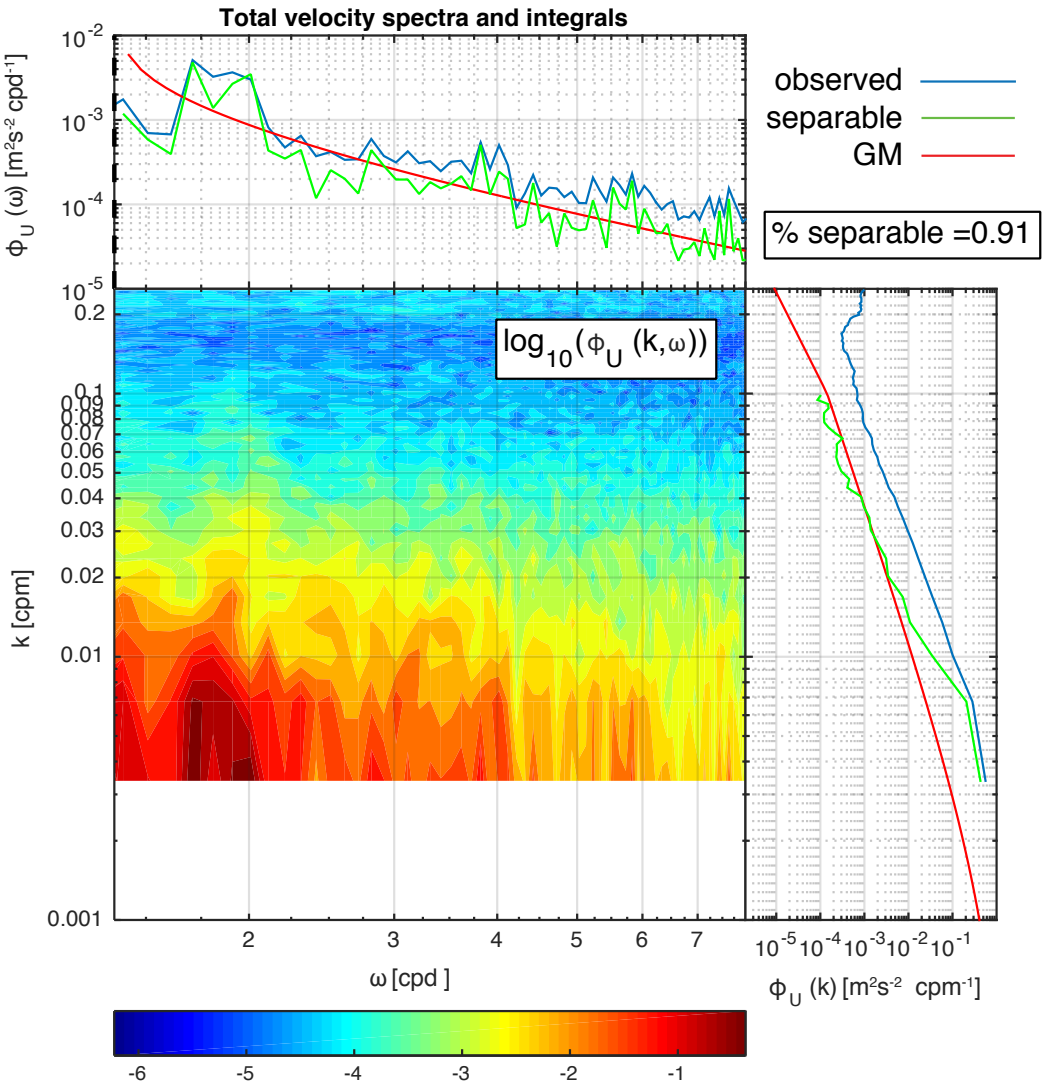

Figure 4.46: Total velocity spectrum from ORE05 MP6 shown with integrated frequency spectrum and integrated wavenumber spectrum of observations and optimal separable wavenumber and frequency forms.

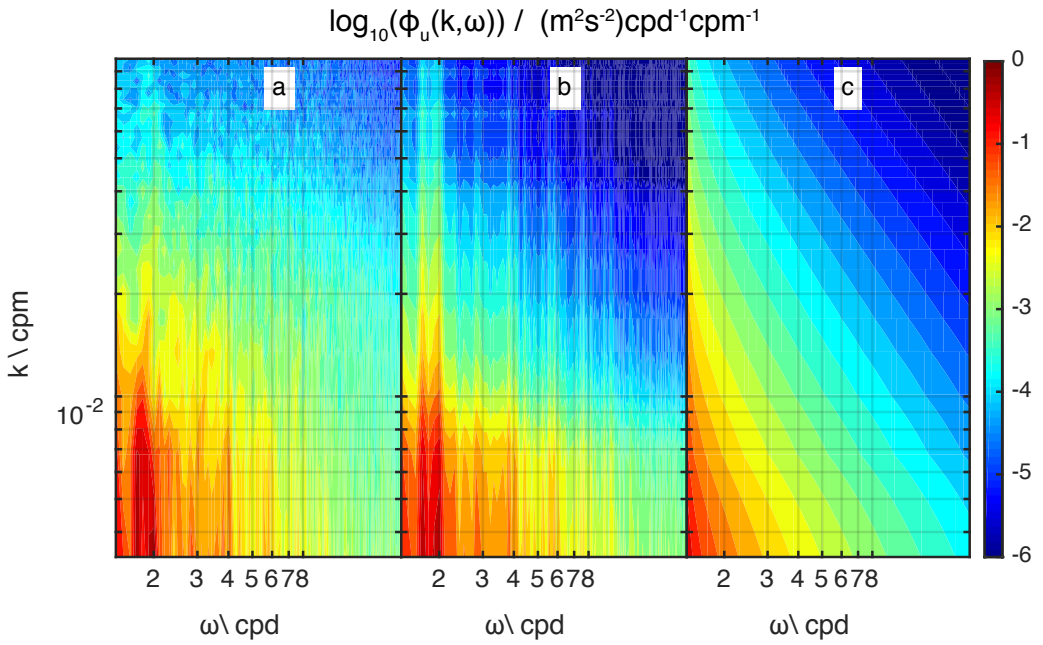

Figure 4.47: ORE05 MP6 total velocity spectra a) observed, b) optimal separable, c) GM model

Chapter 5

RESOLUTION AND SPECTRAL RESPONSE OF PROFILING INSTRUMENTATION

5.1 Introduction

Understanding the sampling characteristics of the instruments used to sample the vertical structure of oceanic variability is vital to interpreting not only estimates of parameterized diffusivity but also to how observed spectral levels relate the actual level of variance in the ocean. In order to capture both vertical and temporal variability a variety of instruments have been developed that make repeat profiles of the water column. In particular, the work here discusses the McLane Moored Profiler (MP) and the EM–APEX float.

Ideally, our instruments would be able to make instantaneous vertical profiles over any depth range making vertical lines through time and depth space. However, because profilers are limited to a finite travel speed, the instruments actually trace a sawtooth pattern (Fig. 5.1). This pattern produces uneven temporal sampling that varies as a function of depth relative to sampling range.

The irregular temporal sampling requires additional processing before a frequency spectrum can be computed. Because of this, a range of approaches exist for dealing with the resultant irregularly spaced data. One approach is to simply assume that each vertical profile is instantaneous and assign the entire profile the mean time of the profile. This is effectively assuming that the rate of change of variability is significantly less than the time it takes the instrument to complete a profile or that the spacing between profiles is much longer than the profile duration. Another approach is to interpolate the data back to a uniform time and depth grid. In both of these approaches, the exact spectral response is difficult to determine analytically. Typical approaches towards determining frequency response of a filtering oper-

ation require uniform time sampling. Though some work exists on warped transforms, their application here remains unclear.

An additional technique that is used to infer some partial information about frequency content from vertical profiles, without gridding, is to space subsequent vertical profiles by one half of the inertial period. The difference from these velocity pairs preferentially extracts variability near the inertial frequency. This technique, which we discuss in greater detail in the following sections, has been used by several investigators, yet details of the bandwidth and spectral response of this operation are not fully documented.

In the following analysis we use simulated profiling instruments in an idealized wave field to illuminate the wavenumber and frequency response of the operations needed to bring unevenly spaced data back to a uniform grid and how total variance captured is effected. Additionally, we look at the impact of assuming vertical profiles are instantaneous on resolved variance and determine the bandwidth and total spectral response of the half inertial difference filter.

5.2 Instruments discussed

We consider two specific instruments in this work, the McLane Moored Profiler, and the EM–APEX float. What follows is brief discussion of their nominal properties and deployment parameters to clarify the inherent properties of the profiling schemes to be addressed here.

5.2.1 McLane Moored Profiler

The MP is a wire crawling instrument that is equipped with a CTD and a velocimeter that provides records of salinity, temperature, pressure, and east (u) and north (v) velocity. The MP traverses the wire with a mean speed of $25 - 35$ cm s^{-1} and can provide 2-m vertical resolution and on average 1.5-hr spacing between samples, though this varies as a function of depth and profiling ranges. Previous calculations have shown that frequency and wavenumber content can be resolved, without contacting the instrument noise floor, out to a vertical wavenumber of $k_z \approx 0.10$ cycles per meter (cpm) and to a frequency of $\sigma \approx 10$

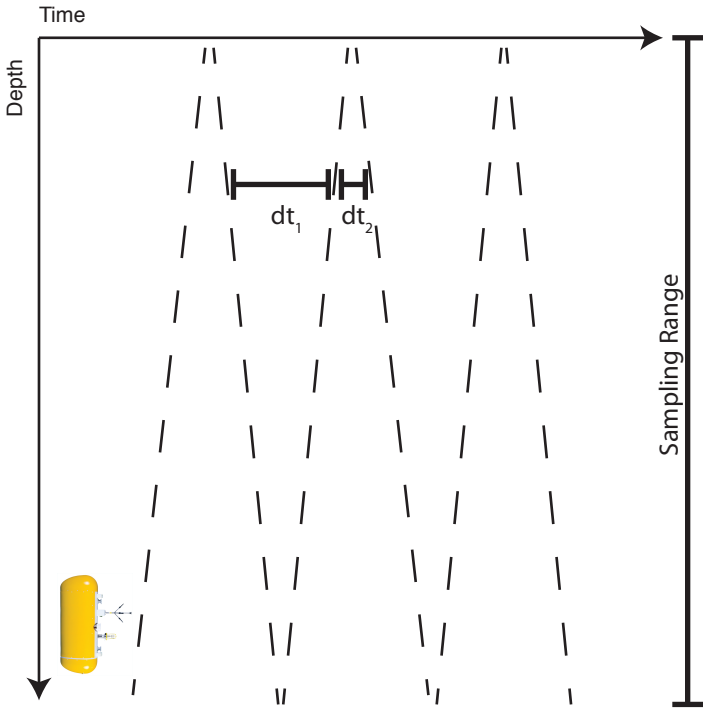

Figure 5.1: Schematic profiling pattern used by a MP.

cycles per day (cpd).

Schematically, the profiles from an MP are shown in figure 5.1. Typically, the moored profiler pauses briefly at both the top and bottom of its profile though its deployment parameters can be set as desired

We investigate three separate properties of this profiling shape. One, the effectiveness of assuming a vertical profile is instantaneous is dependent on the profiling speed of the instrument. In order to evaluate the impact of profiling speed we run simulated MPs through an idealized wave field at varying speeds. This allows us to not only evaluate how well the instrument does at capturing variability, but also determine if perhaps it can profile slower without loss of resolution.

Two, because the spectral response of gridding unevenly sampled data remains un–clear, we examine spectra from various profiler speeds and compare spectra of the gridded data to

the input spectrum. This analysis is carried out in both frequency and wavenumber because the impact of this operation will be different in each dimension.

Three, since the spacing between subsequent data samples varies as a function of depth relative to sampled range, we examine the frequency response of the interpolation process at varying depths and map the effect of this response.

5.2.2 EM-APEX

EM-APEX floats are a descendent of the profiling floats used in the global Argo array and have additional electromagnetic sensors accompanying the usual set of conductivity, temperature, and depth sensors. These additional sensors allow the float to measure horizontal velocity. Horizontal velocity is estimated by measuring the electric current produced by seawater moving through the earth's magnetic field. Details of the post processing methods used to convert this current to velocity are documented in Sanford et al. [2005]. The floats have a typical lifespan of about 300 vertical profiles at an effective vertical resolution of 2–3m.

In addition to the typical evenly temporally spaced profiles, periodic rapid bursts of profiles are sometimes used. This is shown schematically in figure 5.2. By spacing the ascending profiles in the burst at half an inertial period apart it is possible to isolate near inertial variability by computing eastward inertial velocity (u_i) and northward inertial velocity (v_i) [Kilbourne and Girton, 2015] as

$$u_I(z) = \frac{u_2(z) - u_1(z)}{2} \quad \text{and} \quad v_I(z) = \frac{v_2(z) - v_1(z)}{2}. \tag{5.1}$$

While this operation does isolate near inertial variability, it also aliases in all odd multiples of the inertial frequency. In a typical red velocity spectrum, the impact of aliasing in variance at these higher odd multiples of f is minimal. However, when these odd multiples of f are near to the diurnal or semidiurnal frequency, or inertial $\pm$ tidal frequencies as is produced by kinematic heaving [Alford, 2001], the impact may be significant. Additionally, the operation

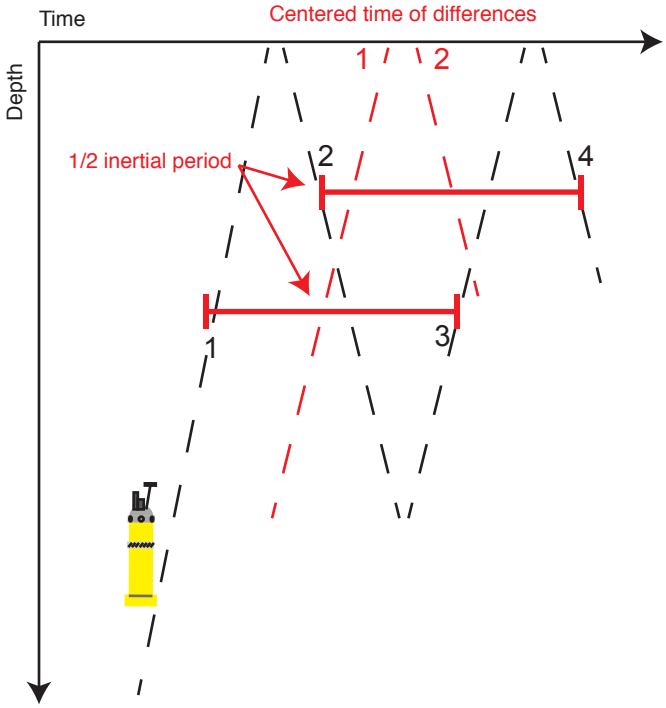

Figure 5.2: Schematic profiling pattern and half inertial differences from an EM-apex float.

is not simply a dirac comb in frequency space. The half inertial difference has some bandwidth that has a varying effect that changes with respect to distance in frequency space from f or the nearest odd multiple of f. In the following sections we investigate the impact of half inertial differencing and the bandwidth of the half inertial difference filter.

5.3 Methodology

In the following section we outline the methods used in testing the response of the previously described processing operations. The methodology used here makes use of a uniform GM wavefield and a field with a single wave whose phase, amplitude, frequency, and vertical wavenumber are specified explicitly.

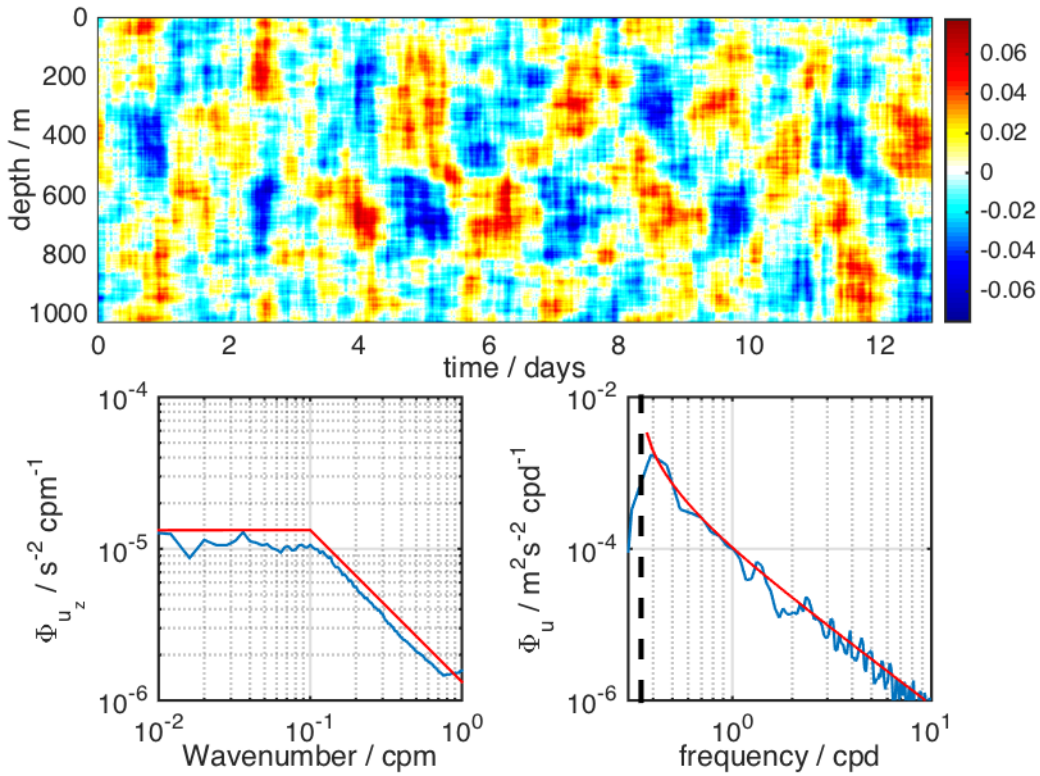

Figure 5.3: a) GM time depth map of velocity. b) Computed wavenumber spectrum of shear and the GM spectrum of shear that was inverted to produce the input field. c) Computed frequency spectrum of velocity and the GM velocity spectrum that was inverted to produce the input field.

5.3.1 GM field

In order to evaluate the impact of the processing techniques used with the MP and the EM-APEX floats, multiple realizations of virtual instruments profiling in an idealized wavefield are created. This wavefield is constructed to have an exactly GM spectral shape in frequency and wavenumber. A GM velocity field is produced by taking the inverse Fourier transform of a GM wavenumber frequency spectrum. Each wave in the input spectrum is assigned a random phase before doing the inverse. An example time depth map, frequency spectrum of velocity, and wavenumber spectrum of shear are shown in Fig. 5.3

Resolution and length of the time depth field are controlled by the resolution and Nyquist

frequency of the input spectrum. In the following work we use a time depth field that has a vertical resolution of 0.5 m and a temporal resolution of 9 minutes. This resolution allows us to build arbitrary profiles through the field while reducing the distance to a data point thereby minimizing the impact of the interpolation.

Single wave

In addition to the GM wave field, we make use of single wave fields. By specifying the frequency, vertical wavenumber, and phase explicitly, we can step through various properties and look at the influence of incrementing their values. This is of particular value for mapping out the frequency response of the processing operations. It allows us to isolate the response to the impact of only a single variable.

5.4 Results

5.4.1 McLane

The virtual MP was profiled through our GM wave field at a set of profiling speeds ranging from 0.01 m/s up to 0.35 m/s. The profiler was allowed to profile non stop over a period of ten days. The set of profiles was then linearly interpolated back to a uniform grid with a 2 m vertical resolution and a 1.5 hour temporal resolution.

Shear spectral variance

As an example to illustrate the effects of gridding and assuming profiles are instantaneous, virtual profilers were made to sample 1000m of water at 10°N. A vertical wavenumber spectrum of shear was computed from each profile, assuming they were instantaneous, and each gridded profile. The mean shear spectrum of the profiles and the gridded data were then computed as the average of all the profile spectra. Variance was computed by integrating the mean spectrum and then expressed as the percent variance relative to the input GM spectrum of shear integrated over the same wavenumber range. The results of this computation

are shown in Fig. 5.4.

The gridded data reaches a peak at 95% of the GM variance at a velocity of 0.3 m/s that decreases rapidly as the profiling speed slows. The mean shear spectrum computed from the instantaneous profiles show a small peak at 0.3 m/s, but overall, changes minimally over the entire range of profiling speeds. The typical MP profiling speed of 0.25 m/s captures 93 percent of the variance of the input field. This analysis illustrates that there is a critical speed that the instrument needs to profile above. At speeds slower than $\approx$ 0.15 m/s percent variance drops off dramatically though this will depend on profiling range and latitude.

We perform a similar computation but make use of only the down casts to show the

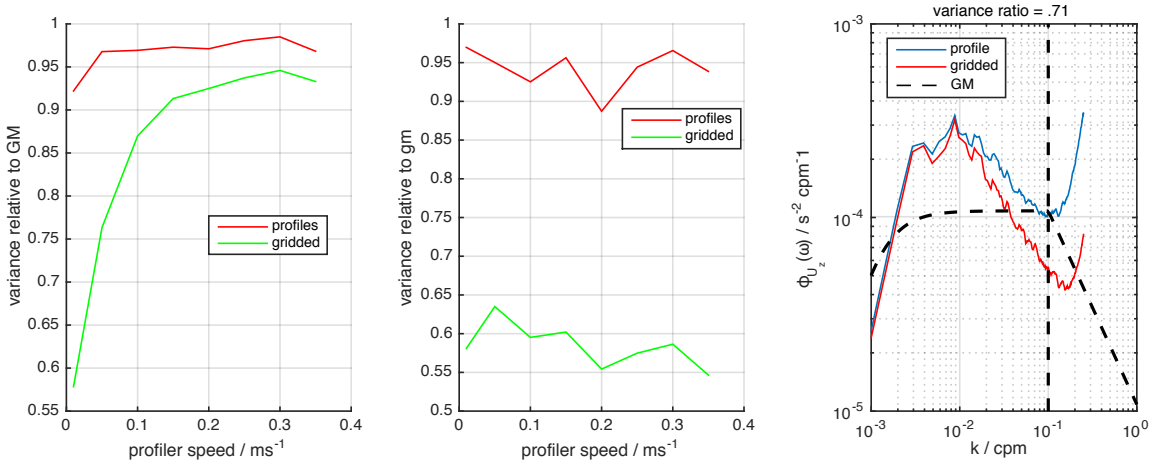

Figure 5.4: An example of the effect of gridding data and assuming profiles are instantaneous. Profilers are sampling 1000m of water, the field is set at 10°N, and the profiles are gridded back to a 2 m 1.5 h grid. a) Variance captured relative to the GM input spectrum as a function of profiler speed based on shear spectrum with a sawtooth pattern. Results shown for both assuming each profile is instantaneous and re–gridding back to a 1.5 hour uniform time grid. b) Variance captured relative to the GM input spectrum as a function of profiler speed based on shear spectrum with only down profiles. Results shown for both assuming each profile is instantaneous and re–gridding back to a 1.5 hour uniform time grid. c) Example spectra from IWAP MP1 showing the difference in wavenumber spectrum of shear computed from profiles vs gridded data as well as variance captured in profiles vs gridded. Note this is not the exact same quantity plotted in panels a and b where the ratio is relative to variance in the actual input field.

improvements that can be had in terms of resolved variance in a sawtooth profiling scheme despite the effects of gridding (Fig. 5.4b). In this example, gridded data from only downcasts shows effectively no dependence of variance resolved on profiler speed with a significant reduction in variance resolved as compared to including the up casts.

With a GM input field sampled by a virtual MP, spectral level is reduced uniformly over all wavenumbers. Vertical wavenumber spectra of shear computed from profiles and gridded data from actual observations, however, are not attenuated uniformly at all wavenumbers. Comparisons of profile and gridded shear spectra from IWAP MP1 (Fig 5.4c) show greater reduction in spectral level at high wavenumber than at low wavenumber. Integrating up to $k = 0.1$ cpm, the gridded spectra have 71% of the variance of the profile spectra. This is a greater reduction in variance than is predicted by our synthetic profilers, which at 25 cm/s, show a profile to gridded variance ratio of $\approx 95\%$.

The lack of change in percent shear variance captured from the profile data as a function of profiler speed is not surprising as the input GM wavefield is completely homogenous in time and depth. Effectively, it doesn't matter how one traverses this wave field with respect to the instruments capability to capture shear.

Because the GM wavefields lowest energetic frequency is the inertial frequency, the lower frequency limit of the wavefield changes as a function of latitude. This changes the distribution of variance in frequency space and means that gridding the vertical profiles will likely have a different impact at each latitude. To diagnose this, GM wavefields are generated from 10 to 80 °N in 10 degree increments. A similar calculation is then done for each wavefield with results now shown as a function of both latitude and profiler speed (Fig. 5.6)a,b. Again, the profilers here are sampling over 1000m of water.

Curves showing the latitude dependence for each profiling speed reveal that variance captured at a given profiler speed is linearly dependent on latitude and that as latitude increases the minimum profiler speed required to capture a constant level of variance increases.

This linear dependence could have a significant impact when comparing mixing estimates from moored profilers at different latitudes computed using shear based fine scale parameter-

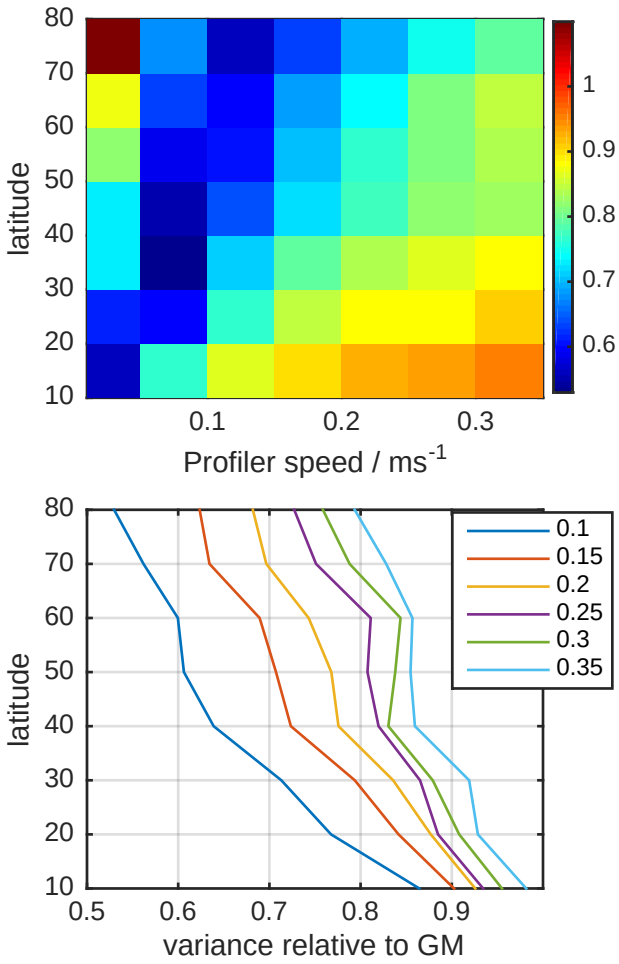

Figure 5.5: Variance relative to GM as a function of latitude and profiler speed for 1000m sampling

izations. The parameterizations have a built in latitudinal dependence that decreases mixing at low latitudes to match observed values. However, the latitudinal dependence in variance resolved by the MP will act to counteract part of the latitudinal dependence of the parameterizations. This effect would make comparisons of parameterized diffusivity at different latitudes, and in particular comparisons between different instruments at different latitudes

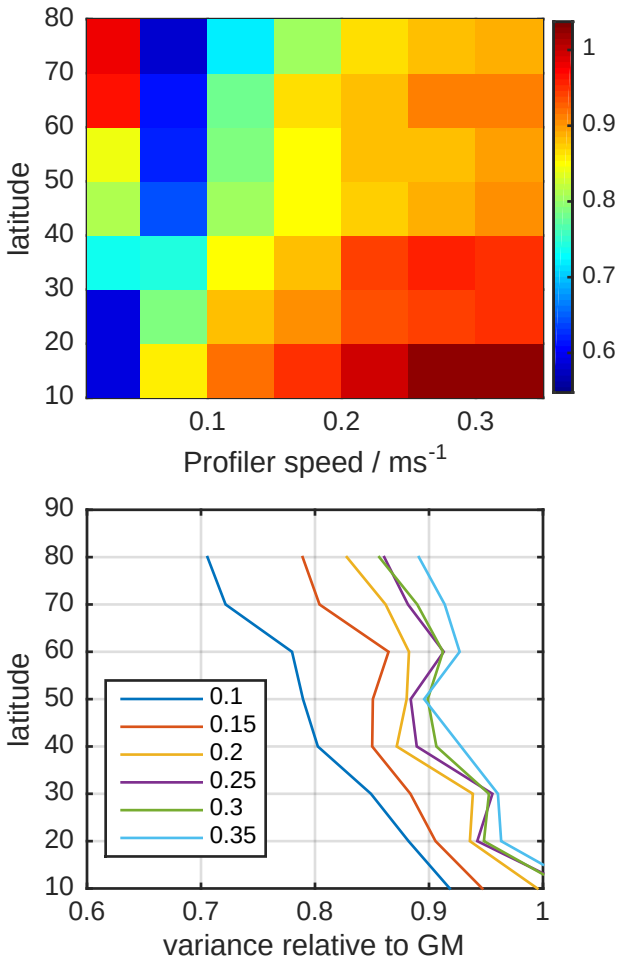

Figure 5.6: Variance relative to GM as a function of latitude and profiler speed for 500m sampling

difficult. E.g. shear estimates from an ADCP will have a different latitudinal dependence of variance resolved than MPs.

Because this result is likely to depend on the profiler range, we can compute the same quantity but instead profile over 500m (Fig. 5.6). We see similar patterns between Fig. 5.4 and Fig. 5.6, however more variance is resolved when profiling over only 500m. We

can collapse these results from 1000m and 500m of profiling range to a common variable by expressing the variance resolved not as a function of profiler speed, but as a function of the mean time between a down and an up profile (δT_{mean}). This is the same as the time between data points at the mid depth point of the profiling range. In these two examples, this normalization should mean that the .1m/s profiler, profiling over 500m, should produce the same result as the .2m/s profiler, profiling over 1000m. Examination of figures 5.4 and 5.6, reveals that this is true.

Because each curve of variance vs latitude is nearly linear, we approximate each curve as explicitly linear, and form a plane which gives variance relative to GM, as a function of latitude and δT_{mean}.

If a set of 3 dimensional points lie exactly on a plane, the unknown coefficients of the functional form of that plane

$$ax + by + cz + d = 0 \tag{5.2}$$

can be found by calculating the null space of the matrix $A = [x, y, z, 1]$ as that null space maps A to zero.

Because our set of linear fits only roughly defines a plane, we can search for the optimal plane using a similar technique. However, since our points do not lie exactly on a single plane, we need to find the plane that minimizes the error relative to our observations. We can do this by finding the nearest approximation to a null space of our matrix A by looking at the right singular vector (V) of the singular value decomposition of A ($A = U\Sigma V^t$) corresponding to the smallest singular value. Solving for the unknown coefficients of this optimal plane in this way yields a function for the variance resolved

$$Z = \frac{-(.7370 + .0019X + .0767Y)}{-.6715} \tag{5.3}$$

where Z is variance resolved, X = latitude (degrees), and Y = δT_{mean} (hours). The root

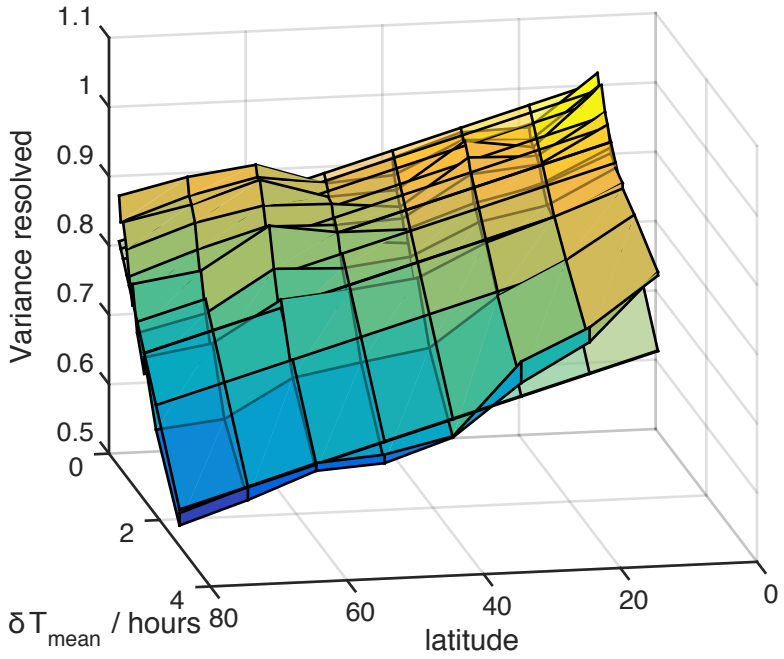

Figure 5.7: Variance resolved as a function of latitude and δT_{mean}. Solid surface shows linear fits to observed structure in variance resolved vs δT_{mean}. Transparent surface shows best fit to the observed structure given in (5.3). Root mean square deviation of this fit from the observed is 0.0322.

mean square deviation of this planar fit is 0.0322. The plane defined by this method is shown in Fig. 5.7 along side the linear fits to each simulation.

The dependence on δT_{mean} and latitude is well represented by this linear function. With this fit, we can predict approximately how much variance an MP would resolve given latitude and profiling parameters while profiling through a GM wave field. Though narrow band frequency peaks in the actual oceanic wave field will create deviations from this approximation, it serves as a good first order approximation that can be used in design of future experiments.

Velocity spectral variance

A similar comparison looking at percent variance captured relative to the input field can be performed using depth averaged frequency spectrum from the gridded profiles. Because of the uneven temporal sampling pattern produced by the sawtooth profiling, a similar comparison cannot be made on the profiles directly. Profiling through 1000m of water at 10°N, variance captured relative to GM computed from the velocity spectra reveals a similar pattern to what was observed in shear (Fig. 5.8). At speeds above 0.15 m/s there is little change in resolved variance, but below 0.15 m/s it declines rapidly. Peak values of variance relative to GM are $\approx 90\%$. Unfortunately, because we cannot determine frequency content captured by the profiles directly we cannot discern how much of the loss of variance is due to the sampling pattern or from the gridding process.

Similarly to what was done for shear variance, we can repeat these calculations to determine the latitudinal dependence of variance resolved in a frequency spectrum. We use the same set of profiling parameters as before taking our sampling depth range to be 1000m, varying velocity from 0.01 to .3 m/s, and varying latitude from 10 to 80 degrees °N.

Mean frequency spectra for each profiling speed reveal subtle differences in attenuation that were not observed in shear (Fig 5.10). The spectral attenuation as a function of profiling speed is also a function of frequency. There is significantly less reduction in spectral levels at near inertial frequencies than near the Nyquist. Excluding the spectrum from 0.01 m/s, near the inertial frequency we have a reduction of only a factor of 2-3 while near the Nyquist frequency the reduction exceeds an order of magnitude.

Previous analysis of the frequency spectra have been based on depth averaged spectra. There is, however, vertical structure in the resolved variance because the spacing of measurements changes as a function of depth. Observed spectral variance relative to GM plotted vs depth reveals a uniform background level with a significant increase in resolved variance at ≈ 500 m (Fig. 5.11).

This peak of elevated variance resolved coincides roughly with the depth at which the

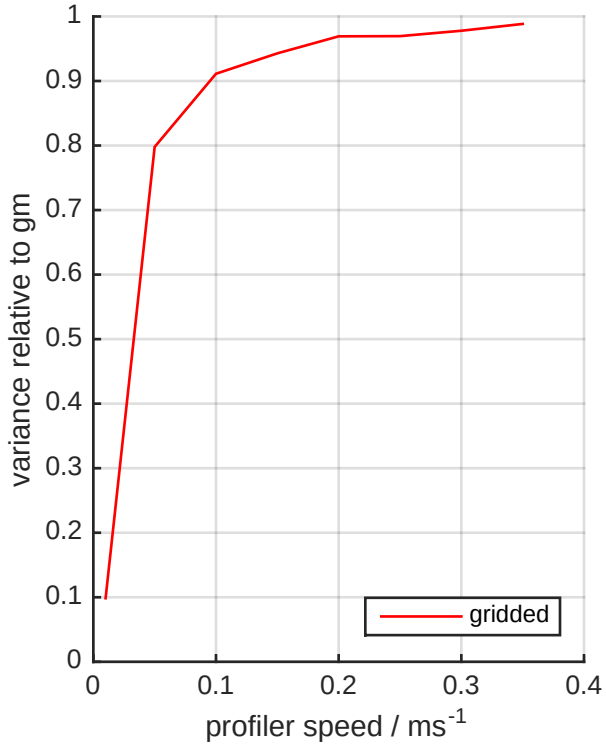

Figure 5.8: Example calculation showing effect of gridding on percent of velocity variance captured relative to the GM input spectrum as a function of profiler speed estimated from the frequency spectrum produced from the re–gridded MP data. Virtual profiler is sampling 1000 m of water, data is gridded to 2 m and 1.5 h, and the wavefield is at 10 °N.

actual temporal spacing of the sloping profiles is approximately 1.5 hours.

5.4.2 EM-APEX

With the EM–APEX floats, we are particularly interested in evaluating the effectiveness of the half inertial difference filter at isolating near–inertial variability. To focus on this question, we perform a series of sequential down profiles through the GM velocity field, separated by half the inertial period. From each profile pair, we compute the half inertial differences (as described in section 5.2.2) and calculate a vertical wavenumber spectrum of shear. The time mean spectrum from the profiles themselves captures 95% of the input

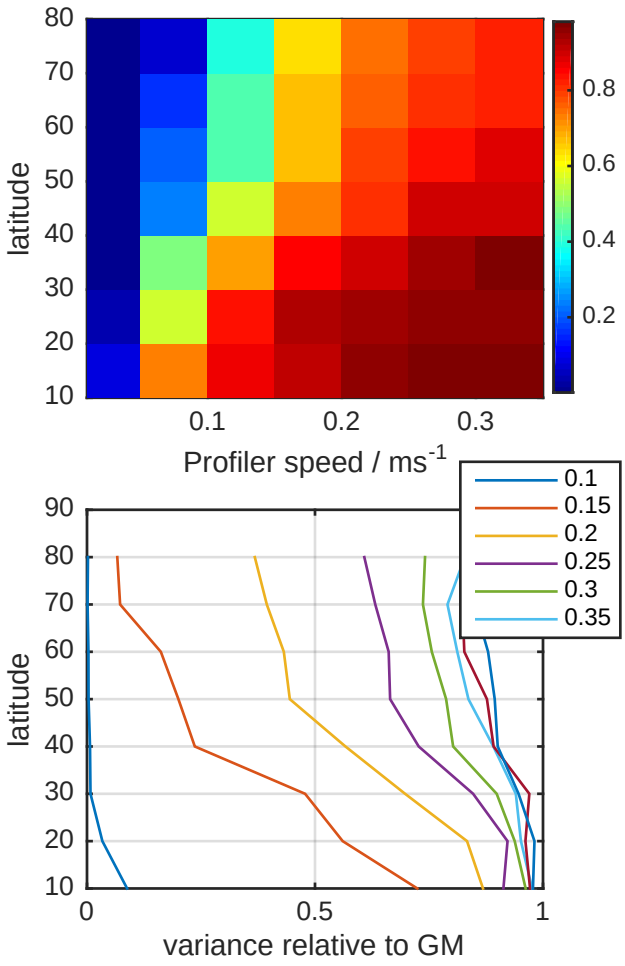

Figure 5.9: Ratio of variance relative to GM as a function latitude and profiler speed for 1000m of water sampled

variance while the half inertial differences only captures 62% (Fig. 5.12). As expected, the half inertial difference has captured only a subset of the variability of the input field.

By taking the GM wavenumber frequency spectrum of shear and integrating across varying ranges of frequency, the bandwidth ($\delta\omega$) around the inertial frequency ($f \times [1, 1 + \delta\omega]$), that corresponds to the percent variance captured by the half inertial difference filter can

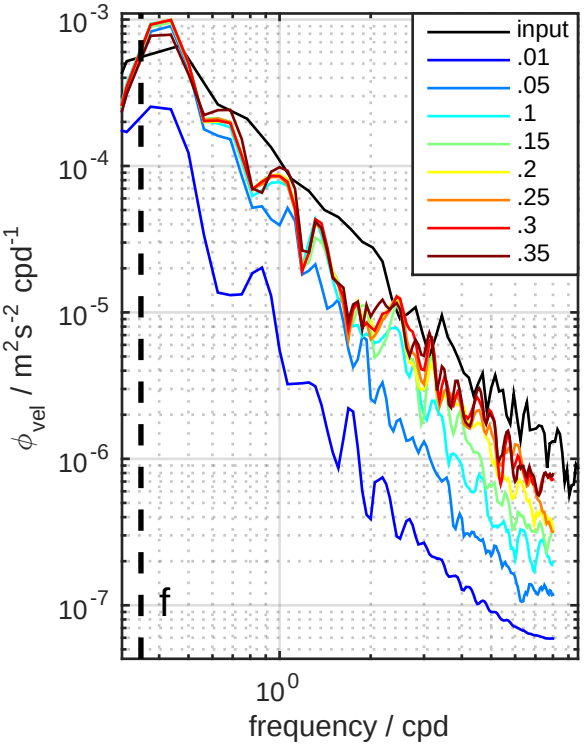

Figure 5.10: Velocity spectrum shown as a function of profiler speed in m/s illustrating that the attenuation in variance resolved is occurs only at higher frequencies. At all profiling speeds except 0.01m/s the magnitude of the inertial peak remains uniform to within error bars. At higher frequencies up to 15 cpd, however, we see attenuation of more than an order of magnitude over the range of profiling speeds.

be computed (Fig. 5.13). Considering only frequencies near f, a $\delta\omega = 0.42$ is required to produce the same level of variance that was captured by the half inertial difference. However, since the half inertial difference also aliases in all variability at odd multiples of the inertial frequency, we also calculate the $\delta\omega$, that when integrated across all odd multiples of f, $N \times f \times [1, 1+\delta\omega]$ where $N = [2n-1] \; \forall \; [n \in \mathbb{N}]$, produces the same variance. For the GM spectrum used in this computation, that corresponds to a $\delta\omega = 0.28$. Despite the redness of the velocity spectrum, and therefore the large decreases in power at higher frequencies, the addition of higher odd multiples of f reduces the required bandwidth by 33%.

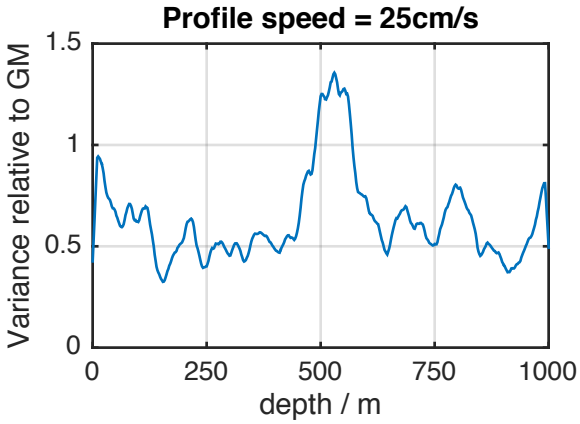

Figure 5.11: Ratio of variance relative to GM as a function of depth

Determining the exact bandwidth this way is difficult because the GM spectrum rapidly increases as ω approaches f. Because of this, the frequency resolution of the spectra, and thereby how close to f the frequency actually gets, can have a large impact on the computed variance. To map the bandwidth out more explicitly, instead of using a GM wave field, synthetic EM–APEX profilers were made to profile through a wave field consisting of a single wave with a prescribed amplitude, frequency and vertical wavenumber. The attenuation of each spectral peak was calculated as

$$A(\omega/f) = \frac{\Phi(k,\omega)_{halfinertial}}{\Phi(k,\omega)_{input}}. \tag{5.4}$$

By profiling through a range of waves with varying frequencies the frequency response, $A(\omega/f)$, can be determined (Fig. 5.14). As expected, frequency peaks at all even multiples of f are attenuated completely. However, the attenuation quickly lessens as one moves away from those frequencies. Peaks at odd multiples of the inertial frequency are not attenuated at all and at $\pm 30\%$ of the odd multiple frequencies, nearly 80% of the peak remains. The breadth of this band means that there is a high probability that energetic frequencies above f may be significantly aliased into the half inertial difference estimate of near inertial variability.

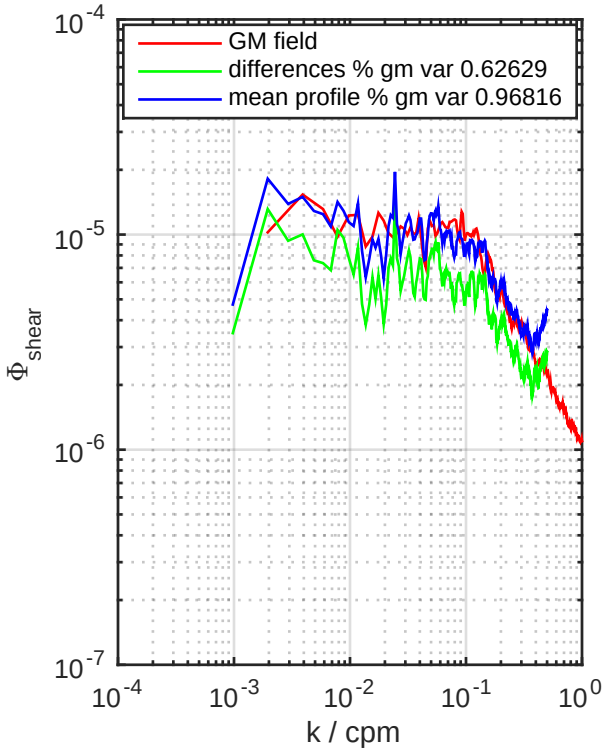

Figure 5.12: Wavenumber spectrum of shear computed from synthetic EM–APEX profiles and half inertial difference pairs along with GM input spectrum. Shows that assuming vertical profiles from an EM–APEX float profiling at 10cm/s are synoptic reproduces the input spectrum at a 96 % level. The half inertial difference pairs produce a spectrum that is only 33% of the original input.

$A(\omega/f)$ can be represented as a sin wave with an root mean square deviation from the computed values of attenuation of $RMSD = 0.0034$. This wave takes the form

$$A(\omega/f) = \frac{1}{2}\left(1 + cos(\pi * (\frac{\omega}{f} - 1))\right) \tag{5.5}$$

The frequency response of the half inertial difference operation can be used to estimate the output spectrum from the input spectrum. If we assume a GM frequency spectrum ($GM(\omega)$), we can compute the output frequency spectrum from the half inertial difference filter as $\Phi_i = A(\omega) \times GM(\omega)$ (Fig. 5.15).

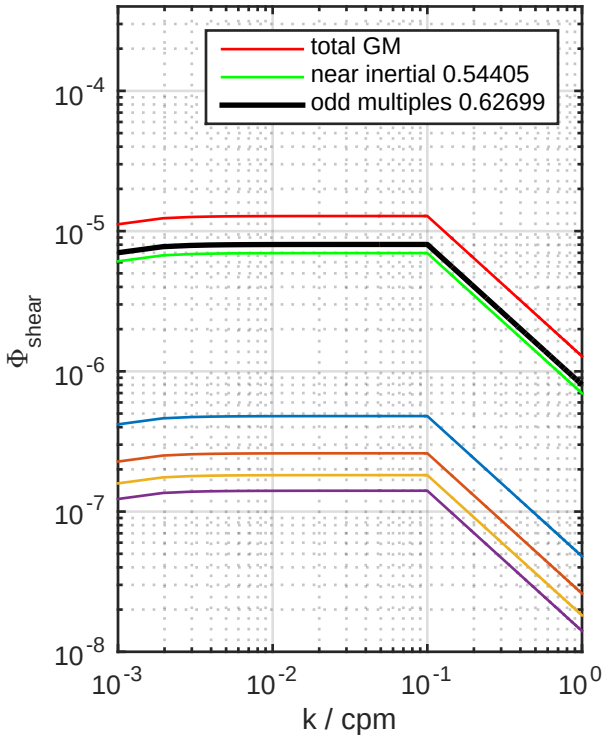

Figure 5.13: Vertical wavenumber spectra of shear showing GM spectrum as well as inertial band spectrum only, and inertial band and plus odd multiples of the inertial frequency. Spectra are averaged over a ω to 1.28ω band. Shows that with a GM input spectrum, a 28 percent bandwidth around the inertial frequency and odd multiples produces similar results to the attenuation observed in synthetic EM-apex profiles.

Any frequency greater than f can potentially be aliased into the half inertial estimate. Because of this, strong narrowband peaks, that are not represented by the GM spectrum, can seriously bias the near inertial estimate. These include phenomenon such as internal tides and their harmonics as well as variability produced by the kinematic interactions between near inertial motions and internal tides. Latitude bands where at least 80% of the diurnal and semidiurnal tides will be aliased are shown in Fig 5.16.

Between 2°N and 12 2°N 96% of this latitude range is at a latitude where at least 80% of any diurnal or semidiurnal tidal peaks would be aliased in.

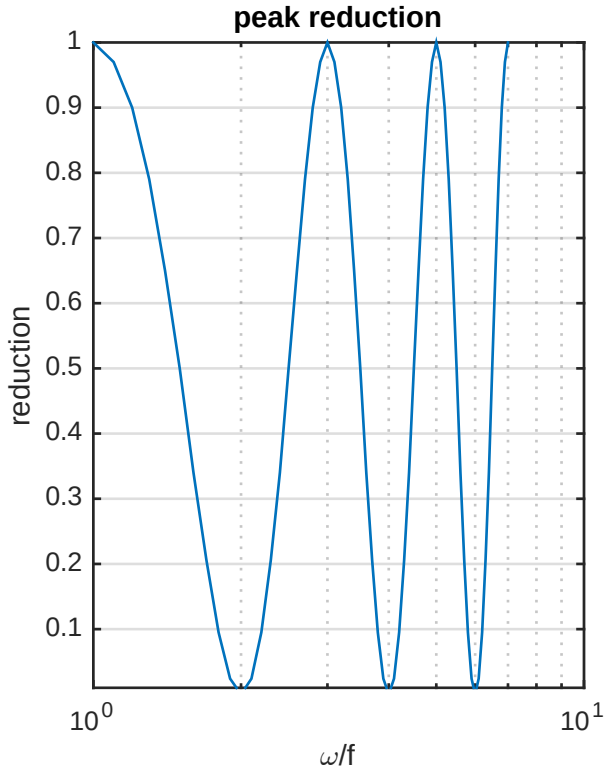

Figure 5.14: Reduction in observed spectral peak associated with a delta function in frequency. Illustrates the broad bandwidth associated with the half inertial differencing operation.

5.5 Conclusions

Synthetic time depth maps of velocity that have identically GM spectral properties are used to evaluate the frequency response of processing and gridding operations performed on data from MPs and EM–apex floats. We find that in a GM wavefield a vertical wavenumber spectrum of shear, assuming each vertical profile is instantaneous, accurately reproduces the input spectrum regardless of profiling speed. Interpolating these sloping vertical profiles back to a uniform grid, however, comes at the expense of resolved variance. At typical profiling speeds of 25-35 cm/s, the gridded MP data can be used to calculate a vertical wavenumber spectrum of shear that contains ≈90% of the input variance while at speeds slower than 15

cm/s the resolved variance drops off drastically. Reduction in shear level is relatively uniform over wavenumber.

The act of interpolating back to a uniform grid has a more profound effect on frequency content. At 25 cm/s the gridded data only captured ≈65% of the input variance and at slower speeds captured even less. Unlike the vertical wavenumber spectrum of shear where attenuation was uniform in wavenumber, the reduction in resolved variance in the frequency spectrum of velocity varies with frequency. Near the inertial frequency, decreasing profiling speed from .35 to .05 cm/s only reduces captured variance by a factor of two. At higher frequencies however, the reduction in spectral level approaches an order of magnitude.

The response of the frequency spectrum to gridding is also depth dependent. At depths

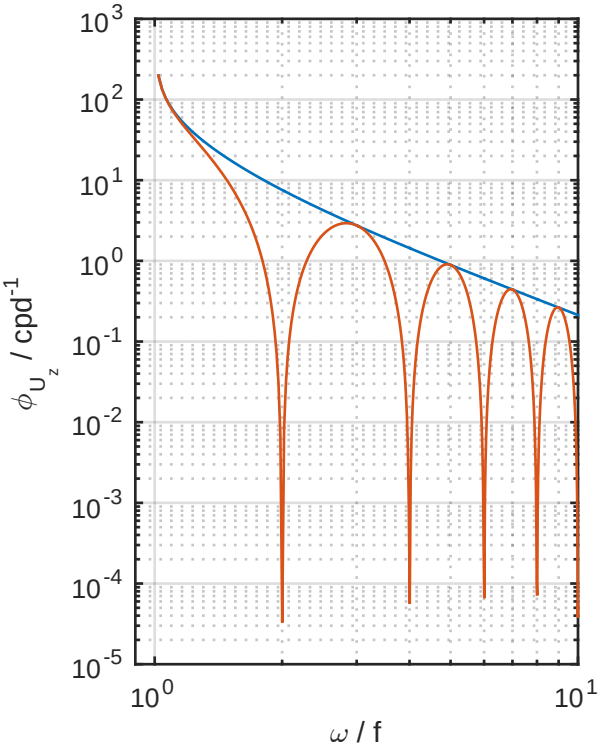

Figure 5.15: Resultant frequency spectrum of sampling a GM wavefield with a half inertial difference filter.

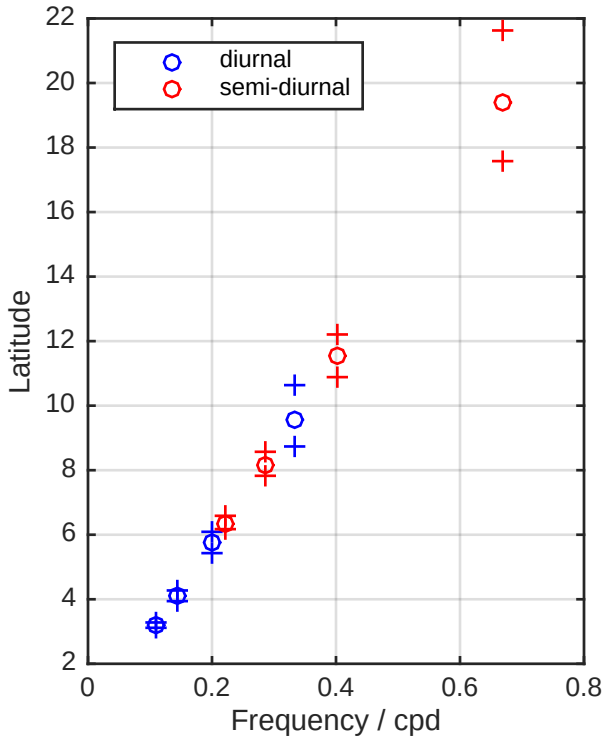

Figure 5.16: Latitudes where odd multiples of the inertial frequency fall within the range where 80% of the tidal peak will be aliased into the half inertial difference estimation of near–inertial variability.

where the mean time between samples is close to the gridding interval more of the input variance is retained. Surprisingly, the depth structure in variance relative to the input spectrum has a narrow peak, $\approx 200m$ despite the changes in temporal spacing varying linearly with depth (Fig. 5.11).

The half inertial difference filter employed by EM–apex floats reduces spectral variance by 38% which corresponds to a bandwidth of $[1, 1.28] \times N \times f$ where $N = [2n - 1] \; \forall \; [n \in \mathbb{N}]$ when integrating around all of the odd multiples of the inertial frequency when compared to a discrete GM spectrum.

The frequency response of the operation to delta functions in frequency space produces a sinusoid of the form

$$A = \frac{1}{2}\left(1 + cos(\pi * (\frac{\omega}{f} - 1))\right) \tag{5.6}$$

which can be used to estimate the output spectrum from the half inertial difference filter if the input spectrum is known. This wave form has a frequency bandwidth $\omega \pm .295\omega$ with at least an 80% transmission rate. Because of this broad bandwidth, at nearly all latitudes less than 20°N, either diurnal or semidiurnal internal tides will be strongly aliased into the inertial estimate from the half inertial difference filter. This could significantly bias any estimates of near inertial variability. Even without strong narrow band peaks, the effectiveness of the half inertial difference filter is dependent on the observations being spectrally very red.

The impact of these processing steps varies greatly depending on instrument specifications and the desired output, e.g. frequency content versus wavenumber content. It has been shown that they could introduce potentially significant biases in estimates of variance. Calculations of parameterized diffusivity depend linearly on accurate estimates of variance. This means that with all other terms held constant, underestimating shear variance by 20% would reduce the parameterized diffusivity by an equal amount.

5.6 Bibliography

Matthew H Alford. Fine structure contamination: Observations and a model of a simple two-wave case. *J. Phys. Oceanogr.*, 9:2645–2649, 2001.

Byron F. Kilbourne and James B. Girton. Quantifying high-frequency wind energy flux into near-inertial motions in the southeast pacific. *Journal of Physical Oceanography*, 45(2): 369–386, February 2015.

T.B. Sanford, J.H. Dunlap, J.a. Carlson, D.C. Webb, and J.B. Girton. Autonomous velocity and density profiler: EM-APEX. In *Proceedings of the IEEE/OES Eighth Working Conference on Current Measurement Technology, 2005.*, pages 152–

156. IEEE, 2005. ISBN 0-7803-8989-1. doi: 10.1109/CCM.2005.1506361. URL http://ieeexplore.ieee.org/lpdocs/epic03/wrapper.htm?arnumber=1506361.

Chapter 6

CONCLUSIONS

This dissertation examines various aspects of the internal wave field and its interactions with the environment. We have focused on diagnosing the role of internal waves, and their interactions, on vertical mixing in the ocean. In particular we have focused our attention on spectral properties of the wave field and its frequency content via the shear to strain ratio. From a set of observations covering a broad range of forcing and topographic regimes, this work forms a diverse examination of the shear to strain ratio and factors that influence it. The most significant results of this work are

- Parametric subharmonic instability of the diurnal tide is acting to generate near inertial waves on the South China Sea side of the Mindoro Strait in the Philippines.

- Estimates of vertical diffusivity in the Mindoro Strait are insufficient to produce the observed water mass changes through the Strait

- Our examination of the mixing in the Mindoro strait and the role of internal wave processes on generating this mixing motivated a deeper look at variations in shear and strain (and the shear to strain ratio R_ω) over a broader set of observations from over ten years of moored profiler deployments. Temporal and spatial variability in R_ω is found to be significant enough to produce order of magnitude changes in estimates of parameterized diffusivity. Variations in the shear to strain ratio could more than account for the observed factor of 2-3 disagreement between strain based estimates of diffusivity and microstructure.

- Each site can be categorized as having shear to strain ratio dominantly controlled by

either shear or strain. This means that at most sites variability is primarily in shear or strain, but not both.

- At sites with elevated shear levels, shear and strain vary at nearly the same rate, while at sites with less shear, strain varies much less. This is in contrast to the model of Garret and Munk that has a constant shear to strain ratio $R_\omega = 3$.

- The two dimensional spectrum of velocity has distinctly different wavenumber structures in the narrow band frequency peaks associated with forcing and the background continuum that cannot be reconciled with a separable model of the spectrum.

- The background continuum wavenumber spectrum of velocity does not agree with GM at low wavenumbers. Inclusion of the narrow band peaks in the total spectrum significantly improves agreement with the GM model. This implies that the commonly observed GM spectral shape is dependent on the inclusion of narrow band frequency features.

- Our analysis of the two dimensional spectral properties of shear and strain hinges on our instruments' ability to resolve internal wave variance and the impact of the gridding used in our processing routines. The impact of both the instrument sampling and gridding operation was tested using a synthetic wave field with known spectral levels. At typical profiling ranges and speeds the McLane Moored Profiler resolves nearly 90% of the variance of an idealized internal wave field. Attenuation in variance resolved can be expressed as a function of mean time between profiles and latitude.

- Half inertial difference filtering, as used by EM apex floats to isolate near inertial variability, has a broad pass band that could potentially alias in variance from the internal tides into the inertial estimate at a broad range of latitudes.

6.1 Future work

While each section draws its own conclusions, we have also tried to make clear that this work is only a small step down a long path to providing a full description of the end to end life cycle of energy input to internal waves as it flows to dissipation.

In chapter 2 we document a variety of mechanisms that were observed to be at work in the channel and contributing to the observed levels of mixing. Finding no evidence to support atmospheric forcing of intense thermocline motions, our analysis reveals that these motions are potentially generated by parametric subharmonic instability of the diurnal tide. However, we were unable to explain the existence of a phase lag between PSI generated near inertial motions and the tides. Our hypothesis that this phase lag may exist because of travel time to our location, and that PSI is happening further into the South China Sea, could be evaluated with increased spatial coverage to the north of the original mooring. Understanding the spatial structure of this observed phase lag may hold the key to understanding the presence of these waves.

Additionally, we found that the observed levels of mixing were insufficient to explain the differences in water mass properties between the South China Sea and the Sulu Sea. It is possible that because our measurements were not at the shallowest depth over the sill that the most dynamic mixing regions were un sampled by the profilers. Evaluating the levels of mixing at more points in the through flow would greatly enhance our understanding of where water mass changes are happening in this Strait and how important transformation through the Strait is on total water mass differences observed between the basins.

Chapter 3 documents observed changes in the shear to strain ratio and the impact that variability in the shear to strain ratio can have on estimates of parameterized diffusivity. While the data span a broad range of regimes, much of it is in highly forced regions with strong atmospheric activity, tidal flow, and topographic interactions. The patterns we observe could be further strengthened with continued deployment of moored profilers in a variety of locations to include both strongly forced and what we would consider open ocean

or non forced locations. Additionally, since our sites here can be categorized into being either shear controlled or strain controlled, targeting regions that may have both energetic shear and strain fields would be valuable. Improving our understanding about the shear to strain ratio of a location being shear controlled or strain controlled, and just having greater statistics on the typical range of shear to strain ratio variability, would improve our understanding about the limits of accuracy possible when parameterizing diffusivity with only partial knowledge of shear and strain.

Chapter 4 examines the vertical wavenumber frequency spectrum of velocity and strain and looks for relationships between variability in different frequency regimes. As was discussed with chapter 3, the results presented here highlight the need for improved spatial coverage of records capable of resolving in wavenumber and frequency simultaneously.

In chapter 5, our analysis of the impacts of gridding data on variance resolved could be strengthened by further modulations of the input wave field. Many of the MP sites used in this analysis display significant deviations from the GM spectral shape. Building idealized velocity fields with inherently non GM spectral descriptions that could be virtually sampled would shed a great deal of light on how non GM processes impact resolved variance.